Technische Universität München
Fakultät für Chemie
Lehrstuhl für Physikalische Chemie

Optical and Chiroptical Properties of Semiconductor and Noble Metal Nanomaterials

Matthias Jakob

Vollständiger Abdruck der von der Fakultät für Chemie der Technischen Universität München zur Erlangung des akademischen Grades eines

Doktors der Naturwissenschaften

genehmigten Dissertation.

Vorsitzender:	Priv.-Doz. Dr. Friedrich Esch
Prüfende der Dissertation:	1. Prof. Dr. Ulrich K. Heiz
	2. Prof. Dr. Dr. h.c. Bernhard Rieger

Die Dissertation wurde am 18.04.2019 bei der Technischen Universität München eingereicht und durch die Fakultät für Chemie am 20.05.2019 angenommen.

Abstract

Insight in the optical and physical properties of nanomaterials is essential for the successful development of new applications. Thus, they are studied by a great number of scientists. This work focuses on two particular groups of materials: chiral noble metal nanomaterials and semiconductor nanomaterials. Both groups are highly functional materials, which find application in light sensing and emission, catalyis and photocatalysis.
First, the mechanism of the chirality transfer from organic molecules to silver particles was investigated and found to be a mixture of a so-called chiral footprint and the polarisation of the surrounding electric field. The structure of the material does not play a role in the first place, but can still drastically influence the magnitude of the optical activity.
Secondly, the luminescence dynamics in ensembles of silicon nanocrystals were investigated. Therefore, the best fitting decay model was experimentally determined and compared to frequency-resolved spectroscopy, which allows the direct measurement of the underlying decay rate distribution. The combination of time- and frequency-resolved spectroscopy appeared to be well suited to uncover the luminescence dynamics of silicon nanocrystal ensembles, displaying a broad emission spectrum. Subsequently, the temperature-dependent photoluminescence of alkyl-capped silicon nanocrystal ensembles with mean diameters between 3 and 9 nm was studied. The well-known blueshift of the photoluminescence maximum for decreasing temperatures decreases with increasing nanocrystal diameter and eventually becomes a redshift for nanocrystal diameters larger than 6 nm, which were neglected in previous studies. It was found that a combination of bandgap widening, saturation effects and energy transfer between particles within one sample can explain the observed trend.
Finally, second harmonic generation spectroscopy was succesfully applied to semiconductor nanomaterials, which opens the opportunity to study very thin semiconductor films and also chiral semiconductor nanomaterials in the future.

Kurzfassung

Kenntnisse über die optischen und physikalischen Eigenschaften von Nanomaterialien sind essentiell für die Entwicklung neuer Anwendungen, weshalb diese von zahlreichen Wissenschaftlern erforscht werden. Der Schwerpunkt dieser Arbeit liegt auf zwei Gruppen von Materialien: chirale edelmetallbasierte sowie halbleiterbasierte Nanomaterialien. Beide Gruppen stellen hochfunktionale Materialien dar, welche in der Lichtsensorik/-emission, Photokatalyse und Katalyse Anwendung finden.

Zu Beginn wurde der Mechanismus des Chiralitätstransfers von organischen Molekülen auf Silber-Nanopartikel untersucht und es wurde gezeigt, dass dieser auf einer Kombination aus dem sogenannten chiralen Fußabdruck und der chiralen Polarisation des elektrischen Feldes beruht. Die Struktur der Materialien spielt dabei zunächst eine untergeordnete Rolle, allerdings kann der Betrag der optischen Aktivität von der Struktur stark beeinflusst werden.

Des Weiteren wurden die Lumineszenz-Dynamiken in dispersen Silizium-Nanokristallen untersucht. Dazu wurde experimentell das Modell ermittelt, welches die zeitliche Fluoreszenzabnahme am besten wiederspiegelt. Zusätzlich wurde ein Vergleich mit frequenzaufgelöster Spektroskopie durchgeführt, welche eine direkte Bestimmung der Abklingraten-Verteilung ermöglicht. Die Kombination von zeit- und frequenzaufgelöster Spektroskopie erwies sich als gut geeignet, um die Lumineszenz-Dynamiken von Silizium-Nanokristallen zu untersuchen, welche ein breites Emissionspektrum aufweisen. Daraufhin wurde die temperaturabhängige Photolumineszenz von alkylfunktionalisierten Silizium-Nanopartikeldispersionen mit mittlerem Partikeldurchmesser zwischen 3 und 9 nm untersucht. Die bekannte Blauverschiebung des Maximums der Photolumineszenz wird mit sinkender Temperatur kleiner und schlägt schließlich für Partikel mit einem Durchmesser größer als 6 nm, welche in vorherigen Studien meist nicht beachtet wurden, in eine Rotverschiebung um. Die beobachteten Trends konnten durch eine Kombination aus Bandlückenweitung, Sättigungseffekten und Energietransfer zwischen Partikeln innerhalb einer Probe erklärt werden.

Abschließend wurde Frequenzverdopplungsspektroskopie an Halbleiter-Nanomaterialien erfolgreich erprobt und dadurch die Möglichkeit eröffnet, zukünftig sowohl sehr dünne Halbleiter-Schichten, als auch chirale Halbleiter-Nanomaterialien zu untersuchen.

Table of Contents

1 Introduction

In times of an increasing demand for resources, nanotechnology may help to mitigate this trend. As the surface to volume ratio increases with decreasing particle size, smaller amounts of materials may be used, subsequently leading to more sustainable products.[1] In this regard, catalysis is an important example, where the reduction of particle size can lead to a great improvement of resource efficiency.[2,3] This has a great impact on major businesses like the automotive industry, which used approximatelly 40 % of the worldwide mined platinum between 2005 and 2010.[4] In 2018, the use of platinum in the automotive industry was already around 67 % of the total consumption, despite the use of nanoparticles as catalytical active material, and the number of manufactured cars is still increasing.[5–7]
However, nanomaterials offer even more possibilities e.g. in the fields of drug delivery, sensors or efficient light harvesting systems.[8,9] Nanoscaled materials also play an important role for the advance in semiconductor nanotechnology, which made developments such as smartphones or artifical intelligence possible in the first place.[10–14] The use of colloidal semiconductor nanoparticles is also already established, e.g. for quantum dot enhanced liquid crystal displays.[15] The advantage besides a very high stability is that only ultraviolet LEDs are necessary to excite the RGB quantum dot mixture, which can be encapsulated in small entities displaying the pixels on screen.[9,15] Other nanomaterials are, among others, currently used as pigments, for conductive inks, as lubricants or as reinforced composite materials.[16,17]
A rather new field are chiral nanomaterials, and so far two main approaches to produce them are known. This is on the one hand chirality by structure e.g. chiral helices or chiral cross like structures[18–20] and on the other hand inducing chirality into an achiral material by attaching chiral ligands to it[21–23]. Also, a combination of both can be realized by reducing the metal in presence of a chiral molecule, leading to materials with high optical activity.[24–26] Chiral nanomaterials are applicable for enantioselective chromatography, chiral sensing and asymmetric catalysis and will remain of interest and importance in the future.[27–29]

Technological progress always needs an extensive state of the art knowledge and therefore preceding sophisticated research. Thus, the scope of this thesis is to gain further insight into the optical properties of nanomaterials, whereby two groups of materials are of particular interest: chiral noble metals and semiconductors. Both are highly functional materials which can be used for catalyis, photocatalysis or light sensing and emitting applications.[2,9] Studies

on silver and gold nanomaterials with focus on chiroptical properties and studies on the emission properties of silicon nanomaterials are presented in the following.

2 Theoretical Background

2.1 Nanoparticles – Synthesis and Application

In general, the demand for nanoscaled materials is increasing and therefore a large body of literature dedicated to the development of new production and synthesis routes emerged over the last decades.[30–33]
This section gives an overview of the common synthesis approaches for noble metal and semiconductor nanomaterials and their possible applications.

Noble Metals

Several synthesis routes are known for noble metal nanomaterials. The first and simplest method was developed by J. Turkevich in 1951 and was refined by G. Frens in 1970.[34,35] The method utilizes trisodiumcitrate as reducing and electrostatic stabilizing agent, and the amount of citrate determines the resulting particle size; e.g. a higher concentration yields smaller particles. Recently, the reaction pathway in the Turkevich reaction was worked out for gold nanoparticles, revealing that gold nanowire networks are formed as an intermediate species.[36] Other prominent methods are the Brust-Schiffrin method and Martin Method, which allow the creation of hydrophobic or neat gold nanoparticles respectively.[37,38] A more recent method is the use of Good's buffers, in which the formation of gold nanoparticles was found to be induced by free radicals.[39,40]
Thus, the exploration of new synthesis routes for noble metal nanoparticles is still of interest and also the morphology can be controlled very well by now, including the synthesis of cubes or stars.[39,41] Gold and silver nanoparticles exhibit a broad range of possible applications and were already unwittingly used to produce stained glass by the romans.[42] Nowadays, noble metal nanoparticles are used for diagnostic, antibacterial, conductive, optical and catalytic applications. Silver nanoparticles are for example integrated in fabrics to avoid the growth of bacteria and are used in conductive inks.[43–45] Gold nanoparticles however can be efficiently utilized in bioanalytics or even as a catalyst.[46–49]

Semiconductors

The synthesis of semiconductor nanomaterials is more complex and requires controlled conditions in many cases.[50] Semiconductor nanoparticles can be synthesized by four different

main approaches. These can be categorized in physical, gas-phase, solution and solid-state methods. Physical methods like etching of bulk silicon, ball milling or laser ablation are so-called top-down approaches. Whereas the rest can be classified as bottom-up methods. From these, solution and solid-state methods are by now the most versatile techniques. The silicon nanocrystals (SiNCs), investigated in this work, were produced by a solid-state method. This method is introduced in the following.

The disproportionation of silicon-rich oxides was introduced by Liu et al.[51,52] and further improved by Veinot et al.[53] The improved version uses commercially available hydrogen silsesquioxane (HSQ) in its polymeric form as a precursor. HSQ is then annealed at high temperatures (>1100 °C) under argon atmosphere, containing some percent of hydrogen. This produces small SiNCs embedded in a silica matrix, which can be set free by HF etching. The method allows a precise control of the mean particle size, whereby the annealing temperature and duration of the etching process determine the final crystal size. Higher temperatures yield larger crystals and longer etching times subsequently reduce the size.[54,55]

After removing the silica matrix, the freestanding hydrogen-terminated SiNCs can be extracted from the etchant and subsequently functionalized via the hydrosilylation reaction. For this, any ligand containing a terminal alkene or alkine can be used.[56] By changing the size and functionality, the optical properties of the obtained SiNCs can be changed significantly.[57]

Semiconductor nanoparticles in general can be used for a manifold of applications such as LEDs,[58,59] solar cells,[60,61] sensors[62,63] and display technology[64]. However, the amount of heavy metals in electronic devices shall be reduced in the future.[65] This limits the use of well-established systems like CdSe nanoparticles[15,59], and therefore the demand for less toxic substitutes is rising. Silicon is a promising candidate, as it is abundant, biocompatible, and already used in computer technology and solar cells in its bulk form.[66,67] Consequently, silicon nanomaterials gained a lot of attention in the last decades. Also due to the tunability of their optical properties, which can be controlled by their size and functionalization.[55,57,68] Recently, also medical applications like magnetic resonance or fluorescence imaging were demonstrated.[69,70]

2.2 Optical Properties of Noble Metal and Silicon Nanomaterials

Silver and Gold

The optical appearance of spherical silver and gold nanomaterials is mostly originating from the localized surface plasmon resonance (LSPR). In order to generate a surface plasmon resonance (SPR) the presence of free electrons in proximity to the particles interface is

mandatory. SPR is therefore only observed in metals. The SPR can be described as a surface electromagnetic wave propagating along the material interface, generated by a cumulative electron oscillation relative to the positively charged lattice ions. This oscillation can be excited by absorption of light.[71,72]

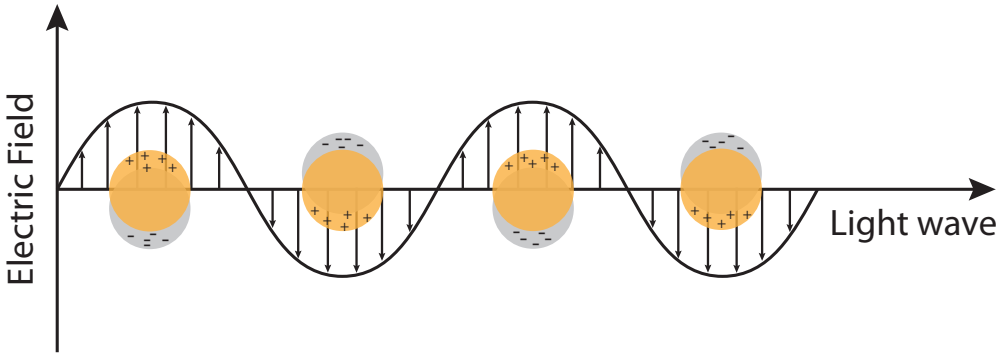

Figure 2.1: Scheme of the dipolar LSPR excited by an electromagnetic wave. The orange spheres represent the metal core, whereby the grey spheres represent the oscillating electron cloud.

In Figure 2.1, a simplified description of the ongoing processes during irradiation with light is depicted. The external electromagnetic field forces the conduction electrons to move to one side of the nanoparticle's surface, which leads to an accumulation of negative charge on the one side and positive charge on the other side. Thus, an electric dipole is created and subsequently a restoring force emerges, leading to an oscillation once the external force vanishes. This oscillation occurs at a certain frequency called the plasmonic frequency. The closer the frequency of the external electromagnetic field to the plasmonic frequency of the SPR, the better the excitability, leading to a larger oscillation amplitude. The electron oscillation is a form of kinetic energy, which is withdrawn from the illuminating light. Therefore, the SPR can be investigated by absorption spectroscopy and the larger the amplitude of the excited oscillation, the more light gets extincted.[72–74]
In a bulk metal, the surface plasmon polariton, which is the electromagnetic wave along the metal/dielectric interface, can be described as:[73,74]

$$\omega_{SP} = \frac{\omega_p}{\sqrt{1+\epsilon_d}} \tag{2.1}$$

with ω_p and ϵ_d being the plasma frequency and dielectric constant of the dielectric layer respectively. The plasma frequency in turn depends on the number density of electrons n_e:[74]

$$\omega_p = \sqrt{\frac{n_e \cdot e^2}{m_e \cdot \epsilon_0}} \tag{2.2}$$

with e being the elementary charge, m_e being the effective electron mass and ϵ_0 being the vacuum permittivity. This means the higher the electron density in the metal, the higher is

also the frequency of the surface plasmon polariton and thus the smaller the wavelength. If for example an electron acceptor is attached to the metal surface, the electron density within the metal decreases and a redshift of the plasmon wavelength occurs. This behavior can be applied in SPR sensors, which are used for plasmon enhanced immunoassays or in resonant waveguide grating biosensors.[71,75]

However, these equations do not describe the SPR in nanoparticles properly, as it is constraint to the nanoparticle dimensions. In the early 20th century, Gustav Mie[76] explained the color of noble metal colloids for the first time by solving the Maxwell equations under the assumption of no particle interactions, which does not hold true for real systems. A simpler approach is the dipole approximation, which can be applied for particles much smaller then the wavelength of the incident light (radius $<$ 50 nm). Within this approximation, the wavelength-dependent absorption cross section for small spherical particles is given by

$$\sigma_\lambda = \frac{18 \cdot \pi \cdot V \cdot {\epsilon_m}^{3/2}}{\lambda} \cdot \frac{\epsilon_2}{(\epsilon_1 + 2 \cdot \epsilon_m)^2 + {\epsilon_2}^2} \tag{2.3}$$

with V, λ, ϵ_m, $\epsilon_1 + i\epsilon_2$ being the particle volume, the light wavelength, the dielectric constant of the surrounding medium and the complex dielectric function of the metal respectively. The resonance condition of the LSPR is met when $\epsilon_1 + 2 \cdot \epsilon_m = 0$, which is in the case of silver or gold in the visible wavelength range.[74,77]

Consequently, the resonance condition is not affected by the particle volume and the position of the LSPR should be size independent. However, strong size dependence is observed for colloidal noble metal nanoparticles.[78] The size dependence of the spectral shape and also of the resonance wavelength arises from damping effects, as the moving electrons are scattered at the ionic metal cores and also at the particle surface. The damping constant is given by

$$\gamma = \gamma_0 + A \cdot \frac{\nu_F}{R} \tag{2.4}$$

$$\gamma_0 = \nu_F / l_\infty \tag{2.5}$$

with γ_0 representing the damping caused by the material specific scattering of the oscillating electrons with the ionic cores. ν_F is the velocity of the conducting electrons and l_∞ the electron mean free path within the metal. The second term in equation 2.4 describes the size-dependent scattering behavior of the oscillating electrons at the particle surface with R being the particle radius and and A being a material-dependent constant. When the particle size increases, the amount of electrons close to the surface decreases and the total damping is reduced. Therefore, the damping at the surface is inversely proportional to the particle radius.[72] It is known that the intensity of a linear oscillator increases and the FWHM decreases with decreasing damping and thus increasing particle size. However, the damping constant influences the resonant frequency only slightly and it was found that the

size dependency of the resonant wavelength of small nanoparticles is caused by interband transitions contributing to the dielectric function.[79,80]
The particle morphology also plays a major role for the shape of the observed LSPR, as the restoring force of the plasmonic oscillation depends on the accumulated charge at the particle surface. For prolate structures or nanorods this becomes especially obvious, as charge can accumulate along the long or the short axis of the particle. The plasmons are correspondingly called transversal and longitudinal. The transversal plasmon is located at higher frequencies than the longitudinal one, as more charges accumulate along the long axis. This leads to a plasmon splitting, caused by a redshift of the longitudinal plasmon and a blueshift of the transversal plasmon compared to the plasmon of a spherical particle.[72,77,81]

Silicon

To understand semiconductors' optical properties one has to consider the development of the energy states in nanoparticles and bulk materials. When two atoms of the same kind approach each other, their wave functions start to overlap. Thus, for N atoms forming a single particle, all electrons from one orbital occupy 2N different states due to Pauli's exclusion principle, and a band of states is formed. The lower band is called valence band and the upper band is called conduction band. The valence band is completely filled with electrons and is therefore not able to carry a current. The conduction band is empty, but may carry a current, if an electron is placed in it. In metals both bands are overlapping and are thus conductive. Contrary to metals, the valence and conduction band do not overlap in semiconductors and insulators, but are separated by the so-called bandgap.[82] The bandgap is dependent on the temperature, while it reaches a maximum value at 0 K.[83] It was proposed that the main reason for the temperature dependence is a shift of the position of the valence and conduction band, caused by a dilatation of the lattice or a change in the electron lattice interaction.[83] The model for the temperature-dependent bandgap was introduced by Varshni et al.[83] and improved later on.[84]
The bandgap in inorganic semiconductors can exhibit values between 0.2 and 4 eV, while materials with a higher bandgap are usually classified as insulators.[82,85]
In general, two types of semiconductors exist and these are direct and indirect bandgap semiconductors (see Figure 2.2 a). The main difference is that the highest point in the valence band and the lowest point in the conduction band are not at the same value of $\overrightarrow{k}$ for indirect semiconductors. Thus, the additional interaction with a phonon is necessary to mediate an optical transition (see Figure 2.2 b), which lowers the overall transition probability.[86]
An electron excited to a level in the conduction band will leave back a hole in the valence band and will subsequently relax thermally to the bottom region of the conduction band. The so created electron-hole pair can then recombine under emission of electromagnetic radiation. However, also the the emission of a phonon, which is a non-radiative decay channel, may

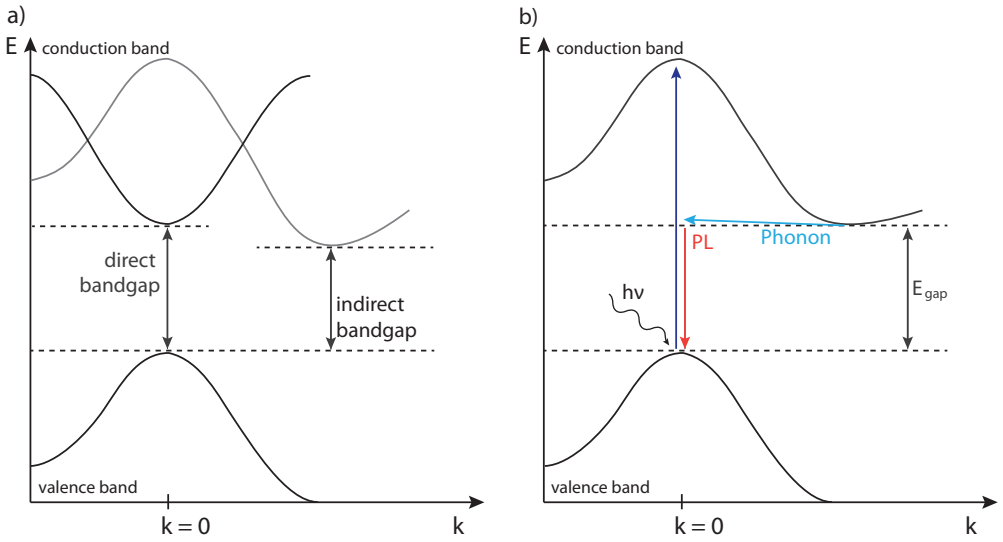

Figure 2.2: a) Simplified band structure of a direct and an indirect semiconductor. b) Schematic of a phonon mediated photoluminescence (PL) in an indirect semiconductor.

happen.[86] Whether a radiative or a non-radiative decay occurs, depends, among others, on the surrounding temperature. While at low temperatures (< 100 K) the radiative transition prevails, it is the opposite case at higher temperatures.[87]

In porous silicon the excited charge carriers are usually localized on different sites in the material and must therefore move to the same site in order to recombine. This behavior can be described by the radiative tunneling model, which was proposed in 1979 by Tsang and Street.[87] As the electron-hole separation varies randomly, a lifetime distribution is expected for the occurring luminescence. However, the radiative tunneling model is not able to explain the occasional appearance of an additional fast luminescence band and the wavelength dependence of the luminescence lifetime. Therefore, two different processes were proposed. This is firstly the recombination of a geminate electron-hole pair produced by a single photon and secondly the recombination of distant electron-hole pairs. This distant pair moved away from each other or was produced by different photons in the first place.[87] It was found that the photoluminescence (PL) in porous silicon actually originates from small embedded SiNCs and nanowires.[68,88] Consequently, free standing SiNCs exhibit similar optical properties. The bandgap of SiNCs is still of an indirect nature, however their small size causes a confinement of the electrons and holes.[89,90] This quantum confinement leads to a high-energy shift of the bandgap and to an increased recombination rate at ambient temperatures.[91] The first effect can be explained by the particle size and its effect on the Bohr exciton radius, which is the average distance of an electron-hole pair in a bulk material. If a particle is smaller than twice the Bohr exciton radius, then the electron-hole distance gets limited and reduced by the particle size. This in turn leads to an increase of the oscillator strength and a subsequent high energy shift of the bandgap.[91,92] The increased recombination rate is proposed to originate from an uncertainty in the crystal momentum of the SiNCs,

which leads to more allowed transitions without the involvement of a phonon.[90,92] The amount of these "quasi direct" transitions was predicted and found to increase for decreasing crystal size.[90,92]

Subsequently, the PL of SiNCs can be tuned by the crystal size, but also by attaching different surface groups.[57] While simple alkyl-capped SiNCs show a broad size-dependent PL peak between 600 and 1000 nm[53,93–95], blue emission was observed for amine-terminated SiNCs[55,96]. Also, the amount of surface oxidation plays a significant role and leads to a blue-shift in the observed PL.[55,97] To sum up, the PL of silicon nanocrystals can be tuned over the whole visible wavelength range, utilizing a combination of crystal size and surface functionalization.[55] Recently, two dimensional silicon nanomaterials were created and gained attention.[98] The so-called silicon nanosheets can be created by the exfoliation of calcium silicide and show stable green PL, if incorporated in a stabilizing matrix like a polymer.[99] The field of silicon nanomaterials offers many technological opportunities and will stay an important topic for the future. Furthermore, they represent a less toxic and more biocompatible alternative than the established quantum dot systems using CdSe, InAs or PbS as main material.[100,101]

2.3 Chirality and Chiral Nanomaterials

Chiral amino acids and sugars are a central part of life on earth. Surprisingly, life is even homochiral, meaning that only L-amino acids and D-sugars are present, while the counterparts are toxic in most cases.[102,103] The origin of this homochirality is not yet resolved and is thus still studied.[104] In Figure 2.3, the structure of L- and D-cystein is depicted and they exhibit mirror image symmetry. Chiral means that a molecule shows handedness and can therefore not be superposed with its mirror image also known as enantiomer. A chiral molecule in a

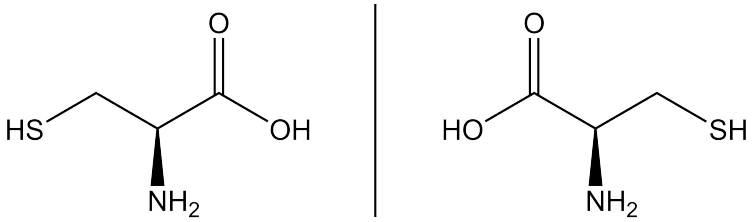

Figure 2.3: The chemical structure of L- and D-Cystein respectively. The two enantiomers are mirror images and thus cannot be superposed.

more chemical sense is usually defined as a molecule containing at least one chiral center, which in turn is defined as an atom exhibiting 4 different binding partners.[105] However, there is also another kind of chirality. An intrinsically achiral material like a metal can nevertheless exhibit optical activity, e.g. noble metal helices and cross-like structures.[26,106–108] However, also a combination of chiral molecules and an achiral material is possible and can lead to

an induced chirality in the achiral material. This was found to be the case for plasmonic noble metal particles coated with chiral molecules. These metal particles showed plasmonic chirality without exhibiting an intrinsically chiral structure in the first place.[22,24,107,109,110] Naturally, also the mixture of structural and induced chirality can be realized, leading to a large optical activity.[26] In general, three different chirality transfer mechanisms are known up to now: I) a chiral structuring during the formation of the material, due to the influence of the surrounding chiral molecules, II) electronic interaction of the achiral material with the chiral ligands and III) a chiral arrangement of the chiral ligands leading to a chiral deformation of the achiral material.[111] The third of the possible mechanism is also called chiral footprint.[111] These mechanism are not excluding each other and may also appear simultaneously depending on the investigated system.[24,111]
Chiral materials find applications in asymmetric catalysis[29,112,113], chiral sensing[114,115] and chiral photonics[116]. Therefore, the topic of chiral materials is further investigated and will remain important in the future.

2.4 Characterization Techniques

2.4.1 Optical Characterization

Ultraviolet/Visible, Circular Dichroism and Optical Rotation spectroscopy

Ultraviolet/Visible (UV/VIS) spectroscopy is based on the absorption of monochromatic electromagnetic radiation. In general, interaction between radiation and matter can be classified into absorption, transmittance and scattering. Although originating from completely different physical processes, scattering and absorption cannot be distinguished by an absorption based technique and are thus summarized as extinction.[117] However, scattering is almost negligible in diluted solutions and the extinction is then referred as absorbance[118], which is displayed in many commercial devices. The relationship between the transmittance T and the absorbance A is then defined as:

$$A = log\frac{I_0}{I} = log\frac{1}{T} \tag{2.6}$$

with I and I_0 being the light intensities before and after passing through the sample.[119] Usually I_0 is determined by the measurement of the solvent in the case of a cuvette or the bare support material in case of thin films. UV/VIS spectroscopy can also be used to quantify dissolved materials. The absorbance A follows the Beer-Lambert law for a certain concentration range and is expressed as follows:

$$A = \epsilon \cdot c \cdot l \tag{2.7}$$

with c being the molar concentration, l the path length and ε the wavelength-dependent molar extinction coefficient.[119] With that, UV/VIS spectroscopy can be used to characterize the optical properties of many materials. When measuring thin solid nanomaterial films, scattering can become a problem and an extension of the simple UV/VIS spectrometer by an integrating sphere is necessary. The inside of the sphere is coated with highly reflective materials like $BaSO_4$ and for an absorption measurement the sample specimen is put in the middle of the sphere. In an empty sphere, the incident light hits the sphere's wall and the light is scattered diffusively in all directions. The light is scattered until it reaches the detector and gets absorbed. With the specimen mounted in the middle of the sphere, additional absorption takes place and decreases the detected light. The absolute absorption of the sample can be measured, as light scattered by the sample is still detected. An integrating sphere can also be used in reflectance mode. Therefore, the sample is put on the wall, opposite to the entrance slit of the incident beam, and the reflected light is detected. The sample's reflectance can then be normalized to a reflectance standard.[120–122] An integrating sphere can also be used to determine the absolute quantum yield of a sample or the luminous-flux of a light source.[123,124]

If information about optically active materials shall be obtained, conventional UV/VIS spectroscopy does not suffice any more and has to be extended with a polarizer and a subsequent quarter wave plate or photoelastic modulator. This generates circular polarized light. The measurement principle is similar to conventional UV/VIS in transmission mode, but the absorbance for left and right handed cirular polarized light $I_{L/R}$ is determined separately and the difference of the molar extinction coefficient, which is defined as circular dichroism (CD), can be determined:[125]

$$\Delta A = A_L - A_R = log\frac{I_0}{I_L} - log\frac{I_0}{I_R} = log\frac{I_R}{I_L} \tag{2.8}$$

$$\Delta\epsilon = \frac{1}{c{\cdot}l} \cdot \Delta A \tag{2.9}$$

It is obvious that I_0 does not play a role for the measurement of ΔA and the devices are thus of a single-beam type, as no reference beam is necessary. To ensure a stable measurement, the voltage applied to the photomultiplier is varied and the measured photo current is kept constant. The applied voltage is then used to calculate the respective absorbance of the sample.[125] Most commercial CD spectrometers measure the absorbance and CD value simultaneously and the concentration-independent anisotropy factor/g-value can be calculated:[125]

$$g = \frac{\Delta A}{A} \tag{2.10}$$

Circular dichroism is often displayed as ellipticity Ψ, which is connected to the g-value via the following relationship:[125]

$$\Delta A = \frac{\Psi[deg]}{32.98} = \frac{\Psi[mdeg]}{32980} \tag{2.11}$$

In principle the ellipticity can be directly measured by sending linearly polarized light through a chiral material. Linear polarized light can also be described as a perfect mixture of left and right handed circular polarized light. This results in elliptical polarized light, as one of the two circular polarizations is absorbed more by the chiral material.[125] However, the measurement of ΔA has proven to be more convenient and is usually automatically converted into ellipticity by the spectrometer (equation 2.11).[126] Another way to characterize chiral substances and materials is to determine their optical rotation or optical activity. When linear polarized light at a non-resonant wavelength passes through a chiral medium, the plane of polarization is rotated about the optical axis. This value can be very specific for neat molecules and is used to identify chiral substances, determine their concentration or to measure the enantiomeric ratio. The specific optical rotation at a certain wavelength λ is defined as:

$$[\alpha_\lambda] = \frac{\alpha}{l \cdot \rho} \tag{2.12}$$

with α, l and ρ being the measured rotation, the length of the tube and the density in g per 100 mL respectively. The correct unit of the specific rotation is thus deg cm^2 g^{-1}, but often just the value itself is given.[125]

Photoluminescence Spectroscopy

Luminescence is the subsequent spontaneous emission of light from a substance, which is in an excited state. In the case of PL, the excitation happens through absorbed high energy radiation like UV light. PL is known to occur in organic molecules, but also in semiconductors. However, different mechanisms take place. The luminescence of molecules can be described by the Jablonski diagram and can in principle be classified into two categories. These are fluorescence and phosphoresence, which take place at different time scales. Whereas fluorescence occurs in the nanosecond regime, phosphorescence, which is a quantummechanical forbidden transition from an excited triplet state to a singlet ground state, takes place in time scales between microseconds and seconds. Sometimes even lifetimes of minutes or hours can be observed.[119,127,128]

In the case of semiconductors, electron-hole pairs are generated upon UV excitation, which can then recombine under emission of radiation. The lifetime in semiconductors is mainly dependent on the nature of the material and also on its purity, as impurities may create excitons or act as recombination centers. Excitons in indirect semiconductors may recombine

without the involvement of a phonon and thus shorten the observed luminescence lifetime.[86]

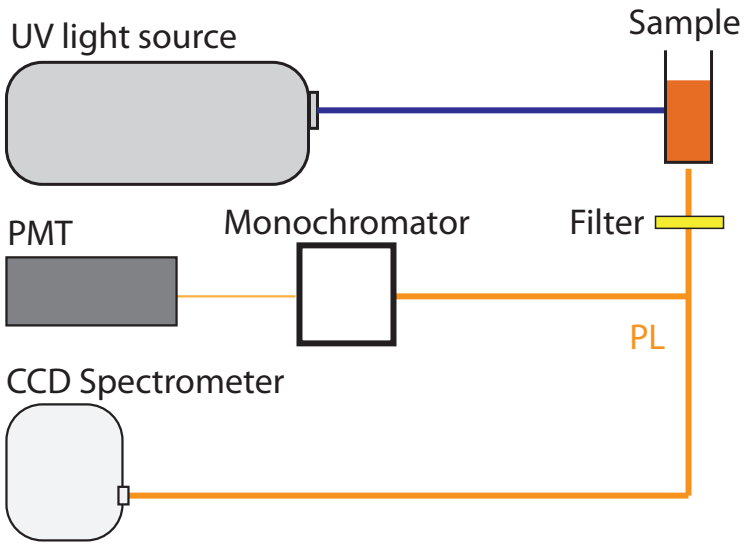

Figure 2.4: Scheme of a PL setup, which is capable of measuring luminescence spectra, as well as luminescence lifetimes. A pulsed UV excitation source hits a luminescent sample and the occurring PL is collected, filtered and guided to a spectrometer or a monochromator with subsequent PMT respectively.

Independent of the luminescent material, PL spectroscopy is performed in the same way. The sample is excited using a high energy light source. Very often Ar^+ lasers with a wavelength of 351.1 nm or xenon arc lamps combined with a monochromator are used for this purpose. The occurring PL is measured perpendicular to the excitation beam and longpass filters are used to minimize detected excitation light. The PL is then guided to the detector by means of optics or optical fibers, where the wavelength-dependent light intensity is measured. This may happen through a combination of a monochromator and a photomultiplier tube (PMT), or a grating combined with a CCD chip.[127] The measurement of time-resolved PL needs some extensions, which are in particular a pulsed excitation source and a very fast detector. Many lasers and also the xenon arc lamp are naturally operated in pulsed mode, however also continuous light sources may be converted into a pulsed source by using an acousto-optic modulator. The fast detector can be a PMT or a photodiode. The PMT exhibits a higher sensitivity and signal to noise ratio, whereas photodiodes are available for a greater wavelength range.[127] As both do not distinguish between the incident wavelengths, a monochromator has to be used prior to the detection, if time-resolved and simultaneously wavelength-dependent spectroscopy shall be performed.[127]

A further extension to the already named spectroscopies is the temperature-dependent PL spectroscopy. For that, some sort of cryostat with an integrated temperature controller needs to be installed. The investigated samples are usually cast on a support and mounted onto the cryostat, which in turn is placed in a vacuum chamber. Vacuum is necessary at low temperatures to avoid unwanted contamination by freezing water or gases from the

surrounding air.[129,130] The temperature can have a great effect on the observed PL and is often used to investigate fundamental mechanisms.[97,129,131,132]

Second Harmonic Generation Spectroscopy

Nonlinear optical processes occur when intense radiation hits a medium, which responds non-linearly to the incident light's electric field. Usually, only laser light is intense enough to mediate these effects. In 1961 Franken et al.[133] discovered the phenomenon of second harmonic generation (SHG), which was the start of this scientific field.[134] SHG can be described as absorption of two photons of the same energy and the emission of a photon with twice the energy. It's efficiency scales quadratically with the strength of the incident electromagnetic field and thus the incident light intensity. The amount of generated second harmonic light also depends on the second order susceptibility χ^2. In materials with inversion symmetry, χ^2 is zero and therefore no second harmonic light can be generated.[134] As a consequence, SHG is only possible in materials without inversion symmetry; e.g. a materials surface or particles deposited on a support.[81,135–137] In Figure 2.5, the SHG and SHG-CD process is described schematically. Generated second harmonic light travels coherently with the fundamental light and must thus be separated by a filter or prisms prior to detection.[138] SHG itself can be off-resonant or resonant depending one the incident wavelength and the material's optical properties. If neither the fundamental wavelength, nor the second harmonic wavelength hits an energy level, it is called off-resonant and thus only small second harmonic intensities are observed. In case of a resonance with the fundamental or second harmonic wavelength, a strong enhancement of the second harmonic signal is observed. This can be utilized and a wavelength-dependent measurement can be performed, leading to a nonlinear optical spectrum of the material.[136,138] SHG spectroscopy is a sophisticated technique, which needs to be

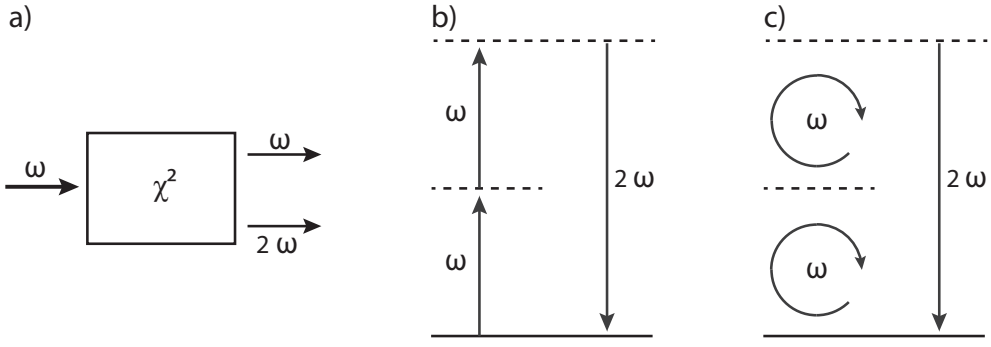

Figure 2.5: Scheme of the SHG process. a) Intense light passes through a nonlinear medium and coherent second harmonic radiation is produced. b) Schematic energy diagram for the SHG process. c) SHG is also possible with circular polarized light.[134]

correctly referenced and power corrected in order to yield meaningful results.[138,139] However, its sensitivity is outstanding and thus enables studies of systems with monolayer and even sub-monolayer coverage.[135,138,140] It is furthermore not restricted to linearly polarized light

and the study of chiral materials by the means of SHG was introduced by Byers and Hicks in 1993.[141,142] Also, the theoretical formalism and the experimental technique of SHG-CD was studied intensively[143] and the nonlinear g-value was defined as[141]

$$g_{nl} = \frac{(I_{left} - I_{right})}{\frac{1}{2}(I_{left} + I_{right})} \tag{2.13}$$

with g_{nl} being the nonlinear anisotropy factor and $I_{left/right}$ being the measured second harmonic intensity for the corresponding circular polarization. The SHG/SHG-CD technique was carried on by different groups since then and lead to new insights in the field of clusters and chiral nanomaterials.[81,136–138,143–145]

2.4.2 Materials Characterization

In many cases a profound knowledge about the investigated materials is necessary to draw any conclusion. In the following section, a brief introduction about the used materials characterization techniques is given.

Infrared Spectroscopy

Infrared (IR) spectroscopy is similarly to UV/VIS a transmission based technique and the same conditions and equations hold true (see section 2.4.1). However, the used monochromatic light usually resembles around 2000 - 20000 nm (500 - 5000 cm^{-1}), as molecular vibrations can be excited in this wavelength range. Thus, the main difference to UV/VIS is the excited transitions and with that very different information can be obtained.[119] While UV/VIS is mainly used to get information about the optical properties or to quantify a substance, IR spectroscopy is used to gain information about the presence or absence of certain molecules or about the nature of the interaction between materials. This is possible due to very characteristic vibrations of the different functional groups. While for example C=O, C=N or C=C appear between 1500 and 1800 cm^{-1}, O-H or N-H exhibit absorption bands between 3200 and 4000 cm^{-1}.[119] It is thus possible to investigate, if a molecule is physisorbed or chemisorbed or if a chemical reaction took place. This is for example the case for N-H containing molecules, because the typical N-H stretching vibrations will disappear upon chemisorption or chemical linkage. In this sense IR spectroscopy is often used to check the state and success of a chemical reaction.[119]

X-ray Photoelectron Spectroscopy

X-ray photoelectron spectroscopy (XPS) is a surface analysis technique, which was developed to measure the elemental composition and the chemical state of the elements in a material. In this technique, high energy X-ray radiation is used to penetrate a materials surface and to

remove electrons from the core level orbitals. These so-called photoelectrons may leave the material and are then captured. Their kinetic energy is analyzed by a hemispherical analyzer. Through the measured kinetic energy and the known applied radiative energy, the bonding energy can be calculated and hence the material from which it escaped can be identified. XPS is a surface sensitive technique, as the mean free path of electrons in a material is only between 1-10 nm. Thus, electrons released deeper are scattered and do not reach the sample surface.[119,146]

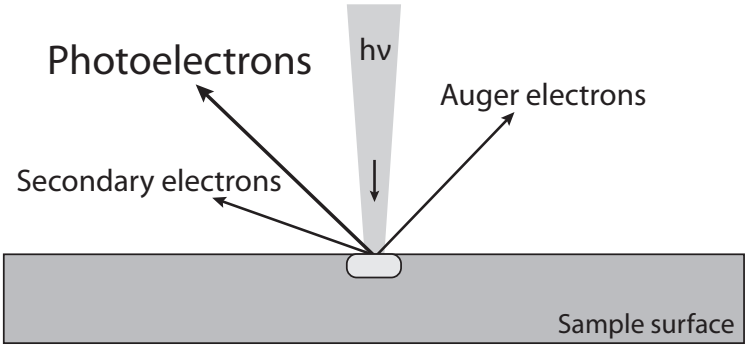

Figure 2.6: Schematic view of the different processes after X-ray irradiation of a material. For XPS the photoelectrons are analyzed. In many cases also the combination with the analysis of Auger electrons is beneficial.[119]

Before the photoelectrons can be analyzed, photoionization must occur. The probability for this process to happen depends on the photoionization cross section, which in turn depends on the target element and the energy of the incident photon. Above the photoionization threshold, the cross section decreases with increasing photon energy, whereas below it is zero. The process can be formally described as

$$A + h \cdot \nu \rightarrow A^+ + e^- \tag{2.14}$$

with A being a neutral atom and $h \cdot \nu$ being the photon energy. On the right side, a positively charged atom and an electron is obtained. Due to energy conservation law, the energy before and after removing the electron must be equal and the following equations can be derived:[119]

$$E(A) + h \cdot \nu = E_k + E(A^+) \tag{2.15}$$

$$E_k = h \cdot \nu - [E(A^+) - E(A)] \tag{2.16}$$

$$E_k = h \cdot \nu - E_B. \tag{2.17}$$

E_k displays the kinetic energy of the released electron after leaving the material, which can then be measured. E_B is the binding energy of the electron in the atom, which is

necessary to remove the electron. It is specific to the material and the initial atomic energy level of the electron. The kinetic energy is not an intrinsic property of the material, as it depends on the used X-ray photon energy $h\nu$. The obtained spectrum has then be corrected for the background, which is mainly due to the cascade of secondary electrons. Once the background is corrected, the obtained peaks have to be fitted in order to determine the exact peak position. A mixture of a gaussian and lorenzian function is usually used to fit the peaks in XPS. Finally, any peak shifts due to charging of the sample have to be corrected. The spectrum can be referenced to a known peak like adventitious carbon. Sometimes also additional elements such as gold are added as a reference material. The obtained peak position is finally giving information about the chemical environment of a material. This is possible, because the binding energy in the atom will change if an oxide or other chemical bonds are present. XPS can in principle also be used to perform a quantitative analysis of a material, whereby the peak integrals display the quantity of the species. However, one has to take into account that XPS is very surface sensitive and does not give any information about the bulk of the material. The most typical X-ray sources are Mg $K\alpha$ and Al $K\alpha$, whereby the linewidth of Al $K\alpha$ is usually improved by a monochromator.[119,146]

X-ray Powder Diffraction

Another technique, which utilizes X-rays, is X-ray powder diffraction (p-XRD). The most widely applied radiation is Cu $K\alpha$ with a wavelength of 1.54 Å. The wavelength is comparable to the atomic distance in a crystal and therefore best suited to reveal the structural arrangement. In a crystal, the atoms are arranged periodically and the underlying fundamental structure, which is then further repeated, is called unit cell. If X-rays hit such a periodic structure, they will get scattered according to Bragg's law:

$$2 \cdot d \cdot sin\theta = n \cdot \lambda. \tag{2.18}$$

While d and θ display the interplanar distance and the diffraction angle. λ is the wavelength of the incident radiation and n is the reflection order. When investigating a sample in powdered form, the small grains are randomly orientated and the diffraction intensity is the sum of X-rays reflected from all the grains. The sample generates a diffraction pattern, which allows conclusions about crystal structure, crystal size, internal stress and composition.[119,147,148] However, also the width of the observed diffraction peaks contains information. The larger and more uniform a crystal is, the sharper the obtained diffraction peaks. This relation was described mathematically by Debye and Scherrer in 1918 leading to the Debye-Scherrer equation:[149]

$$L = \frac{K \cdot \lambda}{\Delta(2\theta) \cdot cos\left(\frac{2\theta}{2}\right)} \tag{2.19}$$

Within this equation L displays the expansion of the crystal perpendicular to the reflecting atomic plane. K is a dimensionless shape factor which is usually close to 1. λ and θ are the incident wavelength and the diffraction angle respectively. This equation is only applicable to nanoscale crystals and is not applicable to crystals larger than 0.1 μm. It gives a rough estimation on the particle size, although it is inaccurate for very small particles and is also limited to entirely crystalline particles. Any non-crystalline parts or shells will not contribute to the obtained diffraction peaks.[148,149]

Electron Microscopy and Energy-Dispersive X-ray Spectroscopy

Absolute information about size and morphology of a material can be obtained by means of electron microscopy, which is an imaging technique and in principle capable of measuring with atomic resolution. The working principle of a transmission electron microscope (TEM) is very similar to that of a light microscope. However, an electron beam and ion lenses are used instead of visible light and optical lenses. Depending on the acceleration voltage, the theoretical spatial resolution is not limited, as the wavelength λ of the electrons is proportional to the inverse of the accelerating voltage V:

$$\lambda\ [nm] \sim \frac{1.23}{\sqrt{V}} \tag{2.20}$$

However, an increased acceleration voltage will more likely lead to beam damage, which means that adventitious carbon and also the sample itself may be destroyed upon irradiation. Assuming an acceleration voltage of 300 kV in a high-resolution TEM, a theoretical spatial resolution of about 0.02 Å is reached.[119,150] As the wavelength of the electron beam is then in the region of atomic bonds, the crystal lattice can be imaged and characterized. The whole setup must be installed within a sufficient vacuum ($< 10^{-5}$ Pa), because electrons are not able to travel through air. The sample specimen is usually a copper grid, coated with an ultrathin carbon film or some layers of graphene, which ensure a maximum of transmission and thus a good contrast.[151] A TEM measurement can be performed in bright-field or dark-field measurement mode. While bright-field images are the standard and are generated by transmitted electrons, dark-field images originate from diffracted electrons. These two modes can be achieved by placing the objective aperture at the focal position (bright field) or moving it away from the focal position (dark field). In the dark field mode only scattered electrons are visible and thus only crystals that fulfill the specific diffraction condition appear bright. Consequently, bright field imaging is used to analyze the structure of the material, while thicker and more absorbing parts of the sample appear darker. Dark field imaging provides information about crystal distribution and orientation.[119,151]

Electron microscopy can also be performed in scanning mode and is then called scanning electron microscopy (SEM). Therefore, the electron beam is focused and moved over the sur-

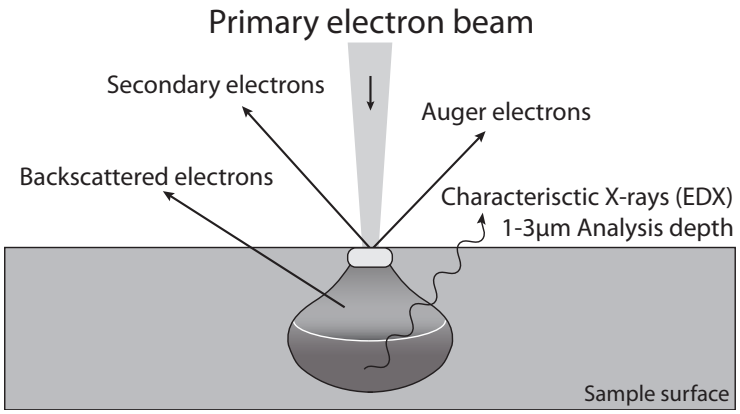

Figure 2.7: Schematic view of the different processes after irradiation of a material with a focused electron beam. In most cases, secondary electrons or backscattered electrons are used for the imaging, which yield different contrast. Characteristic X-rays can be used to gain information about the elemental composition and EDX is therefore often implemented.[119]

face by means of scanning coils. The different occurring processes are then used for imaging purposes. These effects are schematically displayed in Figure 2.7 and are namely secondary electrons, backscattered electrons, Auger electrons and characteristic X-rays. In principle, the interaction of the energy beam and the sample can be divided in elastic (backscattered electrons) and inelastic processes (secondary electrons, Auger electrons, characteristic X-ray). Most of the secondary electrons originate from the sample surface, while backscattered electrons and especially characteristic X-ray radiation originate from deeper regions of the sample. The backscattered electrons can be used to vary the imaging contrast, as their intensity is angle dependent. Moreover, chemical contrast can be achieved as larger atoms lead to more scattering and appear thus brighter. However, the resolution achieved with backscattered electrons is limited. The secondary electrons are thus the primary source for high resolution topographical images. The release of secondary electrons is dependent on the surface orientation, but they do not yield chemical contrast.

If an electron is removed from a inner shell, an electron from an outer shell can fill this vacancy and the energy difference is emitted as radiation. This characteristic radiation can be detected to identify the chemical composition of the material via energy-dispersive X-ray (EDX) spectroscopy.[119,150]

3 Experimental Methods

The following chapter gives an overview about the synthetic methods and procedures, which were applied to create the investigated nanomaterials. The applied materials and optical characterization methods are also briefly discussed.

3.1 Synthesis Procedures

3.1.1 Synthesis of Chiral Noble Metal Nanoparticles

Silver Nanoparticles

The methods, which were used to obtain chiral silver nanoparticles can be categorized into two different approaches. The first method is a direct reduction of silver nitrate, with the reducing agent being the capping ligand at the same time. The corresponding ligand is added to a stirred solution of silver nitrate in ultrapure water (UPW). For L/D-cysteine no further treatment is necessary, whereas the reaction mixture with L-glutathione needs to be refluxed for several hours.

The second approach is the creation of spherical nanoparticles, using a modified method after Turkevich[34,152], with a subsequent ligand exchange reaction. Therefore, silver nitrate is reduced by a mixture of sodium citrate and tannic acid. For the ligand exchange reaction L-glutathion was added and the mixture is stirred over night. The red precipitate was then cleaned by three subsequent centrifugation and redispersion steps. Detailed experimental information for both methods can be found in section 6.1.[24]

Gold Nanoparticles

A direct reduction of gold(III) chloride trihydrat (auric acid) was tried in the manner of silver nitrate, but in most cases only cloudy white suspensions were obtained. This indicates the formation of a polymer like gold-sulfur structure, as was also found by Gautier et al.[25]

Table 3.1: Reaction series with L-cysteine as capping and reducing agent.

Sample	auric acid [µmol]	L-cysteine [µmol]	reagents ratio
A 1	10	1	1:0.2
A 2	10	5	1:0.5
A 3	10	10	1:1
A 4	10	20	1:2
A 5	10	40	1:4

Therefore, several experimental series including an additional reducing agent were performed. To the cloudy white suspension different amounts of citrate or sodium borohydride were added to mediate the formation of gold nanoparticles with the chiral capping agent being present simultaneously. The used ratios of gold salt, cysteine and reducing agents are given in Table 3.2 and Table 3.3.

Table 3.2: Reaction series with L-cysteine as capping and trisodium citrate as reducing agent.

Sample	auric acid [µmol]	L-cysteine [µmol]	trisodium citrate [µmol]	reagents ratio
C 1	10	1	10	1:0.2:1
C 2	10	5	10	1:0.5:1
C 3	10	10	10	1:1:1
C 4	10	20	10	1:2:1
C 5	10	40	10	1:4:1

Table 3.3: Reaction series with L-cysteine as capping and sodium borohydride as reducing agent.

Sample	auric acid [µmol]	L-cysteine [µmol]	sodiumborohydride [µmol]	reagents ratio
B 1	10	10	10	1:1:1
B 2	10	10	20	1:1:2
B 3	10	10	40	1:1:4
B 4	10	10	80	1:1:8
B 5	10	20	10	1:2:1
B 6	10	20	20	1:2:2
B 7	10	20	40	1:2:4
B 8	10	20	80	1:2:8
B 9	10	40	10	1:4:1
B 10	10	40	20	1:4:2
B 11	10	40	40	1:4:4
B 12	10	40	80	1:4:8

An exemplary experimental description is given for sample B 12: To a solution of 3.98 mg gold(III) chloride trihydrate (10 µmol) in 3 mL UPW, 1.19 mg cysteine dissolved in 2 mL

UPW are added and the mixture is stirred for 2 h at 500 rpm. Then 3.02 mg of sodium borohydride are added and the mixture is stirred for further 24 h. The resulting purple solution is stored at 8 °C. The reactions using sodium citrate as reducing agent are performed in the same manner. In the case of cysteine without any further reducing agents, the solutions were stirred for 24 h at 500 rpm after addition of the ligand.
For the synthesis of small spherical gold nanoparticles the same method was used as for the small spherical silver nanoparticles. In detail 1.99 mg of gold(III) chloride trihydrate is dissolved in 48 mL of UPW. The solution is stirred at 500 rpm and heated until it starts to reflux. Then 10 mg trisodium citrate and 2.5 mg tannic acid are dissolved in 1 mL UPW each, mixed and added to the boiling gold solution. The mixture is heated for further 10 min and rapidly cooled to 0 °C afterwards. The resulting red solution is stored at 8 °C.
A ligand exchange reaction is performed with L-glutathione, as this was already successfully performed with silver nanoparticles. Therefore, 5 mL of the above prepared nanoparticle solution is put into a round bottom flask and 5 mg of L-glutathione is added. The mixture is stirred at 500 rpm, whereas a color change to violet can be observed after 2 h reaction time.

3.1.2 Synthesis of Organically Capped Silicon Nanocrystals

The investigated SiNCs have been synthesized according to the method reported by Dasog et al.[57] and the experimental details can be found in section 6.3.[130] Briefly, HSQ is heated in a zirconia furnace tube within a reducing atmosphere to a temperature between 1100 and 1700 °C. Thereby, higher temperatures yield larger crystal sizes. The resulting black material is ground in an agate mortar and milled in a wrist action shaker. After filtration, the powder is dried and stored. The fine powder can then be used to produce free-standing hydrogen-terminated SiNCs by HF etching for about 40 min. The hydrogen-terminated SiNCs are extracted with toluene from the etchant and are subsequently functionalized with 1-dodecene using AIBN as radical initiator. After 20 h reaction time, the functionalized nanocrystals are cleaned up by three cycles of precipitation, centrifugation and redispersion in clean solvent. This reaction route was chosen, because the reaction with AIBN requires mild reaction conditions only. A temperature of around 70°C is sufficient, which simplifies the use of most solvents. Furthermore, the protecting ligand can be changed very easily, as many terminal alkenes can be used instead of 1-dodecene. In this case the chiral ligand (R/S)-(1-(allyloxy)ethyl)benzene was synthesized (Scheme 3.1) and attached to the SiNCs following the above described procedure.
The synthesis conditions for (R/S)-(1-(allyloxy)ethyl)benzene were adapted from Groneberg et al.[153] To obtain the chiral molecule, 5 g (30 mmol) of enantiomeric pure 1-phenylethanol is dissolved in 40 mL of THF, cooled to 0 °C and stirred at 500 rpm. Subsequently, 2 g of NaH (60 % oil dispersion, 50 mmol) is added in portions over 10 min. The mixture is allowed to warm up to room temperature, stirred for 45 min and cooled to 0 °C again. Then

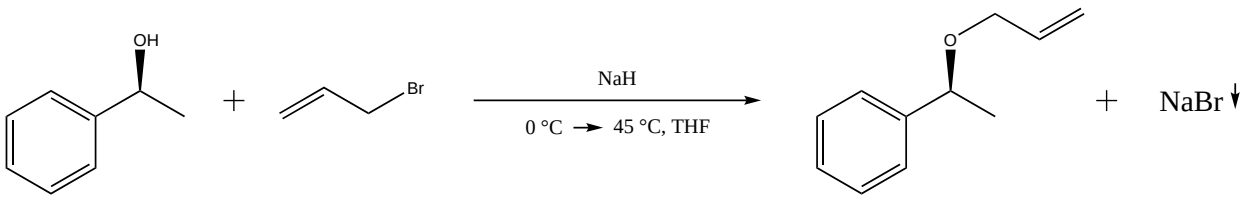

Scheme 3.1: Reaction of (R/S)-1-phenylethanol with allylbromide via S_N2 reaction mechanism, leading to (R/S)-(1-(allyloxy)ethyl)benzene.

2.6 mL of allylbromide (30 mmol) is added and the mixture is allowed to warm to room temperature and is stirred for further 45 min. To complete the reaction it is heated to 45 °C overnight. All reaction steps were performed in dry glassware and under argon atmosphere. The color of the suspension turns from grayish to white during the reaction, which indicates the formation of NaBr.
The reaction is quenched by addition of MeOH, diluted with Et_2O and washed with water two times. Finally, the organic phase is washed with brine, dried over $MgSO_4$ and the solvent is removed using a rotary evaporator. The resultant yellow oil is purified by column chromatograpy with Et_2O:pentane 1:9, yielding a pale yellow oil.
To produce SiNCs capped with the chiral ligand 200 mg of the fine powdered composite material is etched in 6 mL of 1:1:1 H_2O:EtOH:HF for 40 min. The hydrogen-terminated nanoparticles are extracted from the etchant with toluene, yielding a yellow suspension. The particles are centrifuged down at 6000 rpm for 10 min and the supernatant is discarded. The particles are redispersed in 10 mL of dry toluene and transferred to a dry Schlenk flask with argon atmosphere. Then, 30 mg of AIBN and 0.65 mL of the corresponding enantiomer are added and the reaction mixture is treated with three cycles of freeze-pump-thaw to remove oxygen. The mixture is subsequently stirred at 70 °C for 20 h. Afterwards, the solvent is reduced at a rotary evaporator and the particles are precipitated by adding methanol. The mixture is centrifuged at 9000 rpm for 10 min and the supernatant is discarded. The functionalized nanoparticles are redispersed in 4 mL toluene and the cleaning procedure is repeated twice.

3.1.3 Materials

All reagents were used without further purification, unless stated differently. Silver nitrate (99.9999 %), gold(III) chloride trihydrate (>99.9 %), sodium borohydride (99 %), sodium citrate tribasic dehydrate (>99.5 %), sodium hydride (60 % in mineral oil), tannic acid (>97 %), L-cysteine (>97 %), D-cysteine (>99 %), L-glutathione (>98 %), 1-dodecene (95 %), tetrahydrofuran (anhydrous), toluene (HPLC grade), 1-phenylethanol (>97 % enantiomeric purity), allyl bromide (reagent grade) and azobisisobutyronitrile (reagent grade) were obtained from Sigma-Aldrich. Toluene was purified and dried using a Grubbs-type

solvent purification system (Innovative Technologies, Inc.). The solvents methanol, ethanol, diethylether and pentane were obtained from the faculty supply and were of technical grade. Hydrogen silsesquioxane (tradename FOx-17) was obtained from Dow Corning; the solvent was removed in vacuo, and the resulting white solid was used without further purification. Electronic grade hydrofluoric acid (49 % aqueous solution) was purchased from J. T. Baker. UPW was obtained from a Direct-Qs 5 UV purification system from Merck Millipore.

3.2 Applied Characterization Methods

3.2.1 Characterization of Chiral Silver Nanoparticles

This section gives a brief overview on the optical and materials characterization methods, which where applied to the synthesized chiral noble metal nanomaterials.
A very useful tool to qickly characterize noble metal nanomaterials is conventional UV/VIS spectroscopy, due to the surface plasmon resonances. Silver and gold are very well known metals and the particle size can be estimated by its optical properties.[154] To get definite information on morphology electron microscopy is a useful tool. Electron microscopy can be combined with EDX spectroscopy additionally, which allows to collect information on the elemental composition. XPS is also a powerful tool to obtain information on the composition of a material, as it can reveal the oxidation states of the investigated material. To investigate the optical activity CD spectroscopy is the method of choice and can be used for molecules as well as for plasmonic structures. CD spectroscopy exploits the different absorption of left- and right-handed circular polarized light, when passing a chiral agent. Chiral enantiomers exhibit a mirror image like CD spectrum.

SEM and EDX data were obtained with a JSM-7500F from JEOL equipped with an XMax detector from Oxford Instruments. Brightfield TEM images were recorded using a JEM-1400 microscope from JEOL and evaluated with ImageJ. XPS spectra were recorded on a SPECS system equipped with a Phoibos 150 2D CCD hemispherical analyzer and a Focus 500 monochromator. The detector angle was set perpendicular to the surface and the X-ray source was Al Kα. CD and UV/VIS spectra were recorded on a J-815 spectrophotometer from Jasco. Detailed experimental information can be found in section 6.1.[24]

3.2.2 Characterization of Silicon Nanocrystals

This section gives a brief overview on the optical and materials characterization methods, which where applied to the obtained SiNCs.
First IR-spectroscopy was applied, to quickly check the success of the functionalization process. The Si-H, Si-O-Si and the IR bands of the respective ligands are of interest, as they

indicate the degree of functionalization and oxidation. To gain further insight in the particles composition high resolution XPS spectroscopy was performed. By means of XPS the degree of oxidation can be determined more precisely and more important, the oxidation state of the silicon core can be checked. To completely characterize the particles their mean diameter needs to be determined, which can be achieved by using TEM. Finally, the crystallinity can be controlled using high-resolution TEM. Additionally, p-XRD can be used to get information about the crystallinity and the particle size can be estimated through the Debye-Scherrer equation.
The PL properties were investigated by a self-built fiber guided setup. Briefly, a 352 nm Ar^+ laser was used to excite the SiNCs. The PL spectra were recorded on an USB spectrometer. For time-resolved measurements, a combination of an acousto-optic modulator and a PMT was used. For wavelength-resolved measurements, the luminescence was guided through a monochromator prior to detection.

Fourier-transform infrared (FTIR) spectra were recorded on a Nicolet 8700 from Thermo Scientific. XPS was measured in a SPECS system equipped with a Phoibos 150 2D CCD hemispherical analyzer and a Focus 500 monochromator. The detector angle was set perpendicular to the surface and the used X-ray source was Mg Kα. Bright field transmission electron microscopy images were obtained on a JEOL-2010 and evaluated with ImageJ. High-resolution TEM was performed on a JEOL JEM-ARM200CF. Powder X-ray diffraction spectra were recorded on a diffractometer from Inel equipped with a curved position sensitive detector. The applied radiation was Cu Kα.
PL spectra were recorded with an Ocean Optics USB2000+ spectrometer with a wavelength range of 530–1100 nm. A HL2000 tungsten halogen light source was used as calibrated radiation source for relative irradiance measurements. Time-resolved measurements were performed with a Hamamatsu H7422-50 PMT interfaced to a Becker–Hickl PMS400 multiscalar. The used monochromator was an Acton MS2500i. The 352 nm Ar+ ion laser beam was pulsed (50 % duty cycle, 50–1000 Hz) by using an Isomet IMDD-T110L-1.5 acousto-optic modulator. For low-temperature measurements a helium cryostat from CTI Cryogenics equipped with a Cryo-con 32 temperature controller was used. The quantum yield was determined by a Quantaurus QY spectrometer from Hamamatsu.
Detailed experimental information can be found in section 6.2[95] and 6.3.[130]

3.3 Setup for Nonlinear Optical Studies

The following section is adapted from v. Weber et al.[138] and further information can be found in *Chem.Phys.Chem.*, **2018**, *19*, 1-9.
In Figure 3.1 the used optical setup is depicted. The combination of an ultrahigh vacuum

(UHV) system with laser spectroscopy allows the preparation and investigation of samples with a minimum of environmental influences. The laser setup enables the application of a linear and a nonlinear spectroscopic technique, which are surface cavity ring-down (s-CRD) and surface second-harmonic generation (s-SHG).
The main part of the UHV system is the analysis chamber with a base pressure of $1 \cdot 10^{-10}$ mbar. It is equipped with a 4-axes manipulator (x, y, z, Φ). For surface treatment, a sputter gun in combination with an electron shower ($<$ 15 eV; to neutralize non-conductive samples) is attached to the analysis chamber. To introduce and store samples a transfer chamber, equipped with a fast-entry lock and a sample magazine, is connected to the analysis chamber by an UHV gate. The attached evaporator can be used to prepare thin molecular films with a defined thickness. Therefore, a quartz crystal microbalance is used. A laser ablation cluster source is connected to the analysis chamber, which allows the in-situ deposition of small metal clusters on a chosen substrate.[80]
The laser spectroscopy setup consists of two main parts, which are the light source before the UHV chamber and an analysis part after the chamber. The light source is an optical parametric amplifier laser system with a spectral range of 210 to 10000 nm and a pulse duration of about 30 ps. A complete polarization of the monochromatic laser beam is ensured by a calcite Glan-Laser prism, before passing a photoelastic modulator (PEM), which actively controls the polarization of the laser beam. The PEM is able to generate linear polarized light and left- or right-handed circular polarized light. The necessary delay between the oscillation of the PEM and one laser shot, which defines the outcoming polarization, is set by a self-made trigger box. After passing the PEM, the laser beam is cleaned from residual second harmonic light by a 400 nm longpass filter. The laser beam is then focused on the sample inside the UHV chamber by a fused silica lens with a focal length of 300 mm. The laser spot size at the sample varies between 0.5 and 4 mm, by moving the sample towards or away from the focal point. The fundamental light and the generated second harmonic light leave the chamber and are recollimated by another fused silica lens with focal length of 300 mm. The separation of the fundamental and second harmonic beams is achieved by a combination of two rotatable Pellin-Broca prisms, followed by a monochromator. The angles of the prisms are adjusted to the wavelength by stepper motors, which are calibrated upfront. The light intensity of the fundamental beam, which is used for the power correction of the measured second harmonic signal, is detected by a photodiode located behind the first prism. The second harmonic light is detected by a PMT in the very end. A LabVIEW program controls the laser, the trigger box, the PEM, the stepper motors, the monochromator and the oscilloscope and therefore enables the full automation of a stepwise scan over a wavelength range, while switching between different polarizations for each wavelength step. It is also possible to monitor the time evolution of the second harmonic signal at a certain wavelength.
To measure s-CRD the fundamental laser beam is deflected with a 90 °C silver mirror before

reaching the first Pellin-Broca prism and is then detected by another PMT.
The optimal measurement parameters (focus and incident laser power) for s-SHG spectroscopy have to be determined and adjusted for each set of samples and were kept constant for a series of measurements. The measurement angle was always set to 70° (respective to the incident laser beam) to minimize scattering and to maximize the obtained second harmonic signal.

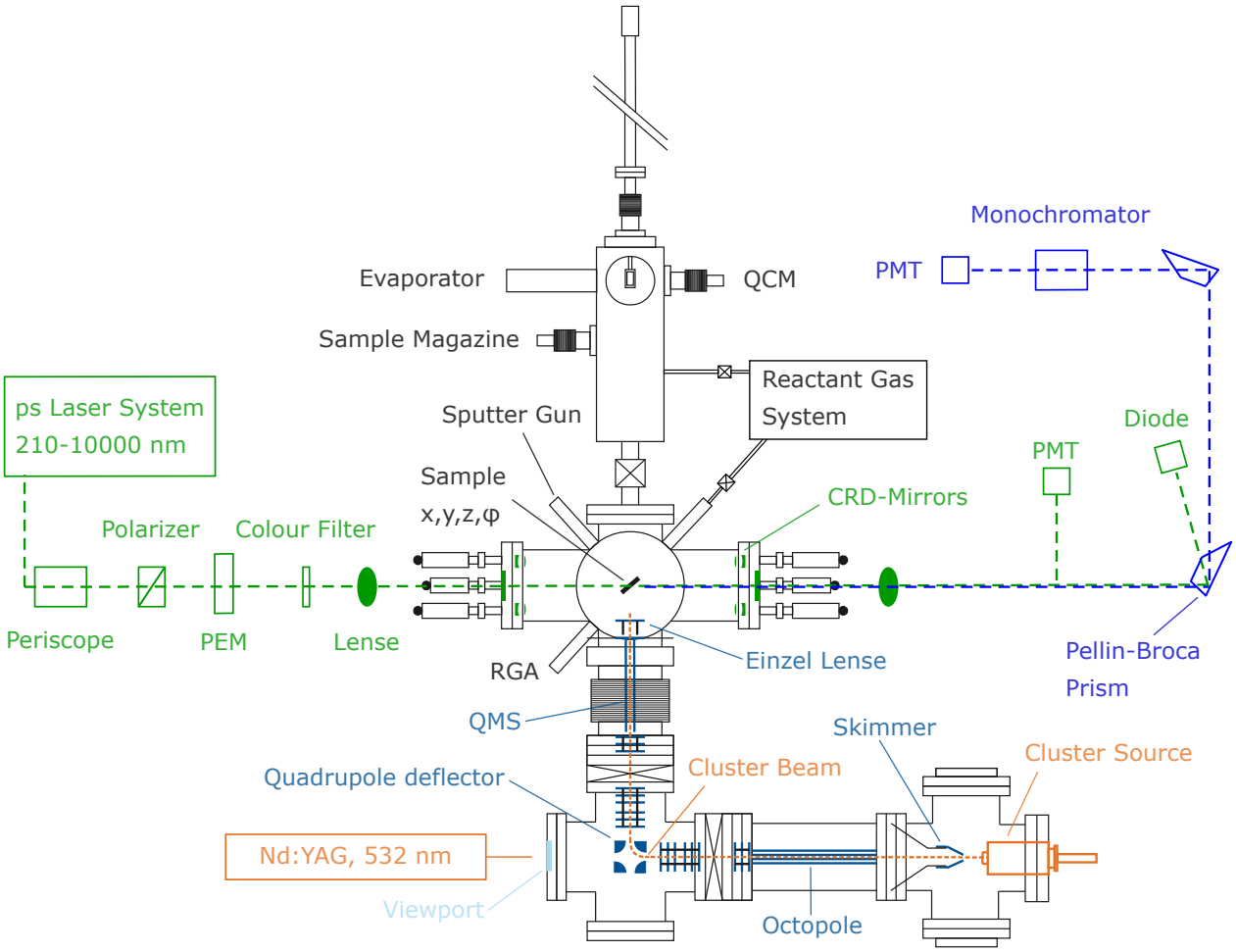

Figure 3.1: Schematic drawing of the used ultrahigh vacuum setup for optical studies. It is possible to perform surface cavity ring-down (s-CRD; green path) and surface second-harmonic generation (s-SHG; blue path) spectroscopy under very controlled conditions. Reproduced from *Chem.Phys.Chem.*, **2018**, *19*, 1-9 with permission from John Wiley and Sons.[138]

The PG401 laser system was obtained from EKSPLA. The used PEM is a II/FS42A from Hinds Instruments. The longpass filter FELH0400 was obtained from Thorlabs. The used Monochromator is an Omni-λ 150 from LOT. The installed PMT for s-SHG spectroscopy is a H9305-03 and for s-CRD spectroscopy is a H7732–10 from Hamamatsu.

4 Results and Discussion

4.1 Chiroptical Properties of Noble Metal Nanoparticles

The first part of the thesis deals with the question how chirality can be introduced in metal nanomaterials and new insights in the mechanism of chirality transfer were obtained. Noble metals were used as a model system, as their surface plasmon resonances ease the analysis of their chiroptical properties.

Chiral Silver Nanoparticles

Optically active silver nanostructures were synthesized from $AgNO_3$ in a one-step process mediated by thiol-containing biomolecules. Thus, the protecting ligand additionally acts as reducing and capping agent. This direct synthesis was performed successfully with D- and L-cysteine and L-glutathione. The chiroptical properties of the obtained nanostructures were investigated by CD spectroscopy in the ultraviolet and visible wavelength range. The obtained nanoparticles exhibit a g-value, which is about one order of magnitude larger compared to particles prepared by a conventional citrate reduction followed by a ligand exchange reaction. Although the generated structures do not show a chiral geometry, they show mirror image g-values, when D- and L-cysteine are used as capping ligand (see Figure 4.1). This implies that the underlying chirality transfer mechanism is not based on an induced structural chirality.

A time-resolved study of the reaction between $AgNO_3$ and L/D-cysteine was performed and revealed that firstly almost only very small optically active particles are present, which then steadily grow into huge particles over the course of 30 h. The growth is accompanied by an increase of the g-value. This observation and the fact that the particles formed with L/D-cysteine (Figure 4.1 c/d) possess a random shape leads us to the conclusion that the observed g-values originate from either a chiral polarisation of the plasmon resonance or a chiral footprint on the particles surface. Also a combination of both is possible, which was also proposed by Goldsmith et al.[155] in former studies.

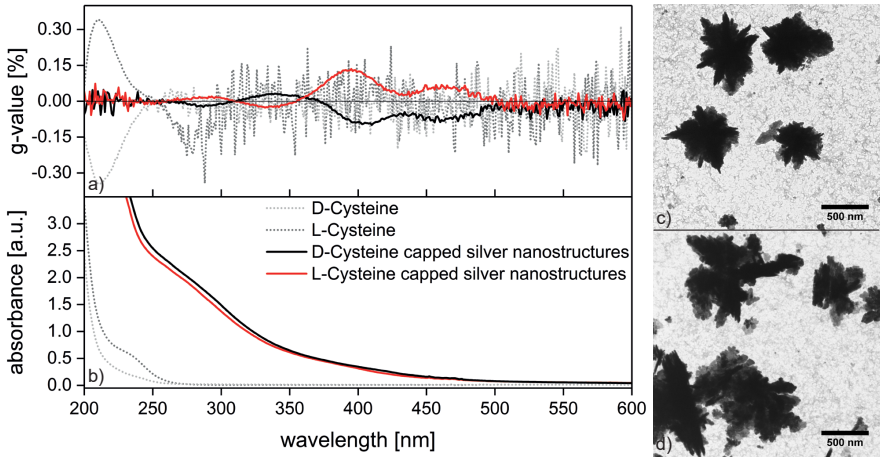

Figure 4.1: (a) g-value and (b) absorbance against wavelength for D- and L-cysteine (dotted line) and the functionalized silver particles (black: D-cysteine/red: L-cysteine). TEM images of the resulting structures using (c) L-cysteine and (d) D-cysteine. The reaction was carried out at RT.
Reproduced from *Phys.Chem.Chem.Phys.*, **2018**, *20*, 20347 - with permission from the PCCP Owner Societies.[24]

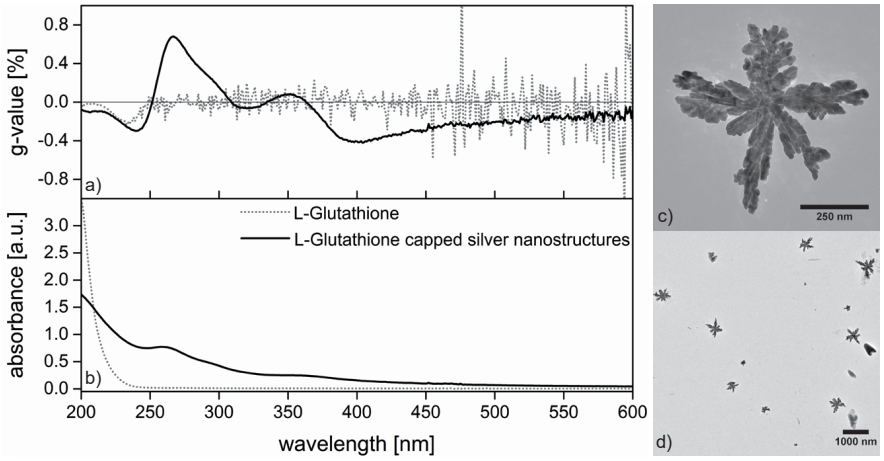

Figure 4.2: (a) g-value and (b) absorbance against wavelength for L-glutathione (dotted line) and the functionalized silver particles (black line). c) and d) TEM images of the resulting structures. The reaction was carried out at 115 °C.
Reproduced from *Phys.Chem.Chem.Phys.*, **2018**, *20*, 20347 - with permission from the PCCP Owner Societies.[24]

The dendritic structure of the obtained materials (see Figure 4.2 c) may lead to the observed enhancement of the g-value in comparison to small spherical particles, which were subsequently capped with L-glutathione. The reasons for this are probably nanogaps and apexes present in the nanostructures, which can lead to local field enhancement or 'super chiral hot spots'. These in turn enhance the measured g-value.[156,157]

The full publication with a more detailed description and analysis of the results is reprinted in chapter 6.1.

Chiral Gold Nanoparticles

Although silver and gold are both noble metals and react with thiols, they behave quite differently when treated with chiral thiol-containing amino acids. Whereas silver can be completely reduced by an amino acid, this seems not possible for gold. Therefore, an additional reducing agent was used. During the course of this project several approaches to produce chiral gold nanoparticles were pursued.
First, a simple ligand exchange reaction was performed by adding L-glutathione to already prepared gold nanoparticles, as this was successfully transfering chirality into NPs in the case of silver. To correctly interpret the results it is necessary to have a look at the optical properties of the gold precursor itself. In Figure 4.3 the absorbance and the g-value are depicted for the pure auric acid dissolved in water, for gold nanoparticles and for L-glutathione capped gold nanoparticles. It is obvious that there is no optical activity in pure auric acid and it shows almost no absorbance above 400 nm. A local maximum is observed around 300 nm, which can be attributed to charge transfer between the metal and the surrounding ligands. A comparison of neat gold nanoparticles and L-glutathione capped gold nanoparticles shows that upon addition of L-glutathione a red shift of the SPR from 520 to 550 nm occurs, which can be caused by the attachement of thiols or particle agglomeration (see Figure 4.3 c/d).

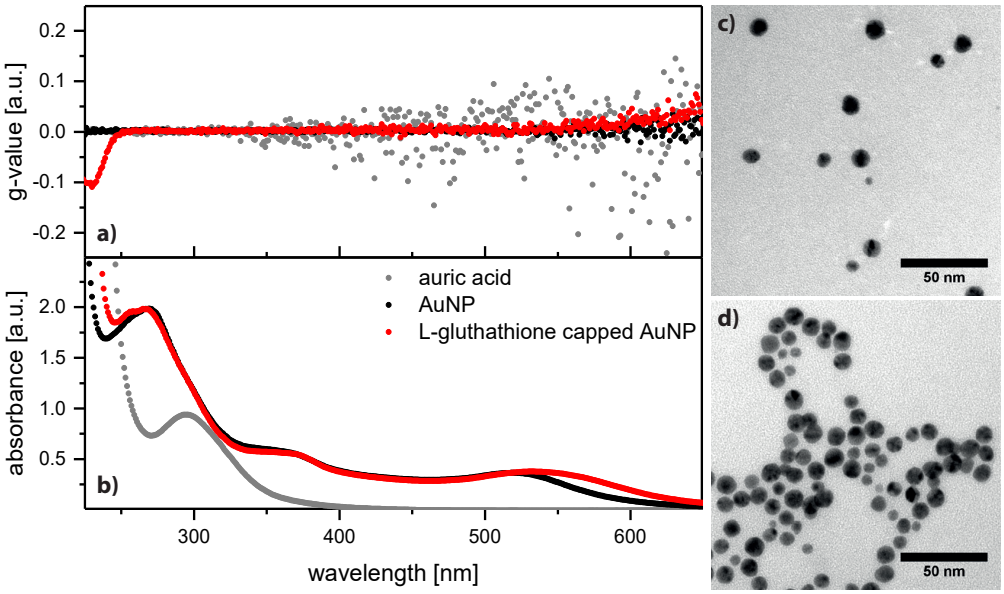

Figure 4.3: a) g-value and b) absorbance for for pure auric acid (grey) citrate stabilized gold nanoparticles (black) and L-glutathione capped gold nanoparticles (red). TEM images of the gold nanoparticles are depicted in c) and d) for the citrate stabilized and L-glutathione capped particles respectively.

The rest of the spectrum remains unchanged upon addition of L-glutathione. The peaks around 380 and 270 nm are interband transitions and are thus less affected by changes at the particle surface. The peak at 380 nm can be attributed to a transition from the uppermost occupied d state to states just above the fermi level and the peak around 270 nm originates

from transitions from lower d states into the conduction band.[158] The functionalized particles do show small optical activitiy below 250 nm, which can be attributed to the ligand L-glutathione. The SPR of gold has a much lower polarizability compared to silver, but the strength of Au-S bond is higher than Ag-S.[159] In contrast to AgNPs the SPR of the AuNP is not getting quenched by addition of L-glutathione. However, also no optical activity is induced.

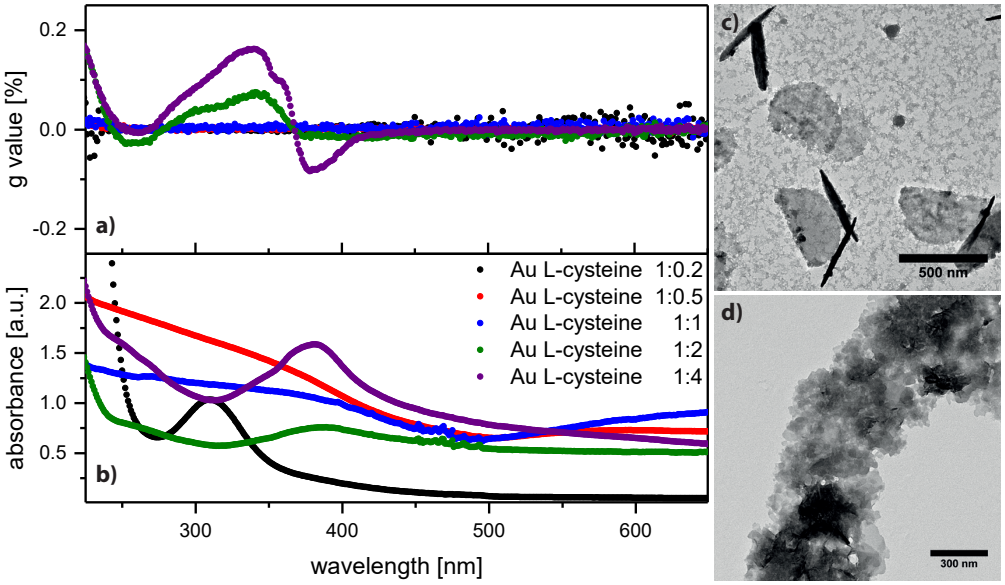

Figure 4.4: a) g-value and b) absorbance for different molar ratios of auric acid and L-cysteine. TEM images of the resulting structures are depicted in c) and d) for a ratio of 1:1 and 1:2 (Au:L-cysteine) respectively.

The next experiments were performed by a direct reduction of auric acid using L-cysteine, or L-cysteine in presence of a reducing agent. The reaction of auric acid with L-cysteine (Figure 4.4) results in white cloudy suspensions with a faint yellow, blue or red color. The different gold to cysteine ratios lead to very different results. The optical properties of a ratio of 1:0.2 (Au:L-cysteine) are almost identical with the neat gold solution, whereas a ratio of 1:0.5 is already leading to a very broad absorbance band from 225 to 500 nm and a small SPR peak around 580 nm. A ratio of 1:1 is still similar, but with a more pronounced and red-shifted SPR. Suprisingly, adding more cysteine again leads to a very different absorption spectrum with a pronounced peak at 390 nm. The material is also showing some optical activity between 290 and 400 nm. The sample made from a ratio of 1:4 is similar to 1:2 but with an even more pronounced absorption peak at 390 nm and optical activity between 300 and 420 nm. In the wavelength range of the SPR (580 - 800 nm) no optical activity is observed for any sample.

TEM images were obtained for the samples with ratios of 1:1 and 1:2 (Au:L-cysteine) to investigate the origin of the then arising optical activity. In Figure 4.4 c the TEM image

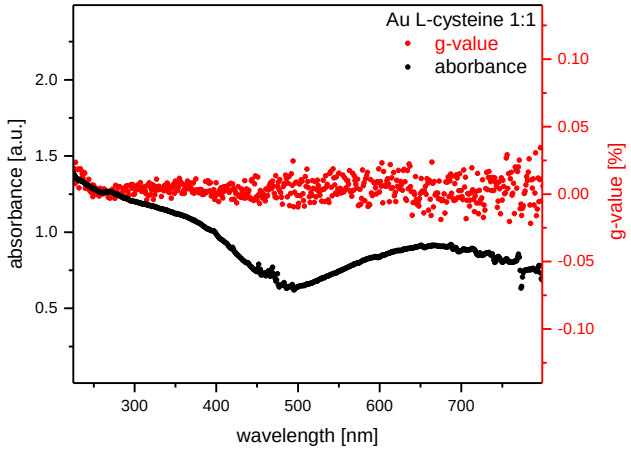

Figure 4.5: Absorbance and g-value for pure the gold nanosticks obtained by a ratio of 1:1 (Au:L-cysteine). A strong absorption over the entire wavelength range can be observed and a local maximum around 680 nm is visible. The material shows no remarkable optical activity over the measured wavelength range.

for a ratio of 1:1 is shown and the formation of sticks, accompanied by thin flat structures is visible. The stick like structure can explain the red-shift of the SPR peak position to around 680 nm (see Figure 4.5).[160] In the case of a ratio of 1:2, large but less dense dendritic structures were obtained. These are very similar to the structures, which were observed in the case of silver nitrate as precursor and cysteine as capping agent (see Figure 4.1 d). Consequently, these kind of structures display optical activity in the case of both silver and gold.

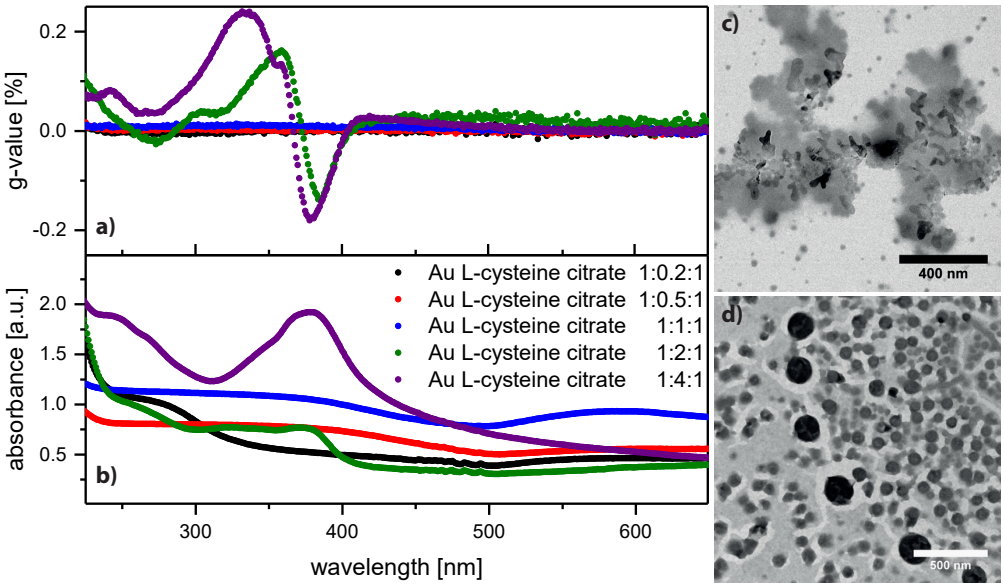

Figure 4.6: (a) g-value and b) absorbance for different molar ratios of auric acid, L-cysteine and trisodium citrate as additional reducing agent. TEM images of the resulting structures are depicted in c) and d) for a ratio of 1:2:1 and 1:4:1 (Au:L-cysteine:citrate) respectively.

After 2 h reaction time, trisodium citrate was added to a part of the previously prepared mixtures and they were stirred for 24 h. The optical properties of the resulting solutions and TEM images for reactant ratios of 1:2:1 and 1:4:1 (Au:L-cysteine:citrate) are depicted in Figure 4.6 c and d. The overall behavior is similar to the samples with just L-cysteine added, with some exceptions. For the lowest ratio of gold to cysteine, the signals from the neat gold solution almost vanished and a continuous weak absorbance over the whole wavelength range appeared. The highest gold to cysteine ratio yields spherical particles with sizes around 50 and 100 nm, but the absorbance spectrum does not show the typical plasmon peak around 550 nm. However, the peak at 390 nm is even more pronounced and the optical activity increased further. For a gold to cysteine ratio of 1:2, a cotton effect around 400 nm appeared in the optical activity after the addition of trisodium citrate. When comparing the structure for reactant ratios of 1:2 and 1:2:1, it appears that the structures gets even less dense on the addition of citrate, but the branched structure remains. The subsequent addition of citrate is in summary increasing the optical activity of some samples, but is not leading to major changes in its optical properties.

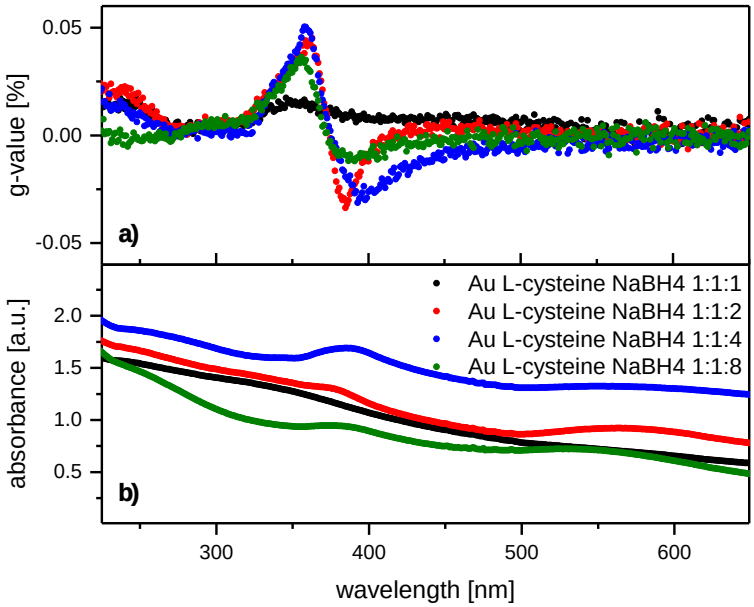

Figure 4.7: (a) g-value and b) absorbance for different molar ratios of auric acid, L-cysteine and sodium borohydride as additional reducing agent (ratio of 1:1:x). Small optical activity is observed around 400 nm.

In the next step $NaBH_4$ was introduced as reducing agent, as it reacts stronger at room temperature than trisodium citrate does. Nevertheless, most of the solutions remained white and cloudy. Three reaction series with a different ratio of gold to cysteine and an increasing amount of reducing agent were performed. In the first series the gold to cysteine ratio was kept constant at 1:1 and $NaBH_4$ was varied from 1 to 8 times the molarity of gold (Figure 4.7). The two subsequent reaction series were performed in the same manner, but the cysteine ratio was increased to 2 and 4 accordingly. Within the first experimental series,

the obtained optical properties are similar for all of the different amounts of $NaBH_4$. It starts with a broad and undefined absorption over the entire wavelength range, whereby two more features around 400 nm and 580 nm appear with increasing amount of $NaBH_4$. However, only the peak around 400 nm is displaying some optical activity. This observation is very similar to the previous samples.

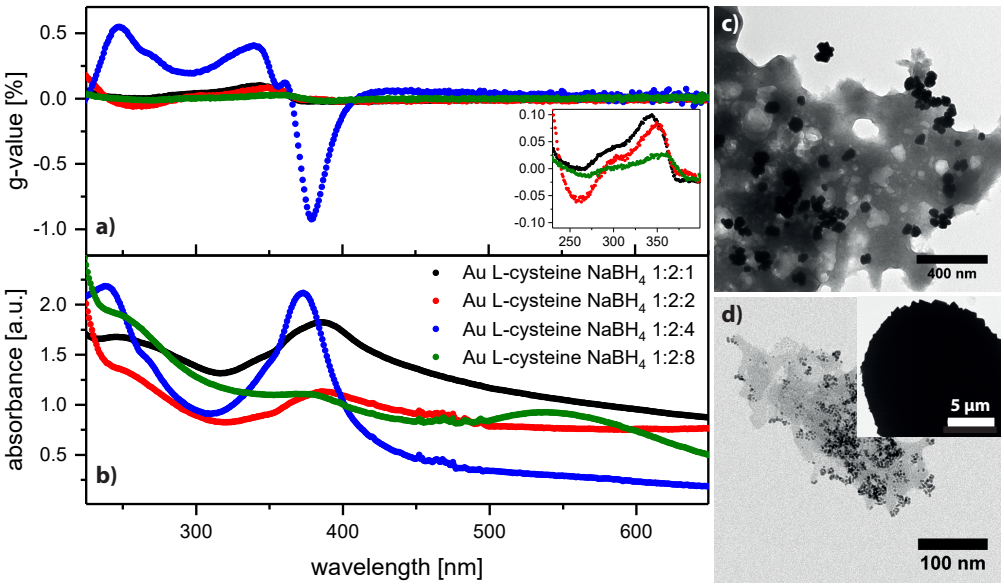

Figure 4.8: (a) g-value and b) absorbance for different molar ratios of auric acid, L-cysteine and sodium borohydride as additional reducing agent (ratio of 1:2:x). Small optical activity is observed around 370 nm (around 0.2 %). The sample with a ratio of 1:2:4 exhibits an outstanding optical activity around 380 nm (up to -0.9 %). TEM images of the resulting structures using reactant ratios of (c) 1:2:1 and (d) 1:2:4. The inset in part a) shows an enlargement of the g-value of the less optically active samples.

The next series, which is depicted in Figure 4.8, was performed with a reactant ratio of 1:2 (Au:cysteine) and varying amounts of $NaBH_4$. This yields similar results as the series with a ratio of 1:1. However, a reactant ratio of 1:2:4 yields a materials with a very high optical activity around 390 nm. The g-value reaches a value of -1 %, which is very high for this kind of material.[23,24,110,161] The absorption spectrum of this sample exhibits a distinct absorption peak at 390 nm, but no SPR is observed at higher wavelengths. TEM images of the material (Figure 4.8 d) reveal that the sample consists mainly of large spherical particles with diameters of around 15 µm. Additionally, spots consisting of very small particles in a gel like environment could be found on the TEM grid. This leads to the conclusion that small ligand capped particles merged to some large particles, like it was the case for $AgNO_3$ and cysteine. The microstructure of these large particles could not be investigated, as they were too dense.

The material obtained by a ratio of 1:2:1 also exhibits the peak around 390 nm, which also shows optical activity. In contrast to the sample with a ratio of 1:2:4 a broad absorbance at higher wavelengths can be observed. TEM images (Figure 4.8 c) reveal that the sample

consists of small particle agglomerates, which are surrounded by a gel like material.
It is remarkable that the sample with the highest amount of $NaBH_4$ added shows a pronounced surface plasmon resonance around 550 nm, but exhibits the least optical activity around 390 nm in this series of experiments.

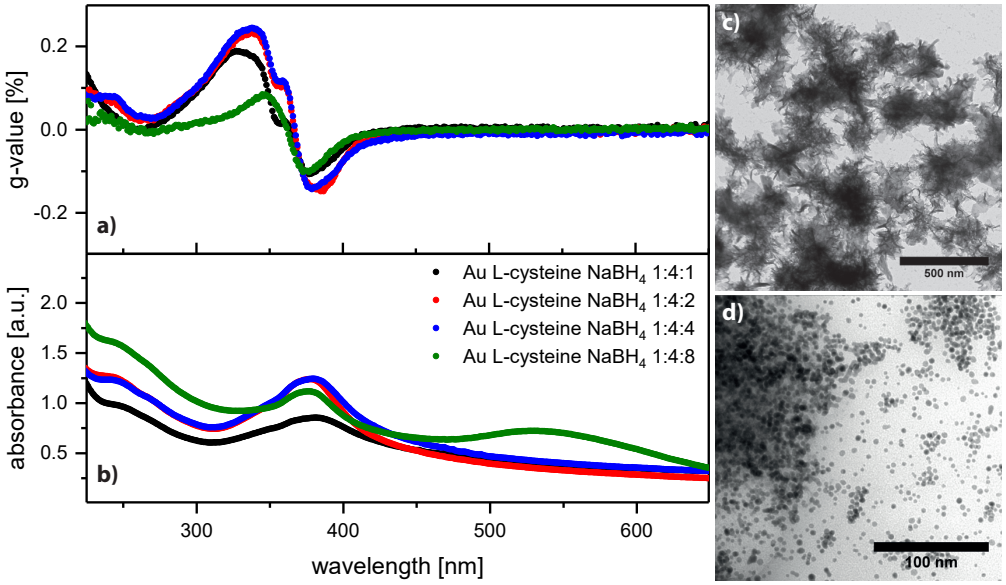

Figure 4.9: (a) g-value and b) absorbance for different molar ratios of auric acid, L-cysteine and sodium borohydride as additional reducing agent (ratio of 1:4:x). Small optical activity is observed around 360 nm. The samples with a ratio of 1:4:2 and 1:4:4 show the most distinct optical activity. TEM images of the resulting structures with reactant ratios of (c) 1:4:4 and (d) 1:4:8.

The last series of experiments was performed with a ratio 1:4 (Au:cysteine) and a variable amount of $NaBH_4$. These samples exhibit very similar optical properties except the one with a ratio of 1:4:8, which shows a pronounced SPR around 550 nm additional to the peak around 390 nm (see Figure 4.9). Again the sample with the highest amount of reducing agent shows the smallest optival activity. TEM images were recorded for reactant ratios of 1:4:4 and 1:4:8 to examine the difference in these samples. The sample with the highest ratio of reducing agent consists only of very small spherical particles with a diameters between 5 and 10 nm, whereas the sample with half the amount of $NaBH_4$ consists of large fuzzy structures. This implies that depending on the amount of cysteine and $NaBH_4$, very different structures and maybe also different oxidation states of the Au are present.
In a previous work in this field, it was proposed that upon addition of cysteine a polymer like Au-sulfur structure is formed, in which the gold is not fully reduced. In their case, this polymer is further reduced by additon of $NaBH_4$, leading to spherical particles. This was also observed in this study for a ratio of 1:4:8. However, the sample with a ratio of 1:2:4 is outstanding, as it exhibits a much higher g-value than all the other investigated samples. This leads to the conclusion that the reactant ratio is crucial to generate a large optical activity. However, no clear trend could be obtained within this study.

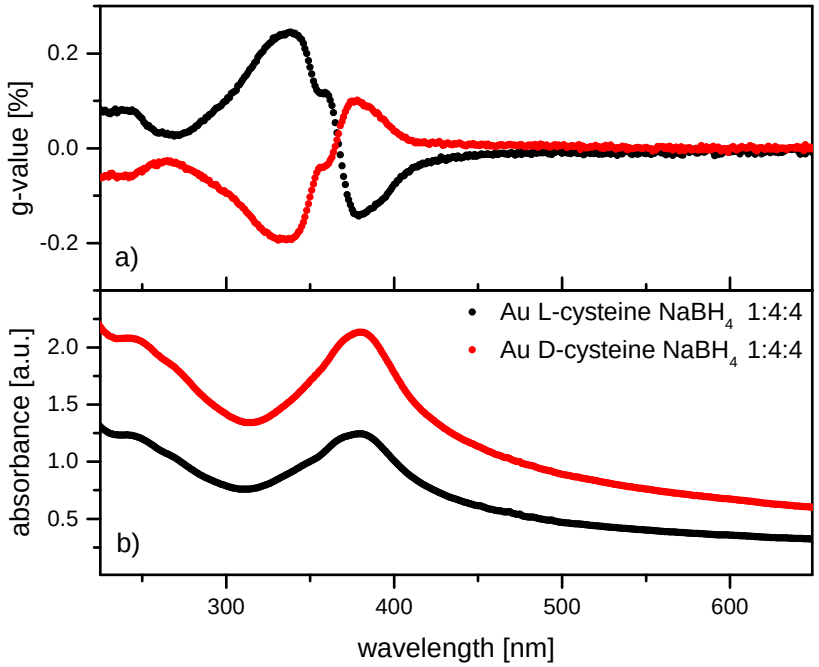

Figure 4.10: (a) g-value and b) absorbance for the same molar ratio of auric acid, L-cysteine or D-Cysteine and sodium borohydride as additional reducing agent (ratio of 1:4:4). Mirror image like behavior can be observed, when using the two enantiomers L- and D-cysteine as chiral agent.

Finally, one experimental set with L- and D-cysteine was conducted. The resulting optical properties are depicted in Figure 4.10 and the g-values shows a mirror image like behavior. This confirms reproducibilty and also allows some insight in the underlying process. As the different reactant ratios lead to many different structures, which exhibit similar g-values, the origin of the observed chirality is most likely not due to a geometrical chirality, as was found in recent work of Lee et al.[26] It is possible that the ligand is leaving a chiral footprint on the materials surface or the surrounding electric field is polarized. However, as the SPR is not showing optical activity in any case it seems most probable that a chiral footprint is the reason for the observed phenomena. The results obtained in this study do not fit to the previous study on silver. In the case of silver optical activity was observed up to 500 nm, which is clearly not related to interband transitions. The sample with a ratio of 1:4:8 (Au:cysteine:$NaBH_4$), which consists of very small spherical particles, shows an absorption peak around 390 nm and a well defined SPR. However, only the peak at 390 nm is showing optical activity. It is known that the polarizability of gold is 5 to 10 times less than the polarizability of silver, depending on the structure.[162] It may be that the interaction of gold and cysteine is too weak and thus not suitable to induce optical activity in the SPR of gold. This was also found in other studies. In a study of Gautier et al.[110] only some thiol containing biomolecules, such as L-glutathione or N-isobutyryl-L-cysteine were able to introduce chirality in the investigated gold nanoparticles.
To clarify the mechanism of chirality transfer in gold further experiments are necessary. This

may include the usage of more different chiral molecules or other reducing agents. A very interesting approach is the use of HEPES, which is one of the "good buffers". The reaction of auric acid and HEPES leads to star-shaped gold nanoparticles.[39] It was found that the piperazine ring in HEPES is able to generate nitrogen-centered free radicals, which can then reduce the gold ions ($AuCl^{4-}$).[40] A combination of HEPES and different chiral thiols seems promising for the generation of chiral gold nanomaterials, as the reaction is rather slow and gives the opportunity for directed growth.[39]

4.2 Studies on the Photoluminescence of Silicon Nanocrystal Ensembles

In the second part of the thesis the optical properties of SiNC ensembles are targeted with focus on their size-dependent emission. Thus, detailed analysis was performed on samples with mean particle diameters between 3 and 9 nm.

Fundamental Photoluminescence Properties of Silicon Nanocrystals

The purpose of the following work is to establish a steady approach to measure, model and interpret the luminescence dynamics of SiNCs. This might help to understand the variety of often conflicting results in the literature and to increase the consistency between different measurements. It thus contributes to a better understanding of the luminescence mechanisms in SiNCs.[95]

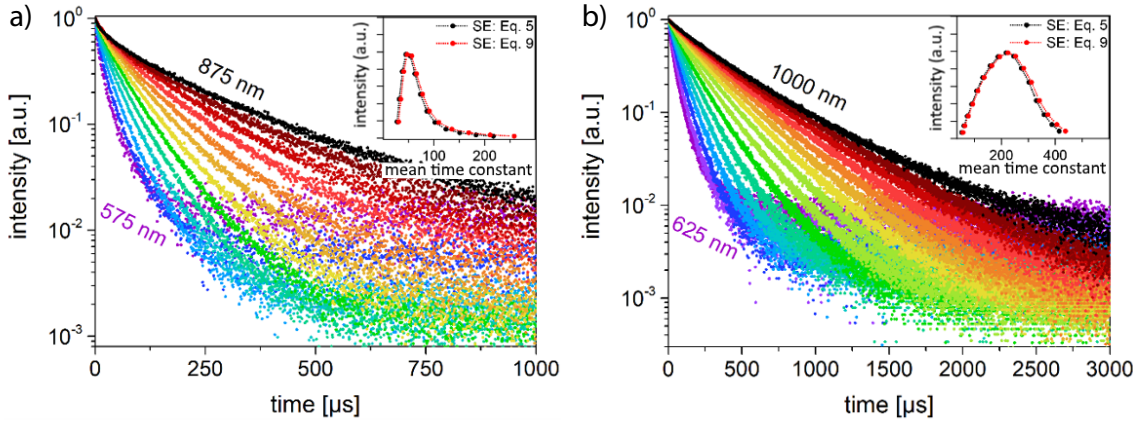

Figure 4.11: Monochromatic PL decays. a) PL decays for the small SiNCs at specific emission energies in 25 nm intervals. b) PL decays for the large SiNCs at specific emission energies in 25 nm intervals. The insets display the luminescence intensity plotted against the calculated mean decay time at a certain wavelength.
Adapted from M. Jakob, A. Aissiou, W. Morrish, F. Marsiglio, M. Islam, A. Kartouzian, A. Meldrum, Nanoscale Res. Lett. 2018, 13, 383.[95]

The luminescence decays are modeled with different functions in the literature, which also

alters the obtained lifetimes. Thus, a detailed analysis of two different SiNC ensembles was performed (Figure 4.11). Thereafter, the luminescence decays of SiNC ensembles were modeled with the most commonly applied fit functions. This includes two stretched exponential and one lognormal function. The lifetime distributions were derived from the model fits and compared to the result of quadrature frequency-resolved spectroscopy (QFRS), which is able to directly extract the luminescence lifetime distribution from a sample. In Figure 4.12 the obtained lifetime distributions are displayed for the two different samples.

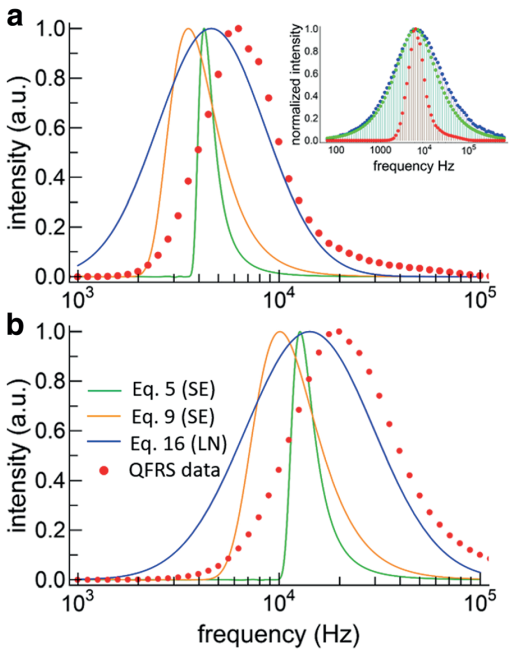

Figure 4.12: Lifetime distributions. (a) Lifetime distributions for large SiNCs obtained from fitting the ensemble TRS data with the two stretched exponential (SE) models and the lognormal (LN) model. The deconvolved QFRS data is also shown (red points). The inset shows the raw QFRS data for this sample (blue), the response function (green) and the deconvolution (red). (b) Lifetime distributions obtained by model fitting the TRS data (lines, same color scheme for both graphs) and QFRS (red points) for the small SiNCs.
Reproduced from M. Jakob, A. Aissiou, W. Morrish, F. Marsiglio, M. Islam, A. Kartouzian, A. Meldrum, Nanoscale Res. Lett. 2018, 13, 383.[95]

The QFRS data yield the lifetime distribution directly without the need to assume a model a priori (Figure 4.12 red dots). For both samples, the obtained lifetime distribution is broad and in the case of the large SiNCs, slightly skewed towards high frequencies. The small SiNCs show a nearly symmetrical lifetime distribution. The lifetime distributions obtained from the two stretched exponential models (orange and green curves) and the lognormal model (blue curve) are also plotted in Figure 4.12. The three decay models yield different distributions and for both samples the QFRS peaks at a higher decay rate. This may seem surprising, but the same effects have been observed for CdSe nanocrystal ensembles.[163,164] It was shown, that the time-resolved spectroscopy (TRS) decay curve for CdSe NCs was sensitive to the

excitation pulse duration. Shorter pulses accentuate the shorter lifetimes and the other way round for long pulses. Furthermore, the mean lifetimes obtained by long-pulse duration techniques were a factor of 3-4 times longer than those obtained by phase measurement. This is due to preferential excitation of the long-lived population in steady-state excitation[164].
In summary, FRS accentuates the short-lived components of the ensemble's decay more than steady-state TRS does. This may cause the difference in the obtained peak frequencies. Despite these differences, FRS appears very suitable to uncover the distribution of lifetimes in SiNC ensembles, as the lifetime distributions are obtained by direct measurement rather than by an assumed model. Another crucial point is the detector response function, which affects both the QFRS and TRS data. Indeed, measuring the ensemble decay with an avalance photodiode and with a PMT setup yielded mean decay times that were different by a factor of around 2, no matter which fitting model was applied. However, as the detector responsivity also affects the choice of the best fitting TRS model, FRS is more confident to use in this regard, too. A possible solution for this problem is the application of monochromatic TRS. As depicted in the insets of Figure 4.11, both stretched exponential fits yield the same results for monochromatic measurements. However, this is a time consuming approach and a sophisticated setup is necessary.

The full publication with a more detailed description and analysis of the results is reprinted in chapter 6.2.

The Role of Ensemble Effects in the Photoluminescence of SiNCs

In the next project the temperature-dependent PL of alkyl-capped SiNC solids with mean diameters between 3 and 9 nm was analyzed. The PL properties were evaluated for temperatures between 41 and 300 K. The well-known blue shift of the PL maximum at low temperatures decreases with increasing nanocrystal diameter and finally becomes a red-shift for SiNCs with an average diameter larger than 6 nm. SiNCs with an average particle diameter of 2.92, 3.89 and 5.49 nm showed a blue-shift of their emission maxima at lower temperatures, whereas a red-shift was observed for the 7.19 and 8.67 nm SiNCs (Figure 4.13).[130]
This implies that the observed shifts cannot be explained by bandgap widening solely, as is commonly assumed. To obtain more insight into this phenomenon TRS was performed on all samples. It revealed that the small sized SiNC ensembles are more strongly influenced by low temperatures than the large sized SiNC ensembles are. This manifests in a 8-fold increased lifetime at low temperatures for the smallest SiNCs and no difference in lifetime for the largest SiNCs. This can be explained by a larger quantum yield, a higher absorption cross section and a longer PL lifetime for larger SiNCs. These effects lead to an earlier saturation of the larger NCs within the population, effectively causing a blueshift of the PL peak.
The increasing red-shift upon cooling may be caused by energy transfer between particles

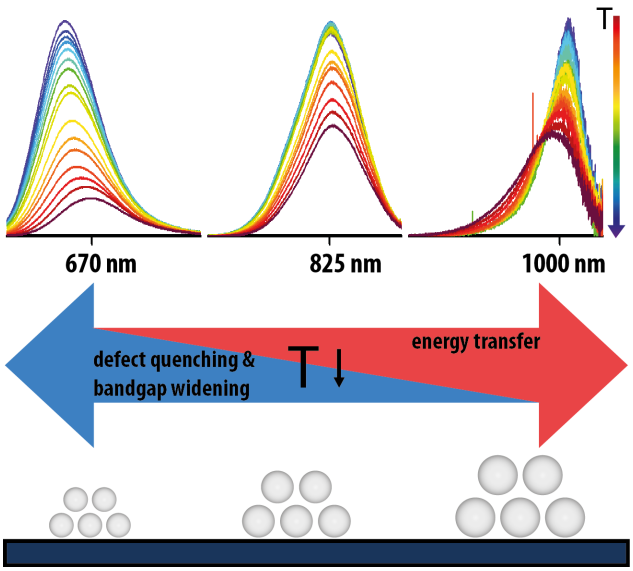

Figure 4.13: The found temperature dependency of the PL of differently sized SiNC ensembles. Ensembles with small mean diameter show a blue-shift of their emission upon cooling, whereas ensembles with a large mean diameter show a red-shift. This behavior cannot be explained by bandgap widening solely and a combination of the latter, saturation effects at the low energy side and energy transfer is proposed to produce the observed behavior.
Reproduced from *Chem. Eur. J.*, **2019**, *25*, 1-8 with permission from John Wiley and Sons.[130]

within an ensemble. This was already referred as a present effect in SiNC ensembles in other studies.[165,166] A time- and wavelength-resolved experiment on two SiNC samples in dispersed and drop-cast form was performed. It indeed confirmed that energy transfer from small to large particles happens within the ensembles, as the difference in the measured decay rates is increasing as a function of increasing emission energy. A simple emission and reabsorption mechanism would not affect the PL lifetime, whereas FRET is usually accompanied by a shortening of the donor lifetimes. This effect was additionally less pronounced for smaller sized SiNC ensembles and thus fits very well into the observed trend.

We showed, that bandgap widening, which is commonly assumed to play the main role in the low-temperature PL of SiNCs cannot explain the observed trends and we propose that a combination of bandgap widening, saturation effects and energy transfer cause the observed trend for the herein investigated samples.

The full publication with a more detailed description and analysis of the results is reprinted in chapter 6.3.

4.3 Nonlinear Optical Spectroscopy and Chiral Semiconductors

In the last part of the thesis semiconductor nanomaterials were investigated by s-SHG and SHG-CD. The combination of chirality and semiconductor nanomaterials is of special interest, as it might lead to new functional hybrid materials and subsequently new applications. Furthermore, the investigation of indirect semiconductors with conventional CD spectroscopy is hampered. This justifies the use of a more sophisticated technique such as SHG-CD.

4.3.1 SnIP - An Inorganic Double Helix

SnIP is an inorganic double helical material, which was discovered by Pfister et al.[167] recently. It consists of SnI^+ and P^- helices interpenetrating each other (see Figure 4.14). The single rods are either left (M-helix) or right-handed (P-helix) and have opposite chirality. However, the unit cell contains both helices leading to a racemic mixture of left and right handed double helices. SnIP shows high flexibility and also PL can be observed. It is a promising candidate for semiconductor applications like flexible devices or in energy conversion processes, but therefore its optical properties have to be investigated extensively.[167]

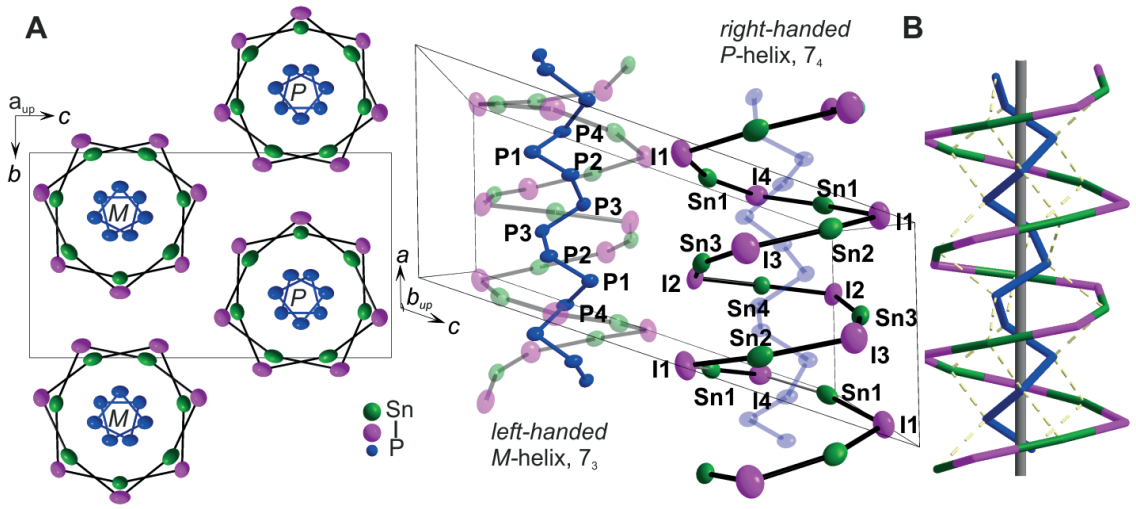

Figure 4.14: A) Crystal structure sections projected along the a and b axis of SnIP. [SnI] and [P] helices are forming a double helical SnIP strand. B) Schematic representation of the double helix arrangement and the intrahelical Sn–P interaction. Reproduced from *Adv. Mater.*, **2016**, *28*, 9783-9791 with permission from John Wiley and Sons.[167]

Optical spectroscopy was performed on a Lambda 650S from Perkin Elmer equipped with an 150 mm integration sphere (Spectralon R). This allows the measurement of the pure absorption without scattering losses, as these will also reach the detector and are also detected as transmitted light. This is particularly useful for the measurement of indirect bandgap semiconductor materials, as they exhibit a rather small absorption. The obtained UV/VIS

spectrum (Figure 4.15 a) displays a typical semiconductor spectrum, in which the absorption starts to increase towards smaller wavelenghts and keeps constant above the bandgap.[168] It does not absorb above 700 nm and exhibits a sigmoidal increase in absorption between 700 and 600 nm. A more detailed analysis of the material revealed that it exhibits a direct and an indirect bandgap at 1.86 and 1.8 eV respectively.[167]. The obtained SHG spectrum follows the same course. Consequently, the used SHG setup is also suitable for the analysis of semiconductor materials.

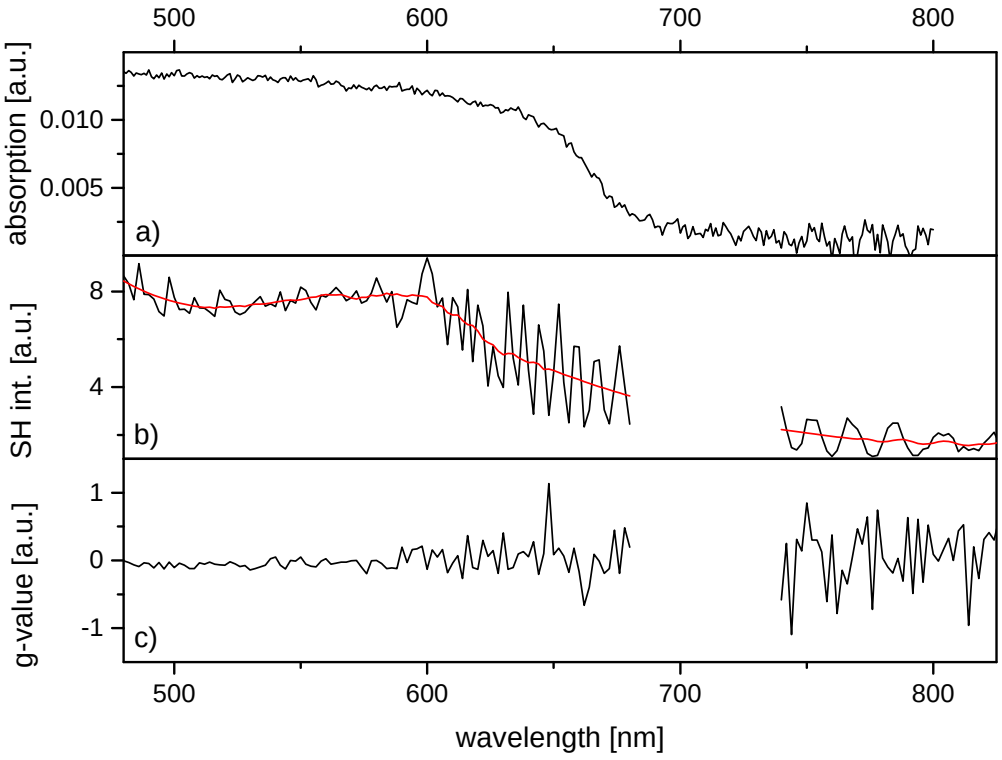

Figure 4.15: Optical and chiroptical properties of SnIP: a) Absorbance measured on an UV/VIS spectrometer equipped with an integrating sphere, b) wavelength-dependent SH intensity and c) obtained g-value from SHG-CD measurements. The SHG spectrum yields the same spectral shape than UV/VIS.

Additionally, it allows to obtain information about the optical activity. This is not possible with commercial CD spectrometers, as these are usually not equipped with the necessary integrating sphere. However, some custom built CD spectrometers equipped with an integration sphere do exist.[169,170]. SHG-CD has the inherent advantage of being very sensitive, which allows to measure the optical activity of molecules in the sub-monolayer regime.[138] Also a measurement in reflection mode can be realized, so that in principle any material can be investigated. The oscillations, which arise at fundamental wavelength larger than 600 nm, originate from interferences of second harmonic light generated at the front and back surface of the glass slab, because Bk7 becomes transparent in this wavelentgh range. In Figure 4.15 c the g-value obtained from SHG-CD measurements is shown and no optical activity was observed within the measured wavelength range. This is not surprising, as the unit cell of SnIP

contains both the left and right handed double helix. With that, the excess of one enantiomer on the particle surface levels out for the ensemble of needles. Nevertheless, it is apparent that SHG-CD spectroscopy can be used to investigate semiconductor nanomaterials.

4.3.2 Second Harmonic Generation on Silicon Nanocrystals

In a subsequent project, SHG spectroscopy was applied to the previously prepared SiNCs. These are capped with dodecane and exhibit diameters between 3 and 90 nm. They were all measured with the same experimental settings. It can be seen in Figure 4.16 that the efficiency of SHG is varying with the particle size. SiNCs with sizes between 7.5 and 50 nm are yielding the highest amount of signal.

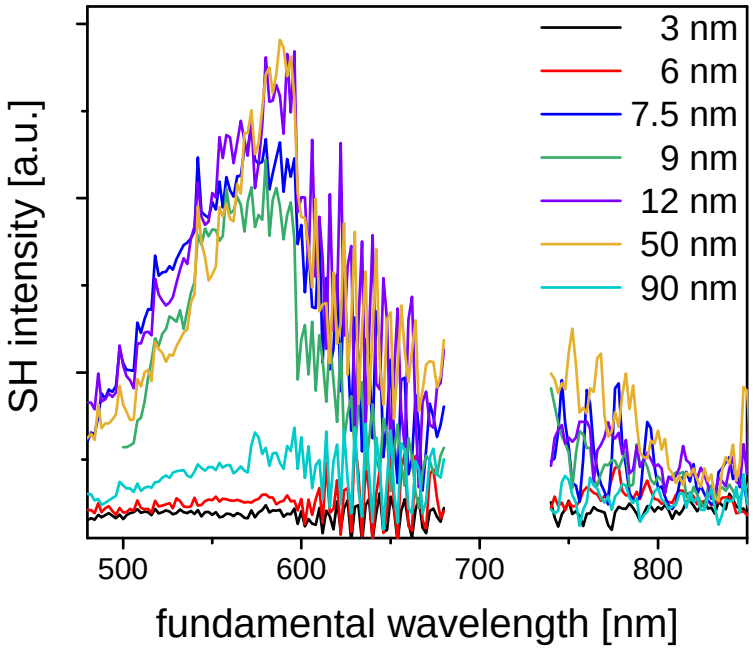

Figure 4.16: SHG spectra for different sized SiNCs as a function of the fundamental laser wavelength. The samples were prepared by drop-casting and the measurement was performed within the UHV chamber in transmission mode.

The peak position is hardly changing, what indicates that the same transition is excited for all samples. With the second harmonic peak intensity being around 600 nm, this means that the shoulder arising around 300 nm in UV/VIS might be the exited transition (see Figure 4.17). Above 9 nm diameter the peak shape in UV/VIS is changing, to a more semiconductor like spectrum. Quantum confinement in SiNCs is present up to 9 nm in diameter only and thus larger particles behave more bulk like, which was also observed within this study.[171,172] However, it is not yet clear why the very big particles with a size of around 90 nm are hardly generating SH signal, despite their UV/VIS spectrum being very similar to the spectrum of 50 nm SiNCs. One possible explanation is their higher absorption cross section and additionally less interaction with the support. This may lead to light-induced

desorption of the material during the measurement.

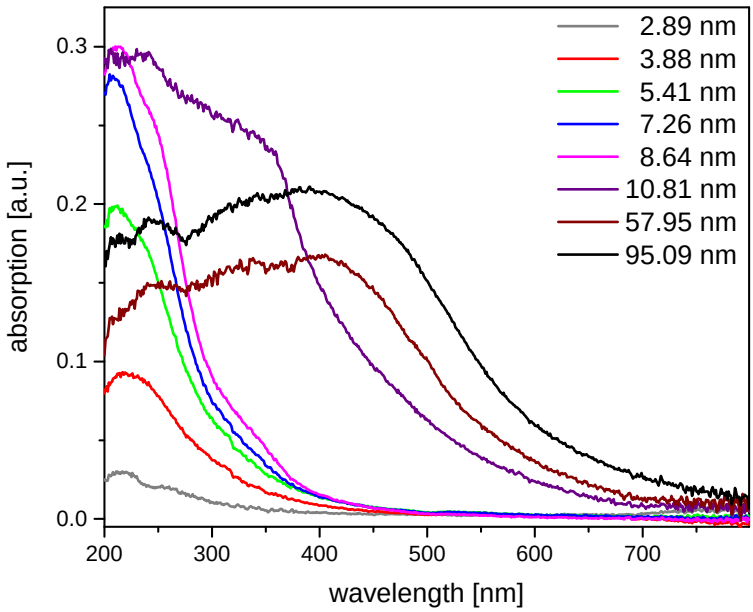

Figure 4.17: UV/VIS spectra between 200 and 800 nm for different sized SiNCs measured on a spectrometer equipped with an integration sphere. The measurement was performed in diffusive transmission mode and therefore the pure absorption of the SiNCs was measured.

Silicon is an indirect bandgap semiconductor, which was also proven for SiNCs.[89] In summary, it is possible to investigate SnIP and SiNCs by means of SHG. This means in turn that the optical properties of direct as well as indirect semiconductors can be investigated with SHG. This opens the possibility to get more insight in chiral semiconductor systems, as SHG can be extended to SHG-CD, using circular polarized light like previously mentioned.

4.3.3 Chiral Silicon Nanocrystals

The hydrogen-terminated SiNCs can be functionalized with terminal alkenes utilizing the hydrosilylation reaction. This leads to silicon particles capped with alkanes and makes them soluble in organic solvents such as toluene or benzene. However, there is only a very limited range of chiral terminal alkenes available. Consequently, (R/S)-(1-(allyloxy)ehtyl)benzene was synthesized from (R/S)-phenylethanol through a simple substitution reaction using allylbromide. In order to do so, phenylethanol is deprotonated and acts as a nucleophile. It attaches to allylbromide, while the bromide is eliminated. The chiroptical properties of the newly created molecule were characterized by means of CD spectroscopy and optical rotation. The resulting CD and absorbance spectra are depicted in Figure 4.18.

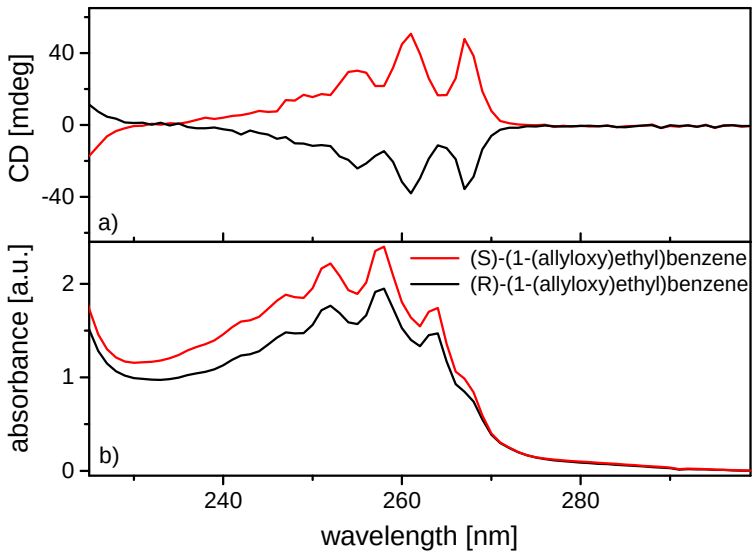

Figure 4.18: (a) CD and b) absorbance for the two synthesized organic ligands (R/S)-(1-(allyloxy)ehtyl)benzene. Above 280 nm no absorbance and optical activity is observed.

The UV/VIS spectrum (Figure 4.18 b) shows an onset around 270 nm with a maximum around 255 nm. The absorption band shows 7 features, which can be attributed to different vibronic transitions and a second absorption band is arising towards 225 nm. The CD spectrum displays only 4 distinct features, whereby the first one is located around 268 nm and the last one around 250 nm. Additionally, a zero crossing was observed around 233 nm, which fits very well to the local minimum between the two absorption bands. In general, the two enantiomers exhibit a mirror-imaged CD spectrum as expected.

The specific optical rotation of the R and S enantiomer was determined as +72.42 and -58.50. The difference in optical rotation can be attributed to impurities within the S enantiomer, which are most likely solvent residues. The specific optical rotation for the capped SiNCs was measured in the same manner and was determined as +26.64 and -29.19. This means, that the degree of functionalization is very similar for both SiNC samples, as the specific rotation is related to the total mass of the material.

CD spectroscopy was also performed on the 3 nm SiNCs functionalized with the R enantiomer. The obtained spectra are depicted in Figure 4.19. The absorbance shows the typical featureless increase of the SiNCs, whereas the ligand appears as a shoulder around 265 nm. However, no optical activity was observed in the first place. Long term measurements (red squares) revealed that the CD value is slighty negative around 265 nm, which fits to the ligands optical activity (Figure 4.18). It appears that the SiNCs do interfere with the measurement of the CD value, which is probably due to light scattering by the particles.

Unfortunately, SHG-CD could not be applied to these samples due to the very low yield of second harmonic signal, as previously shown in Figure 4.16. The attempts to properly functionalize larger SiNCs with the synthesized chiral molecules were not succesful due to

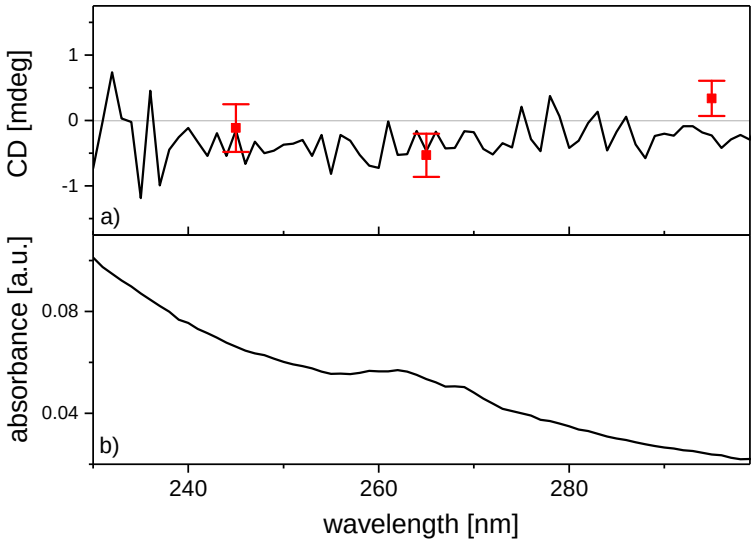

Figure 4.19: (a) CD spectrum and b) absorbance for 3 nm SiNCs coated with (R)-(1-(allyloxy)ehtyl)benzene. The absorption of the ligand (255 - 275 nm) is visible on top of the featureless absorbance of the SiNCs. The red squares display long term CD measurements at selected wavelengths and a small negative CD value was measured around 265 nm.

solubility issues. The prepared chiral ligand is more polar than for example dodecane and the 9 nm SiNCs are already not well soluble when using dodecane. The attachement of the chiral ligand was therefore leading to a precipitation of the SiNCs during the early stage of the functionalization procedure. A more polar solvent has the inherent problem, that the hydrogen-terminated particles are not properly soluble. Despite these problems, the 9 nm SiNCs (see Figure 4.16) seem very promising for the investigation of chiral semiconductor nanomaterials, as they are very uniform and yield a high second harmonic intensity, which makes the use of SHG-CD applicable.

5 Conclusion and Outlook

Through the course of this dissertation several projects and goals were pursued. First, the phenomenom of chirality transfer was investigated. Therefore, the interaction between chiral thiol-containing biomolecules and silver or gold was studied. In the second project, the optical properties of organically capped SiNCs have been investigated, with focus on their PL properties. Finally, the insight from both projects was combined to create and investigate chiral semiconductor nanomaterials. Therefore, SHG spectroscopy and its extension SHG-CD were applied, as conventional CD spectroscopy reaches its limits for the chiroptical study of semiconductor nanomaterials.

A reproducible method to fabricate water-soluble ligand protected chiral silver particles was established, with chiral thiols playing a dual role. They act both as protecting and chirality transfer agents, as well as reducing agents. The direct reduction and capping approach leads to structures with a large optical activity and it is performed as a one-step reaction. Consequently, this approach is superior to the usual procedure, which is the synthesis of small spherical nanoparticles with a subsequent ligand exchange reaction. Despite their irregular structure, the particles created from L- and D-cysteine showed a mirror-imaged g-value. A subsequent time-resolved study of the particle growth and related optical activity gave further insight into the underlying chirality transfer mechanism. While the structure of the material had significant impact on the magnitude of the measured g-value, it is not the origin of the mirror image like behavior of the g-value. This leads to the conclusion, that the optical activity was induced by a mixture of chiral polarisation of the surrounding electric field and a chiral footprint. The same method was then applied in order to generate chiral gold nanomaterials. However, a further reducing agent is necessary to produce elemental gold nanomaterials in most cases. The simultaneous addition of L-cysteine and sodium borohydride lead to a remarkable g-value of 1 % in one case. It appears that the reactant ratio influences the outcome drastically and does not behave linearly. This means more cystein added does not always lead to a larger observed chirality. However, the amount of reducing agent has an optimal value and is decreasing the optical activity for higher amounts. In conclusion, the reactant ratio plays an important role, which was also observed in case of silver, where a ratio of 0.2:1 (cysteine:silver) yielded the best results.
Within the next project, the PL of organically capped SiNCs was examined. First, the existing and most commonly applied decay models used for SiNC luminescence were described

theoretically. Then two dodecene-functionalized SiNC samples with mean diameters of 2.9 and 5.4 nm were prepared and investigated in order to compare the different decay models. Their PL spectrum and decays were measured using standard methods and the PL decays were fit with several models in order to find the best fitting model. While the simple stretched exponential function fits the time-resolved data reasonably well, the distribution of residuals shows that it is not strictly accurate. In reality, none of the applied fitting models fully captures the luminescence decay and they all yield different average time constants. Moreover, the responsivity curve of the detector influences the determined time constants. With that, the interpretation and comparability of PL decays becomes problematic for SiNC ensembles. However, TRS yields internally meaningful data, as long as the same fit model and detector are used. QFRS was then carried out in order to determine the lifetime distribution of the SiNC ensembles directly. We find that FRS techniques are suited for the study of SiNC luminescence dynamics and could replace TRS and the associated choice of the 'best' fit model. However, FRS does come with a disadvantage, which is the required deconvolution. Also the detector responsivity influences the obtained FRS results, altough it can be corrected in principle.

The simple stretched exponential was then used to fit the time-resolved data, as it was found to be the best fitting model and is widely applied in the literature. The temperature-dependent PL of alkyl-capped SiNC solids with mean diameters from 3 to 9 nm has been investigated between 41 and 300 K. SiNCs with an average diameter of 6 nm or more, showed an increasing redshift with decreasing temperature. This was observed for the first time, as previous studies focused on smaller SiNCs.[97,173,174] So far, a blueshift was observed when decreasing the temperature, which was attributed to the phenomenom of bandgap widening.[173] However, the observed redshift of the PL is contrary to bandgap widening and thus surprising. Detailed spectral and time-resolved analysis of the PL of five differently sized SiNC ensembles revealed that not only the overall decay time was shorter for smaller sized SiNC ensembles, but also the individual decay time of smaller sized fractions within an ensemble. This means that the observed effects originate mainly from the particle size distribution of the samples. Furthermore, evidence for occuring energy transfer was found. The combination of bandgap windening (blueshift) , size-dependent PL enhancement (blueshift), and a size-dependent flourescence energy transfer (redshift) can explain the observed steady transition from a low-temperature blueshift to a low-temperature redshift with increasing mean particle diameters.

In the last part of the thesis, the so far gained insight was used to prepare and investigate chiral semiconductor nanomaterials. The analysis of semiconductors' optical activity is not always possible with commercial CD spectrometers, as these are usually not equipped with an integrating sphere and are thus not sensitive enough. SHG-CD is very sensitive and a measurement in reflection mode can be realized, which additionally removes the limitation

of transparent samples. SHG/SHG-CD was successfully applied on the recently discovered inorganic double helical material SnIP and to differently sized SiNCs, which are all semiconducting.

The PL in silicon nanomaterials is complicated, but the gained knowledge may help to increase reproducibility and the understanding of the present literature. The awareness of the found ensemble effects can help to improve present quantum dot based applications or may be used to create new devices, which for example exhibit a temperature-independent light emission.
The gained knowledge about chiral noble metal nanomaterials can be useful for the creation of chiral photonic devices and sensor components.[116,175,176]. Furthermore, no hazardous substances were used for the direct synthesis approach. It thus displays an option for a green synthesis of chiral silver and gold nanomaterials, which in turn may be suitable for medical and pharmaceutical applications.[177,178].
The field of chiral semiconductor nanomaterials is rather new and gains more attention in recent years. The so far known examples show a chiral structure[179–181] or exhibit a chiral footprint[19,182]. Chiral semiconductors exhibit useful electronic and optical properties and can be used for different applications.[114] For instance, inorganic helical nanosprings and semiconductor nanosprings, which can be used as nano-scale sensors, for hydrogen storage or as efficient photosensors.[183–185] Thus, chiral semiconductors remain of particular interest in the future.

6 Reprinted Publications

6.1 Chirality transfer from organic ligands to silver nanostructures via chiral polarisation of the electric field

Matthias Jakob, Alexander von Weber, Aras Kartouzian* and Ulrich Heiz

Chair of Physical Chemistry, Technical University of Munich, Lichtenbergstrasse 4, 85748 Garching, Germany.

* corresponding author, Email: aras.kartouzian@tum.de

Reproduced from *Phys.Chem.Chem.Phys.*, **2018**, *20*, 20347 with permission from the PCCP Owner Societies.

Volume 20 | Number 31 | 21 August 2018 | Pages 20299–20736

PCCP

Physical Chemistry Chemical Physics

rsc.li/pccp

ISSN 1463-9076

ROYAL SOCIETY OF CHEMISTRY

PAPER

Aras Kartouzian *et al.*

Chirality transfer from organic ligands to silver nanostructures *via* chiral polarisation of the electric field

PCCP

PAPER

View Article Online
View Journal | View Issue

Cite this: *Phys. Chem. Chem. Phys.*, 2018, **20**, 20347

Chirality transfer from organic ligands to silver nanostructures *via* chiral polarisation of the electric field†

Matthias Jakob, Alexander von Weber, Aras Kartouzian* and Ulrich Heiz

Received 10th May 2018,
Accepted 27th June 2018

DOI: 10.1039/c8cp02970a

rsc.li/pccp

Water-soluble ligand protected optically active silver nanostructures were synthesised in a one-step reduction and capping process mediated by thiol-containing biomolecules. The synthesis was performed successfully with D- and L-cysteine and L-glutathione. The chiroptical properties of the obtained nanostructures were investigated by circular dichroism spectroscopy in the ultraviolet and visible wavelength range. They exhibit a *g*-value of up to 0.7%, which is about one order of magnitude larger compared to particles prepared by citrate reduction followed by a ligand exchange reaction. The structure and composition of the prepared materials were characterised by transmission electron microscopy, energy-dispersive X-ray and X-ray photoelectron spectroscopy. Although these structures do not have a chiral geometry, they show mirror image *g*-values when capped with D- and L-cysteine. This indicates that the underlying chirality transfer mechanism is based on an electric field polarisation process.

Introduction

Chirality is a fundamental property for life on earth, and it also plays a crucial role in asymmetric catalysis *e.g.* for the synthesis of pharmaceutical drugs.[1,2] In biomedical applications, to avoid unwanted residues and extensive cleaning procedures, it is preferable that only water-soluble and non-toxic materials are used during the synthesis.[3] For this purpose, heterogeneous asymmetric catalysis presents important advantages over homogeneous catalysis, such as easier catalyst recovery and lower probability of product contamination by the catalyst.[4] There are two main approaches to obtain efficient heterogeneous asymmetric catalysts. The first one is the immobilisation of homogeneous asymmetric catalysts. The alternative is the asymmetrisation of heterogeneous catalysts, where chirality must be transferred into the catalyst to favour the formation of one of the product's enantiomers.[5,6] Thus, it is crucial to investigate how to introduce chirality in an intrinsically achiral material. Noble metals, such as gold and silver, are ideal to investigate the mechanism of chirality transfer because their surface plasmon resonances ease the analysis of the optical and chiroptical properties.[7,8] Furthermore, the high sensitivity of the optical properties of noble metals to their surrounding environment[9,10] makes them attractive for chirality-related sensing applications, which demand is constantly increasing.[11,12] In the last decade, several methods to produce chiral noble metal structures and materials with a wide variety of sizes and shapes have been reported;[13–15] for example, nanosized intrinsically chiral cross-like structures, nanohelices, and clusters.[16,17] Alternatively, chirality can be transferred into intrinsically achiral structures by attaching chiral ligands to them.[18–20]

Three possible mechanisms for chirality transfer are commonly proposed: (i) formation of a chiral metal core due to the influence of chiral ligand molecules on the formation of the cluster (chiral growth), (ii) electronic interaction between the chiral ligands and achiral metal core electrons (chiral polarisation) and (iii) a chiral arrangement of the ligands on an achiral metal core (chiral footprint).[20–25] Silver and chiral thiols are particularly good candidates to investigate chirality transfer. Silver nitrate can be reduced by thiols[26] and water-soluble capped silver particles can be obtained if a thiol-containing amino acid is used as a reducing agent.[26,27] Moreover, chirality was already successfully transferred to similar systems in the past, which consisted of gold nanoparticles and chiral thiols as capping ligands.[18,22,28] Goldsmith *et al.* showed that the core of a ligand-capped gold cluster does not need to be chiral to exhibit a significant optical activity; however, a chiral adsorption pattern in combination with a chiral field, generated by the surrounding chiral molecules, can have a strong effect on the particle's electronic states.[29] The surface structure of a material can also have a great influence on its optical properties. In this respect, D'Acunto *et al.* reported that a rippled nanoscale surface leads to a near-field plasmon enhancement, especially close to the nanogaps.[30] And recently, Wang *et al.* demonstrated that circular dichroism can be influenced greatly by the 'super chiral hot spots', which are apexes within a chiral metamaterial.[31]

Chair of Physical Chemistry, Technical University of Munich, Lichtenbergstrasse 4, 85748 Garching, Germany. E-mail: aras.kartouzian@tum.de

† Electronic supplementary information (ESI) available. See DOI: 10.1039/c8cp02970a

View Article Online

Paper PCCP

In this work, we present water-soluble optically active silver nanostructures, which were prepared by reducing silver nitrate with chiral thiol-containing biomolecules in a one-step reaction. These biomolecules act as capping and chirality transfer agents as well and thus display an efficient way to transfer chirality into silver nanomaterials. Additionally, information about the underlying chirality transfer mechanism could be gained by the chiroptical and structural analysis of the obtained materials.

Experimental

Materials

Silver nitrate (99.9999%), sodium citrate tribasic dehydrate (≥99.5%), tannic acid (≥97%), L-cysteine (≥97%), D-cysteine (≥99%) and L-glutathione (≥98%) were obtained from Sigma-Aldrich and used without further purification. Ultrapure water (UPW) was obtained from a Direct-Q® 5 UV purification system from Merck Millipore.

Synthesis and characterisation

Two different methods were used to prepare the samples. The first method used a thiol-containing amino acid as a reducing agent and a capping ligand. The second method, which functions as a reference for sample composition, involved starting with a modified citrate reduction followed by a ligand exchange reaction, leading to small capped silver nanoparticles.

Method 1: Direct reduction and capping by a thiol-containing biomolecule. First, 60 μmol of $AgNO_3$ dissolved in 5 mL of ultrapure water (UPW) were placed in a flask and stirred at 500 rpm. Then, 12 μmol of the respective ligand (L-glutathione and L/D-cysteine) dissolved in 5 mL UPW were added. The L/D-cysteine batches were stirred at room temperature overnight (20 h), yielding a clear yellow solution for both enantiomers. Centrifugation led to the agglomeration or destruction of most particles; thus, it was not performed as a purification step. In addition, prolonged reaction times resulted in a brown precipitate. For the time resolved study, the reaction temperature was set to 35 °C to ensure stable reaction conditions.

The L-glutathione batch did not react at room temperature; hence, it was set under reflux for 5.5 h at 115 °C in an oil bath. The resultant yellow gel was centrifuged (15 000 rpm, 10 °C, 10 min) and re-dispersed in UPW by sonication three times. The solutions were stored at 8 °C until use. A 0.2 : 1 ligand to $AgNO_3$ ratio was chosen because it has been reported to yield stable particle dispersions.[27] D-Glutathione was not available, so it was not possible to compare the two enantiomers.

Method 2: Reduction with citrate and tannic acid and subsequent ligand exchange reaction. In a round bottom flask, 100 μmol $AgNO_3$ were dissolved in 100 mL UPW and heated to reflux. Then, 350 μmol sodium citrate and 15 μmol tannic acid, each dissolved in 5 mL UPW, were mixed and immediately added to the boiling $AgNO_3$ solution. The solution was refluxed for 5 min and, then, cooled to room temperature using an ice bath. The resulting dark-yellow solution was stored at 8 °C until use. The ligand exchange reaction was performed by adding 325 μmol of L-glutathione to 10 mL of the prepared silver nanoparticles solution and stirring overnight. A red precipitate was obtained; then, it was centrifuged (15 000 rpm, 10 °C, 10 min) and re-dispersed in UPW three times. The dispersion was stored at 8 °C until use.

TEM images were acquired using a JEM-1400 microscope from JEOL and evaluated with ImageJ. SEM and EDX data were obtained with a JSM-7500F from JEOL equipped with an XMax detector from Oxford Instruments. CD and UV/VIS spectra were recorded on a J-815 spectrophotometer from Jasco. XPS spectra were recorded on a SPECS system equipped with a Phoibos 150 2D CCD hemispherical analyser and a Focus 500 monochromator. The detector angle was set perpendicular to the surface and the X-ray source was Al Kα.

Results and discussion

Table 1 shows the XPS results. It can be seen that, consistent with the literature,[32] the Ag 3d peak is around 368.3 eV. Additionally, nitrogen 1s and sulphur 2p and 2s were measured. For all the centrifuged samples no nitrate seems to be present (peak expected around 407 eV); only the nitrogen peak for amines at 400 eV is observed. This indicates that the particles are composed of elemental silver. To evaluate the reaction between $AgNO_3$ and cysteine, SEM/EDX analysis was performed on a centrifuged part of the sample; a single intact particle is sufficient for this technique (Fig. S9, ESI†). The nitrogen content is below the detection limit in the D-cysteine capped particles, further demonstrating that all the prepared materials consist of elemental silver. The XPS analysis of sulphur 2p reveals that the ligands are covalently bound to the metal, as a peak at 162.3 eV was observed and no indication of silver sulphide (161 eV) or unbound ligands (164 eV) is present.[33–35] The fitted XPS spectra are depicted in the ESI† (Fig. S4–S7).

Optical and structural characterisation of chiral Ag nanostructures

CD spectra of all the compounds were recorded to investigate the chiroptical properties of the obtained materials. The

Table 1 XPS binding energies (eV) of Ag 3d, N 1s, S 2p and S 2s for the investigated samples. The spectra were referenced to the carbon 1s peak at 284.8 eV. Spin orbit couples are not shown

Sample	Ag 3d	N 1s	S 2p	S 2s
Citrate stabilized nanoparticles (Method 2)	368.2	407.5	—	—
L-Glutathione capped nanoparticles (Method 2)	368.3	400.0	162.3	226.6
L-Glutathione capped particles (Method 1)	368.3	400.2	162.3	226.8
L-Cysteine capped particles (Method 1)	368.6	399.8/407.3	162.3	226.3
D-Cysteine capped particles (Method 1)	368.3	399.9/407	162.3	226.5

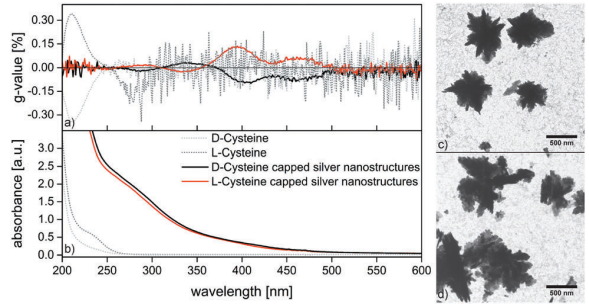

Fig. 1 (a) *g*-Value and (b) absorbance against wavelength for D- and L-cysteine (dotted line) and the functionalised silver particles (black: D-cysteine/red: L-cysteine). TEM images of the resulting structures using (c) L-cysteine and (d) D-cysteine. The reaction was carried out at RT.

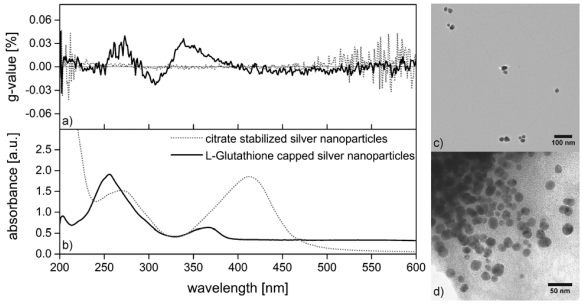

Fig. 3 (a) *g*-Value and (b) absorbance of citrate-stabilised silver nanoparticles (dotted line) and silver nanoparticles capped with L-glutathione (black line). TEM images of (c) citrate-stabilised silver nanoparticles and (d) L-glutathione capped silver nanoparticles.

spectra and TEM images for samples prepared *via* Method 1 are depicted in Fig. 1. The spectra of the pure ligands are shown as dotted lines; there is no optical activity above 300 nm. As seen in the TEM images, silver particles with sizes between 600 and 800 nm were formed. The L- and D-cysteine capped silver particles show the same absorbance behaviour and a well-defined mirror-imaged *g*-value between 275 and 500 nm. Since the ligands do not have any optical activity above 300 nm, the observed optical activity can be confidently assigned to the silver nanostructures. To obtain high quality spectra in the region between 275 and 500 nm a high sample concentration was used, which prevented the correct measurement of the *g*-value below 250 nm. When using Method 1 it is also possible to generate chiral silver particles using L-glutathione as a reducing and capping agent (Fig. 2). The prepared particles have a size of around 500 nm and exhibit a snowflake-like structure. These structures have a *g*-value of up to 0.7% and are optically active over the entire wavelength range evaluated. Again, the optical activity observed above 300 nm can be confidently assigned to transitions in silver because L-glutathione does not present any optical response in this range. Below 250 nm the optical activity is similar to the pure ligand. One can expect that behaviour for the D/L-cysteine capped particles as well (Fig. 1).

As a reference, small silver nanoparticles were synthesised according to Method 2 and capped with L-glutathione. The *g*-values

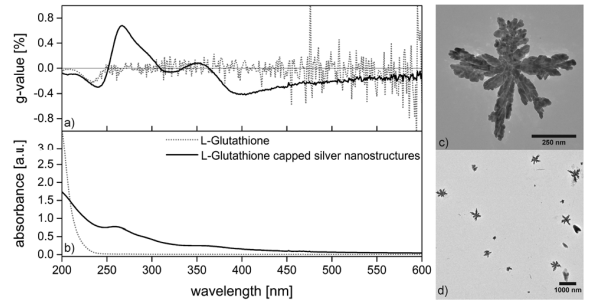

Fig. 2 (a) *g*-Value and (b) absorbance against wavelength for L-glutathione (dotted line) and silver nanostructures obtained using L-glutathione as a reducing agent (black line). (c and d) TEM images of L-glutathione capped silver nanostructures.

of citrate-stabilised silver nanoparticles (dotted line) and L-glutathione capped silver nanoparticles are depicted in Fig. 3a. Their size is around 25 nm in diameter, as determined from the TEM images (Fig. 3c/d). The citrate-stabilised particles exhibit pronounced absorption peaks around 412 and 270 nm, which can be respectively attributed to the surface plasmon resonance and the interband transitions of silver; however, no optical activity is observed in the measured wavelength range. The strong absorbance below 250 nm originates from the tannic acid and citrate. After the ligand exchange reaction with L-glutathione (black line) the main part of the surface plasmon resonance vanishes and only a small part remains around 370 nm. However, the small remaining peak as well as the interband transitions exhibit a measurable optical activity. Compared to the large silver structures obtained with L-glutathione *via* Method 1, the small L-glutathione-capped nanoparticles prepared by Method 2 exhibit a similar trend in their optical activity, although smaller in magnitude. Both samples show a positive *g*-value around 270 and 350 nm, but a negative one in between. Above 400 nm, they both show a negative *g*-value that slowly decreases towards higher wavelengths.

In order to investigate the findings further, a time resolved study of the reaction between $AgNO_3$ and L/D-cysteine was performed (Fig. S1–S3, ESI†). The TEM images corresponding to 2, 12 and 30 h reaction time at 35 °C are shown in Fig. 4. It can be seen that for the 2 h sample, almost only very small particles are present, which probably accumulated in droplets during the preparation process for TEM. There are three remarkable changes over time: first, huge particles form and steadily grow (Fig. 4 bottom 12/30 h); second, small nanoparticles appear after 12 h (Fig. 4 top 12/30 h) and third, the very small particles (Fig. 4 top 2 h) slowly disappear over time. These very small particles exhibit some optical activity between 300 and 425 nm, as well as around 460 nm (Fig. 5a). Therefore, it can be assumed that the very small particles (chiral building blocks) are present in all samples up to 24 h; thus, the *g*-value at 2 h was subtracted from all spectra except for the 30 h sample. For D-cysteine, where all the small building blocks disappeared after 30 h (Fig. 6d), this correction fits almost perfectly, as can be seen in Fig. 6b; this illustrates the accuracy of the assumption.

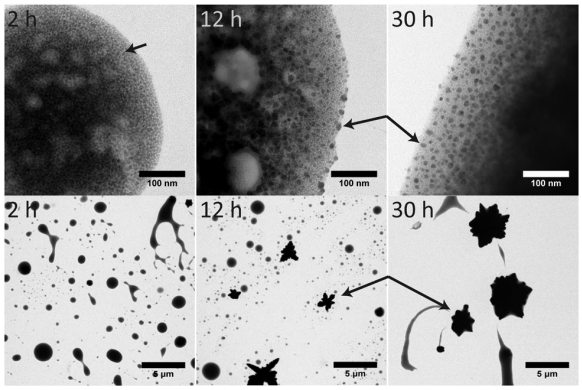

Fig. 4 TEM images after 2, 12 and 30 h of reaction for L-cysteine. Formation of very small (single arrow), small and huge particles (arrow pairs) can be observed over time. The upper row represents an amplification of the gel like formations of the samples.

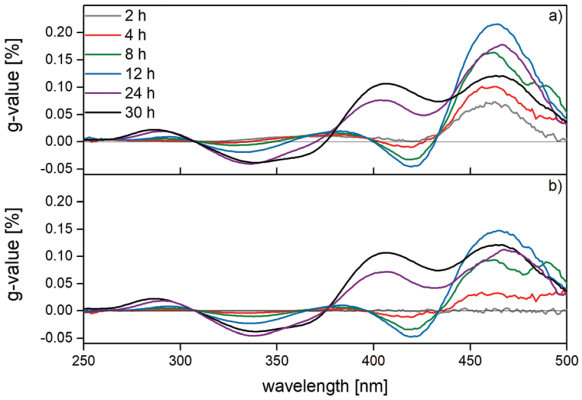

Fig. 5 (a) Time resolved smoothed *g*-values of L-cysteine capped particles produced by Method 1. (b) Corrected time resolved smoothed *g*-values. The *g*-value after 2 h of reaction was subtracted from all the spectra except 30 h, where almost no small chiral building blocks remain. The resulting spectra reflect the growth-dependent *g*-value.

Comparing the final *g*-value (30 h) in Fig. 5 to the *g*-value in Fig. 1, the trend and magnitude are very similar; however, no small nanoparticles are present in the sample of Fig. 1. Hence, the observed effect can be confidently assigned to the growth of the large silver particles and not to the formation of small nanoparticles.

To sum up, small chiral building blocks (Fig. 4, 2 h) are formed within 2 h; then, they grow into larger particles (Fig. 4, 12 h). With increasing particles size, the *g*-value also increases (Fig. 5b), but seems to saturate at a certain size, since the particles prepared without heating have a maximum size of 1 micron; however, the particles grown at 35 °C have sizes up to 5 microns. Consequently, not only the size but also the related properties such as density, structure or ligand coverage may have an effect.

All these observations provide information about the underlying chirality transfer mechanism. Initially, it may be assumed

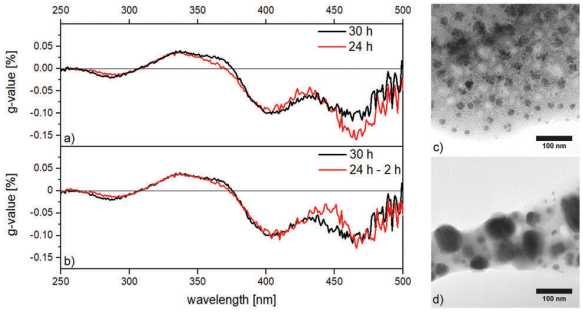

Fig. 6 (a) *g*-Value of the sample reduced with D-cysteine after 24 and 30 h reaction time. (b) Corrected *g*-value of the sample reduced with D-cysteine after 24 h and uncorrected *g*-value after 30 h. TEM images of particles within gel like formations after (c) 24 h and (d) 30 h.

that the chiral building blocks are intrinsically chiral or are attaching to each other in a chiral way, thus, forming structural enantiomers. However, since the growth process is not controlled in this respect, this is statistically very unlikely. And when comparing the generated structures using L/D-cysteine (Fig. 1c/d) it indeed appears that they possess a random shape and are not structural enantiomers, despite the mirror image *g*-value. Thus, the observed *g*-values originate from either chiral polarisation of the plasmon resonance or a chiral footprint on the particles surface, or a combination of them. As proposed by Goldsmith *et al.*, we assume both mechanisms influence the observed optical activity.[29] The fact that the *g*-value increases, while particles grow larger and that the snow-flake like L-glutathione capped silver particles show a larger *g*-value than the small capped nanoparticles is discussed in the following. As seen in Fig. 7, there are many nanogaps and apexes in the formed structures that may lead to local field enhancement or 'super chiral hot spots', which in turn enhance the measured *g*-value.[30,31] So, it is very likely that the dendritic structure of the obtained materials leads to the enhancement of the *g*-value. It is possible that there is an optimal size for the nanogaps and apexes, which might explain that the *g*-value is saturating with further growth. However, this observation cannot be satisfactory resolved within this study.

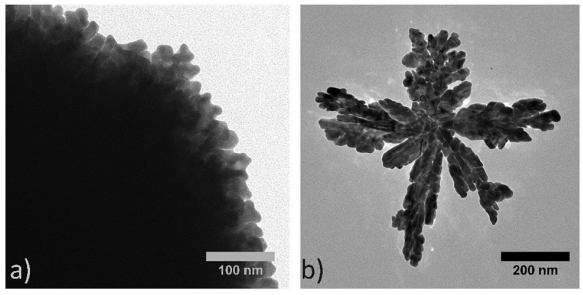

Fig. 7 (a) Structure of a large particle formed by the reaction between D-cysteine and $AgNO_3$ at 35 °C. (b) Structure of a particle formed by the between L-glutathione and $AgNO_3$ at 130 °C. A branch like growth with nanogaps is observed in both cases.

We conclude that the observed effects are due mainly to the chiral footprint on the particle surface in combination with chiral polarisation of the electronic transitions and plasmon resonance of silver, enhanced further by the formed geometric structures.

Conclusions

We present a reproducible method to fabricate water-soluble ligand-protected chiral silver particles. Chiral thiols play a dual role in this process: they act both as protecting ligands and chirality transfer agents, and as reducing agents. This not only eliminates the need for a ligand exchange reaction, but also leads to structures that possess a larger optical activity in the visible wavelength range, compared to small functionalised nanoparticles. The TEM images of the silver nanostructures obtained with two enantiomers show that they do not possess any structural chirality. But a mirror-imaged *g*-value was found. Nevertheless, the structure of the material can have a great impact on the magnitude of the *g*-value. The observed optical activity was found to be induced by a mixture of a chiral adsorption pattern and chiral polarisation of the electric field, caused by the attached ligands. Thus, chirality may be very efficiently transferred into metal particles through the mentioned mechanisms. These findings may be useful for the design of chiral photonics and sensors components.[36,37] The approach presented in this work also provides a suitable method for green synthesis of chiral silver nanoparticles, which may be used for pharmaceutical or medical purposes *e.g.* to prepare antibacterial agents or for tracing applications.[3,38]

Conflicts of interest

There are no conflicts to declare.

Acknowledgements

This work was financially supported by the DFG through the projects Alberta/Technische Universität München Graduate School for Functional Hybrid Materials ATUMS (IRTG2022) and HE 3454/21-1.

Notes and references

1 F. Rolf, *J. Chem. Inf. Model.*, 2013, **53**, 1689–1699.
2 J. M. Hawkins and T. J. N. Watson, *Angew. Chem., Int. Ed.*, 2004, **43**, 3224–3228.
3 Q. Wu, H. Cao, Q. Luan, J. Zhang, Z. Wang, J. H. Warner and A. A. Watt, *Inorg. Chem.*, 2008, **47**, 5882–5888.
4 A. Corma and H. Garcia, *Top. Catal.*, 2008, **48**, 8–31.
5 I. Schrader, S. Neumann, A. Šulce, F. Schmidt, V. Azov and S. Kunz, *ACS Catal.*, 2017, **7**, 3979–3987.
6 M. Heitbaum, F. Glorius and I. Escher, *Angew. Chem., Int. Ed.*, 2006, **45**, 4732–4762.
7 J. M. Slocik, A. O. Govorov and R. R. Naik, *Nano Lett.*, 2011, **11**, 701–705.
8 T. Lünskens, P. Heister, M. Thämer, C. A. Walenta, A. Kartouzian and U. Heiz, *Phys. Chem. Chem. Phys.*, 2015, **17**, 17541–17544.
9 T. Lünskens, A. Von Weber, M. Jakob, T. Lelaidier, A. Kartouzian and U. Heiz, *J. Phys. Chem. C*, 2017, **121**, 9331–9336.
10 T. Lünskens, C. A. Walenta, P. Heister, A. Kartouzian and U. Heiz, *J. Cluster Sci.*, 2017, **28**, 3185–3192.
11 M. Schäferling, M. Hentschel, D. Dregely, X. Yin and H. Giessen, *AIP Conf. Proc.*, 2012, **1475**, 77–79.
12 Y. Kubo, S. Maeda, S. Tokita and M. Kubo, *Nature*, 1996, **382**, 522–524.
13 M. Schäferling, D. Dregely, M. Hentschel and H. Giessen, *Phys. Rev. X*, 2012, **2**, 1–9.
14 J. Kumar, K. G. Thomas and L. M. Liz-Marzán, *Chem. Commun.*, 2016, **52**, 12555–12569.
15 M. Liu, L. Zhang and T. Wang, *Chem. Rev.*, 2015, **115**, 7304–7397.
16 J. T. Collins, C. Kuppe, D. C. Hooper, C. Sibilia, M. Centini and V. K. Valev, *Adv. Opt. Mater.*, 2017, **5**, 1700182.
17 S. Knoppe and T. Bürgi, *Chim. Int. J. Chem.*, 2013, **67**, 236–239.
18 C. Gautier, R. Taras, S. Gladiali and T. Bürgi, *Chirality*, 2008, **20**, 486–493.
19 Y. Li and M. Liu, *Chem. Commun.*, 2008, 5571–5573.
20 G. Shemer, O. Krichevski, G. Markovich, T. Molotsky, I. Lubitz and A. B. Kotlyar, *J. Am. Chem. Soc.*, 2006, **128**, 11006–11007.
21 T. G. Schaaff and R. L. Whetten, *J. Phys. Chem. B*, 2000, **104**, 2630–2641.
22 C. Gautier and T. Bürgi, *ChemPhysChem*, 2009, **10**, 483–492.
23 Z. Fan and A. O. Govorov, *Nano Lett.*, 2010, **10**, 2580–2587.
24 A. O. Govorov, *J. Phys. Chem. C*, 2011, **115**, 7914–7923.
25 A. O. Govorov, Z. Fan, P. Hernandez, J. M. Slocik and R. R. Naik, *Nano Lett.*, 2010, **10**, 1374–1382.
26 R. Cecil, *Biochem. J.*, 1950, **47**, 572–584.
27 M. Roy, P. Mukherjee, B. P. Mandal, R. K. Sharma, A. K. Tyagi and S. P. Kale, *RSC Adv.*, 2012, **2**, 6496.
28 M. Bieri and T. Bürgi, *Langmuir*, 2005, **21**, 1354–1363.
29 M.-R. Goldsmith, C. B. George, G. Zuber, R. Naaman, D. H. Waldeck, P. Wipf and D. N. Beratan, *Phys. Chem. Chem. Phys.*, 2006, **8**, 63–67.
30 M. D'Acunto, F. Fuso, R. Micheletto, M. Naruse, F. Tantussi and M. Allegrini, *Beilstein J. Nanotechnol.*, 2017, **8**, 956–967.
31 Z. Wang, B. H. Teh, Y. Wang, G. Adamo, J. Teng and H. Sun, *Appl. Phys. Lett.*, 2017, 110, DOI: 10.1063/1.4984920.
32 J. F. Moulder, W. F. Stickle, P. E. Sobol and K. D. Bomben, *Handbook of X-Ray Photoelectron Spectroscopy*, Perkin-Elmer Corporation, 1992.
33 M. Himmelhaus, I. Gauss, M. Buck, F. Eisert, C. Wöll and M. Grunze, *J. Electron Spectrosc. Relat. Phenom.*, 1998, **92**, 139–149.
34 V. Krylova and N. Dukštienė, *J. Chem.*, 2013, **2013**, 1–11.
35 D. G. Castner, K. Hinds and D. W. Grainger, *Langmuir*, 1996, **12**, 5083–5086.
36 W. L. Barnes, A. Dereux and T. W. Ebbesen, *Nature*, 2003, **424**, 824–830.
37 N. L. Rosi and C. A. Mirkin, *Chem. Rev.*, 2005, **105**, 1547–1562.
38 X. Wang, M. Wang, R. Lei, S. F. Zhu, Y. Zhao and C. Chen, *ACS Nano*, 2017, **11**, 4606–4616.

Supporting information

Chirality transfer from organic ligands to silver nanostructures via chiral polarization of the electric field

Time resolved analysis of L/D-Cysteine g value and particle growth

The optical acitivity was measured after different reaction times. TEM images were taken accordingly. No TEM image was taken after 6h, as there was not much change in the optical activity. The g-value data have been smoothed by the means of a 10 point savitzgy-golay filter.
TEM images were acquired using a JEM-1400 microscope from JEOL and evaluated with ImageJ. CD and UV/VIS spectra were recorded on a J-815 spectrophotometer from Jasco.

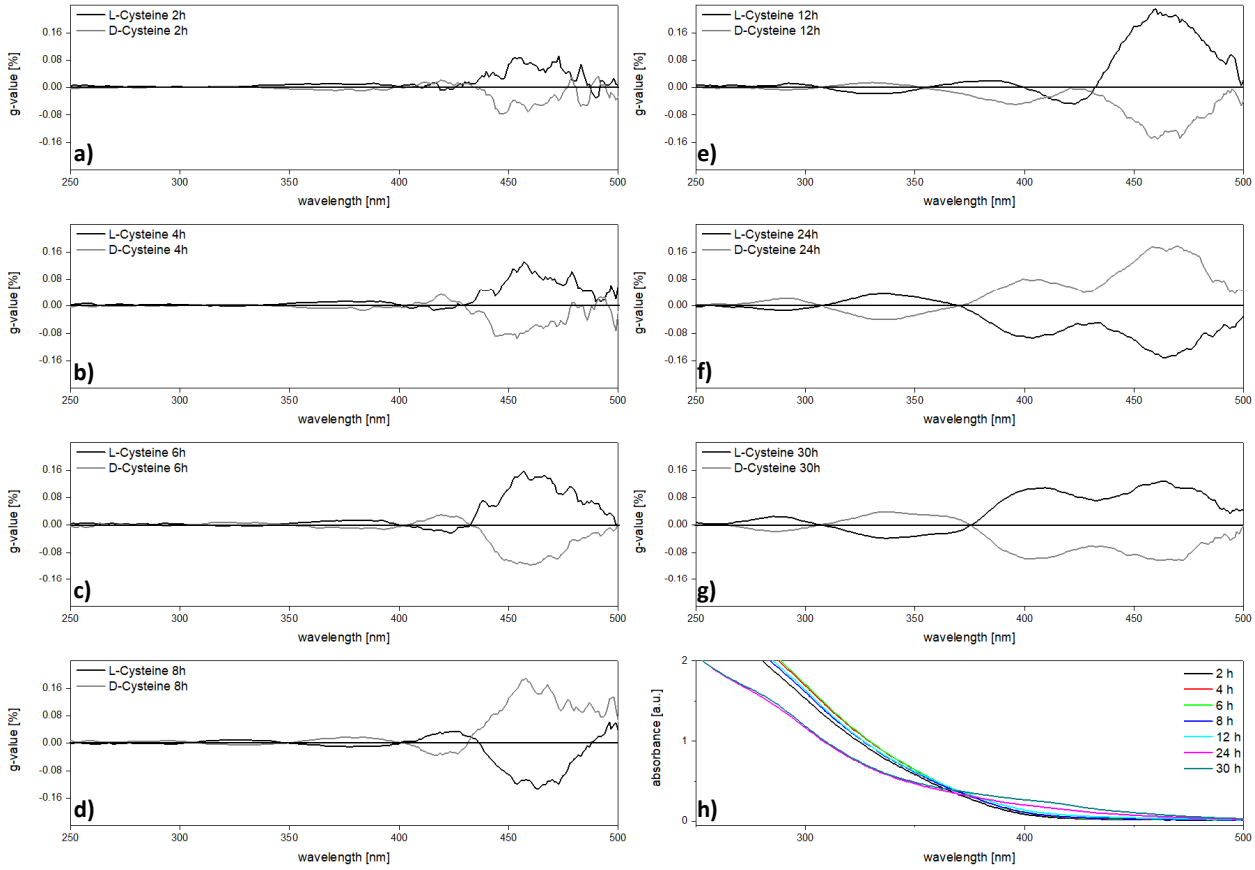

Fig. SI 1: a-f) g values for different reaction times of D/L-Cysteine and $AgNO_3$ are shown. The samples were measured without further purification. **h)** According absorption spectra are depicted for the reaction with D-Cysteine. L-Cysteine samples are showing the same absorption.

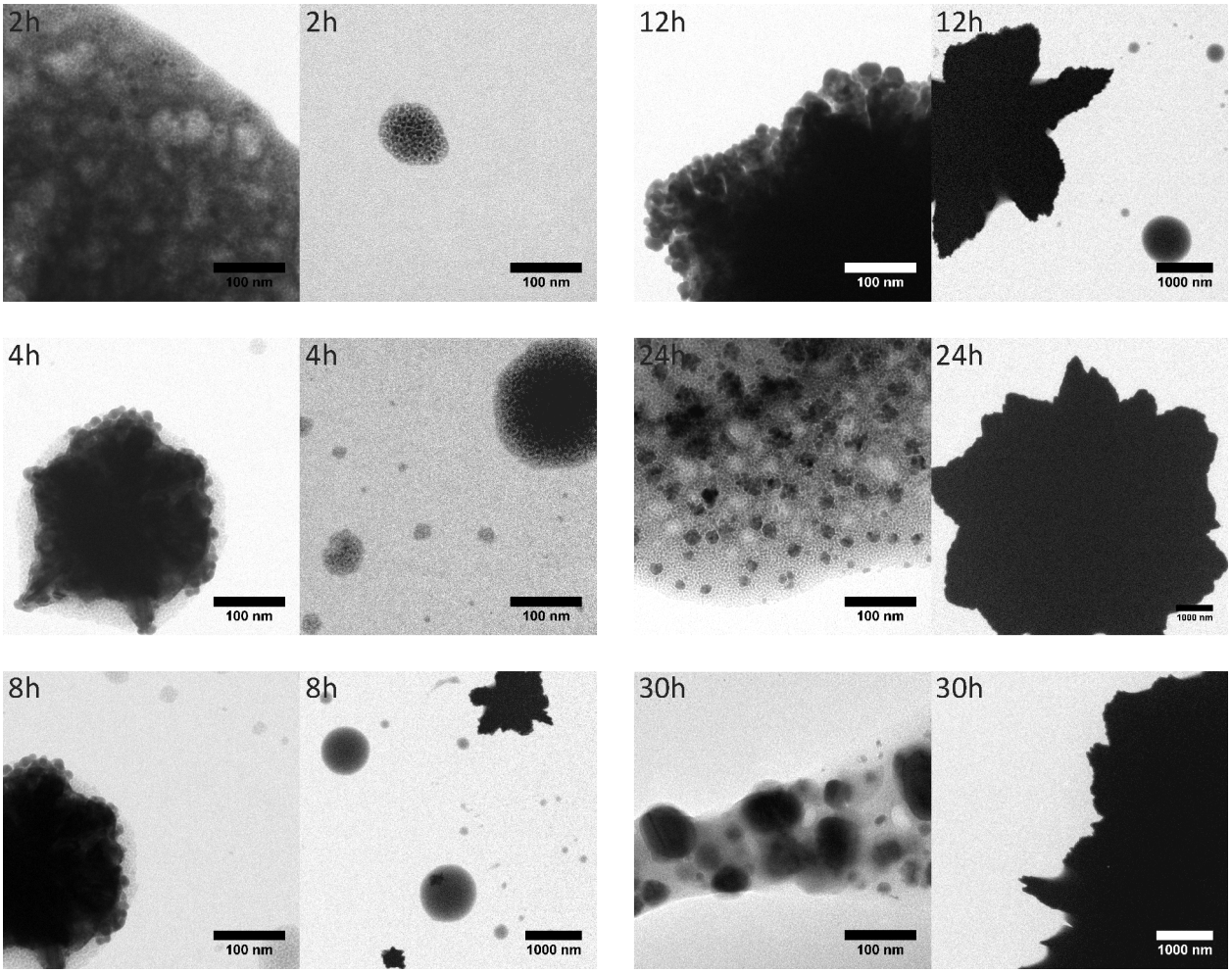

Fig. SI 2: TEM images of the reaction between **D-Cysteine** and $AgNO_3$ at 35°C. A part of the sample has been taken out from the reaction and was drop casted on a TEM grid immediately. Afterwards CD spectra were taken.

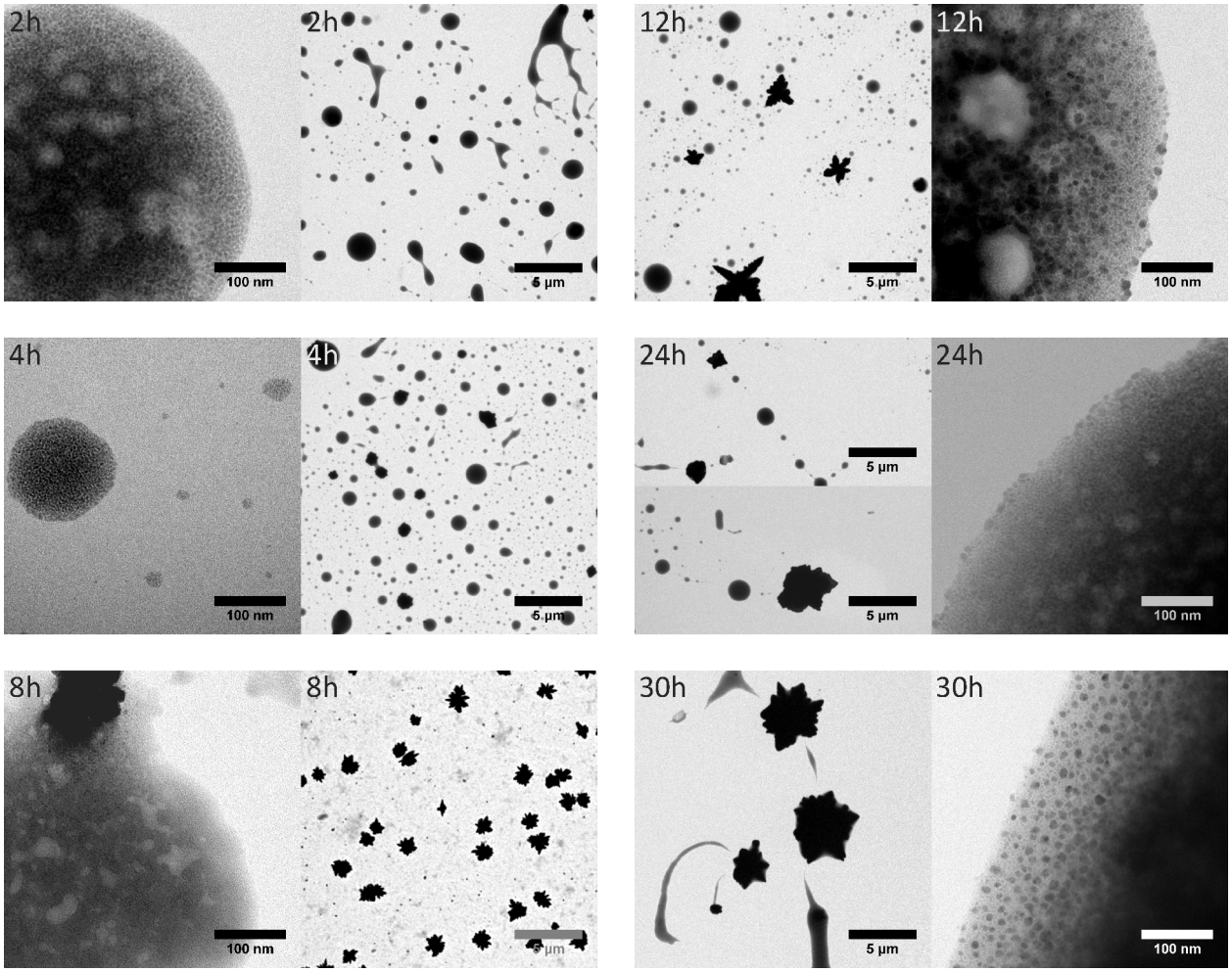

Fig. SI 3: TEM images of the reaction between **L-Cysteine** and $AgNO_3$ at 35°C. A part of the sample has been taken out from the reaction and was drop casted on a TEM grid immediately. Afterwards CD spectra were taken.

Photoelectronspectoscopy (XPS)

In the following XPS spectra of the prepared materials for different elements are shown. The binding energy in eV is plotted against the number of counts. A step size of 0.1 eV was chosen for all measurements. Spectra were recorded on a specs device equipped with a Phoibos 150 2D CCD hemispherical analyzer and Focus 500 monochromator. The detector angle was set perpendicular to the surface and the used X-ray source was aluminum Kα.

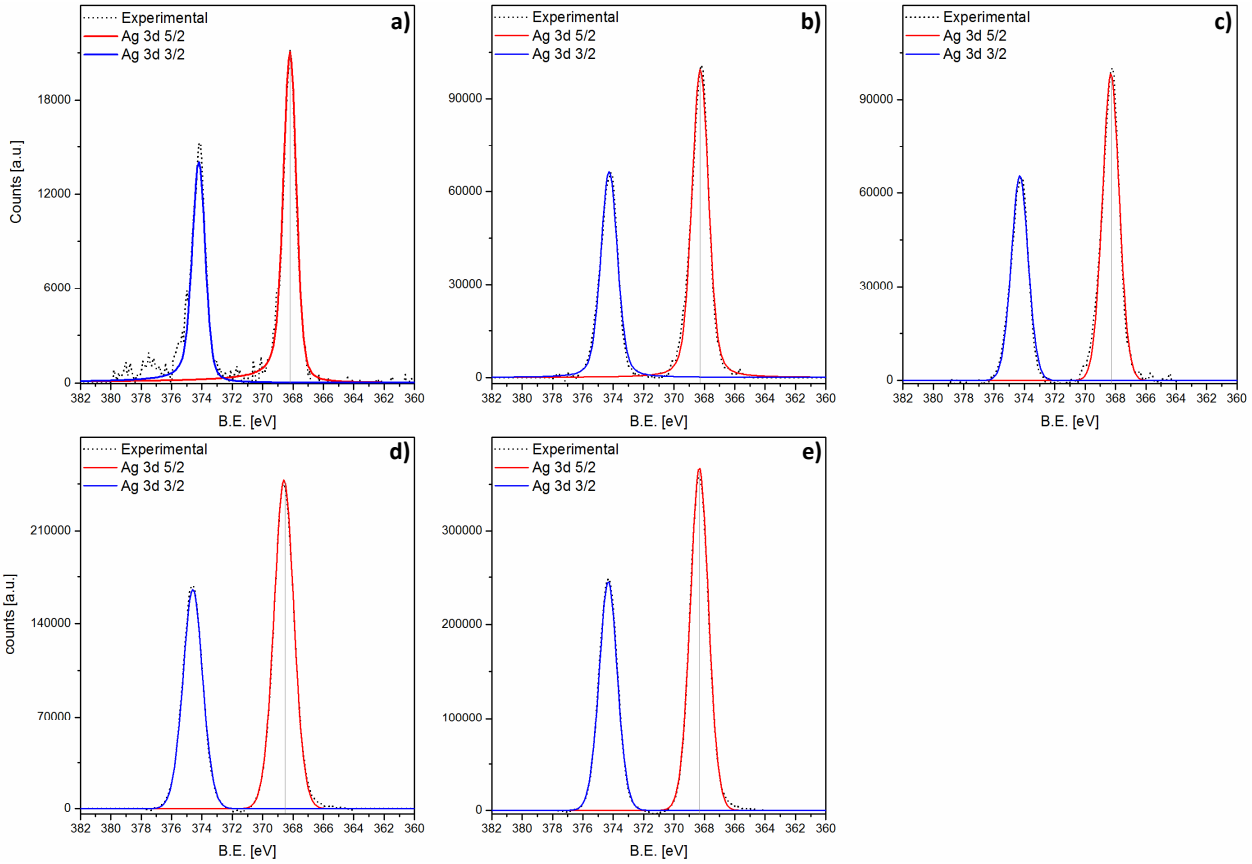

Fig. SI 4: Fitted XPS spectra of **Ag3d** are shown for **a)** citrate stabilized AgNP, **b)** L-Glutathione capped AgNP, **c)** L-Glutathione capped silver nanostructures, **d)** L-Cystein capped silver nanostructures and **e)** D-Cystein capped silver nanostructures. The experimental data are represented by dotted lines.

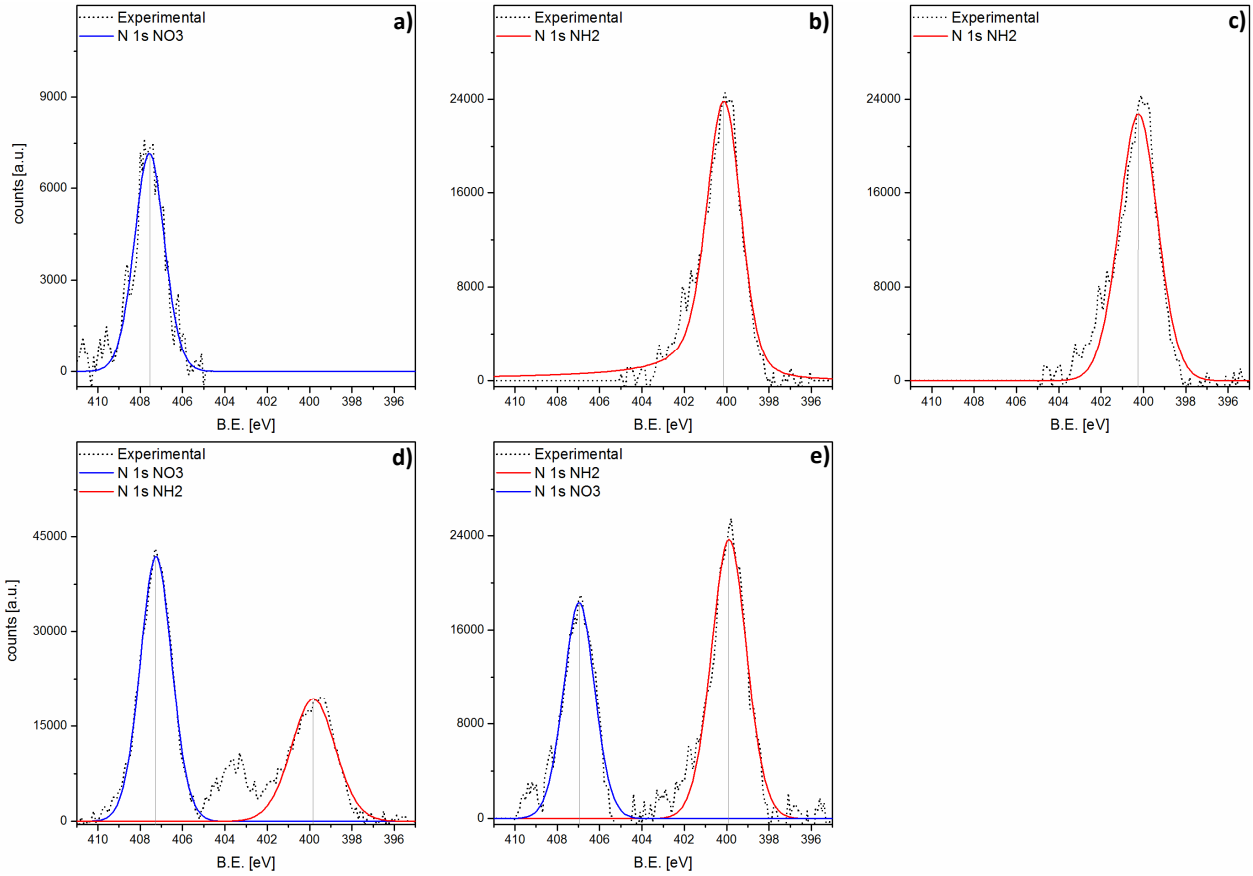

Fig. SI 5: Fitted XPS spectra of **N1s** are shown for **a)** citrate stabilized AgNP, **b)** L-Glutathione capped AgNP, **c)** L-Glutathione capped silver nanostructures, **d)** L-Cystein capped silver nanostructures and **e)** D-Cystein capped silver nanostructures. The experimental data are represented by dotted lines.

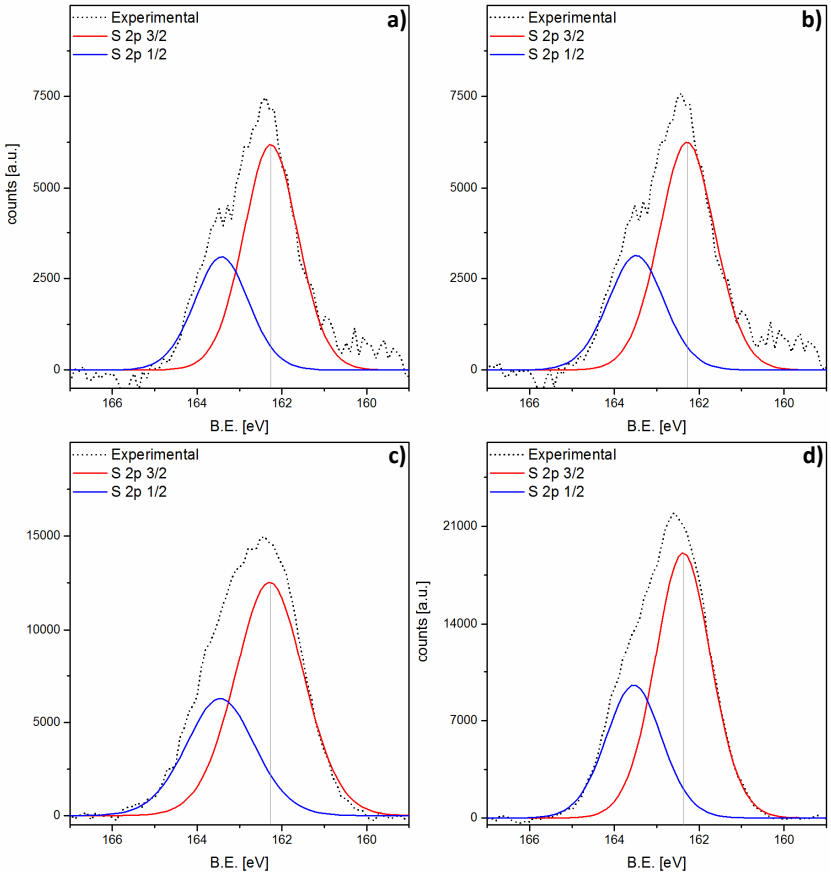

Fig. SI 6: Fitted XPS spectra of **S2p** are shown for **a)** L-Glutathione capped AgNP, **b)** L-Glutathione capped silver nanostructures, **c)** L-Cystein capped silver nanostructures and **d)** D-Cystein capped silver nanostructures. The experimental data are represented by dotted lines.

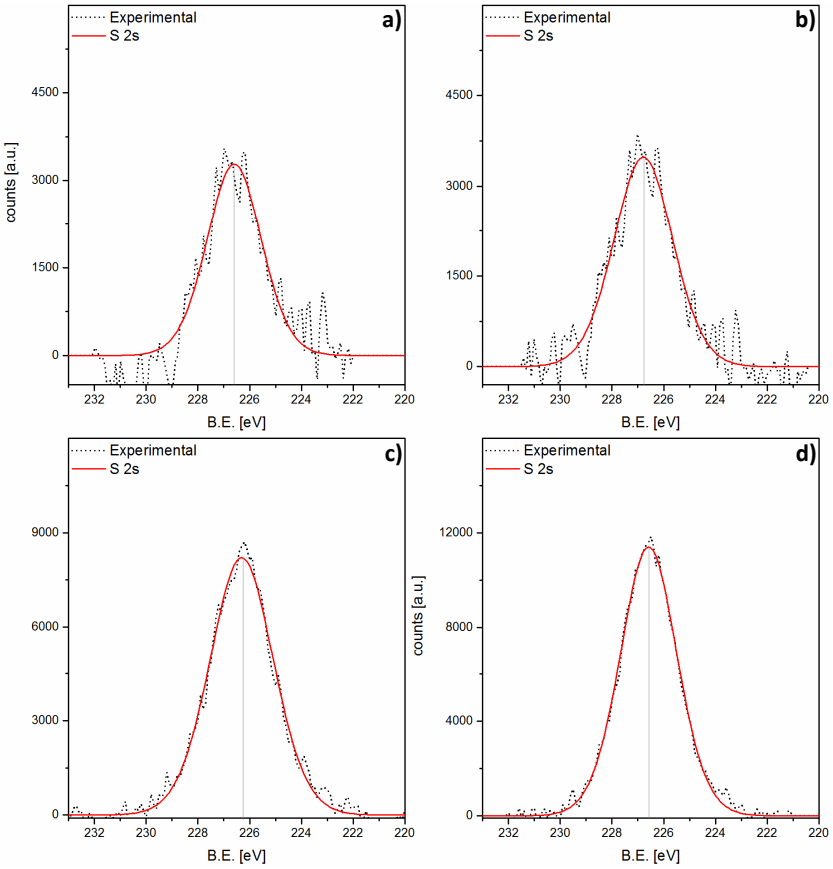

Fig. SI 7: Fitted XPS spectra of **S2s** are shown for **a)** L-Glutathione capped AgNP, **b)** L-Glutathione capped silver nanostructures, **c)** L-Cystein capped silver nanostructures and **d)** D-Cystein capped silver nanostructures. The experimental data are represented by dotted lines.

Scanning Electron Microscopy

To further investigate the composition of the obtained materials EDX analysis was performed for representative samples. Both samples have been cleaned by centrifugation and redispersion in UPW, also the structure made from Cysteine, as in EDX an intact particles can be picked for analysis. From the data in Table SI 1, it can be concluded, that the formed structures consist of elemental silver and not $AgNO_3$ as the nitrogen signal was below detection limit in both cases. Also it appears, that the structures have a similar composition regarding their relative content of silver and sulfur. SEM and EDX data were obtained with a JSM-7500F from JEOL equipped with an XMax detector from Oxford Instruments.

Table SI 1: Elemental Analysis by the means of EDX. Nitrogen is not shown as it was always below quantification limit. Measurements performed on a carbon coated TEM grid.

Used Ligand	Silver [atom %]	Sulfur [atom %]	Oxygen [atom %]	Carbon [atom %]
L-glutathione	14.51	3.98	19.19	62.62
D-cysteine	19.63	3.83	25.18	51.36

SEM images and EDX graphs

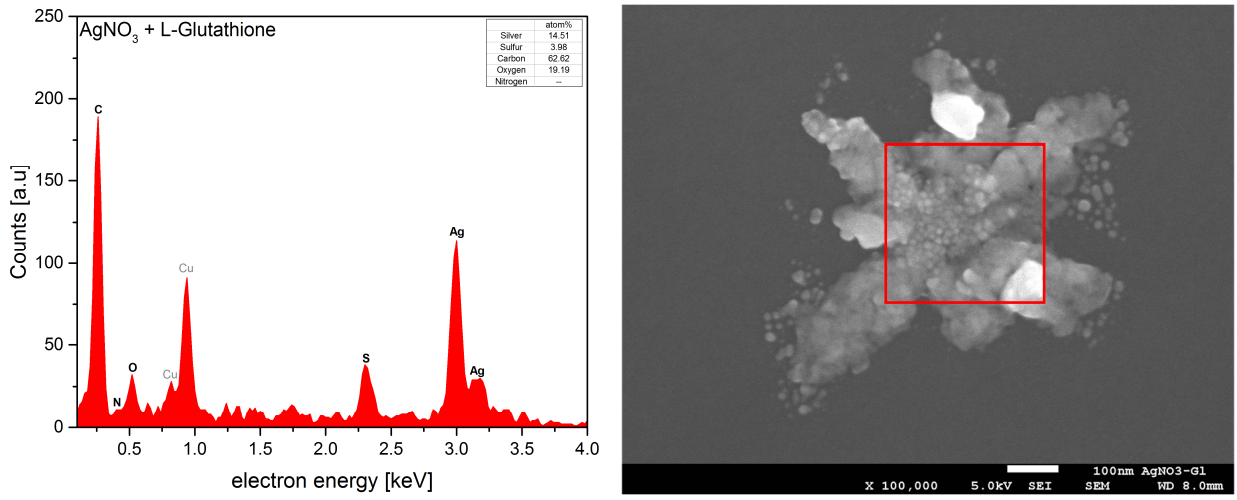

Fig. SI 8: EDX graph (left side) and SEM image including area of measurement (right side) for particles generated by reduction of $AgNO_3$ with L-Glutathione.

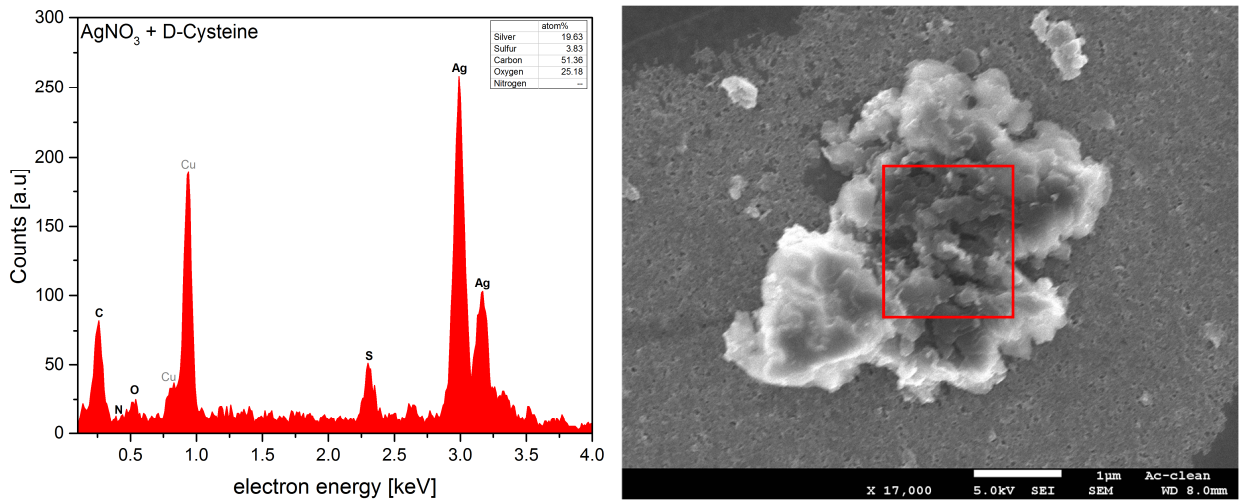

Fig. SI 9: EDX graph (left side) and SEM image including area of measurement (right side) for particles generated by reduction of $AgNO_3$ with D-Cysteine without heating.

6.2 Reappraising the Luminescence Lifetime Distributions in Silicon Nanocrystals

Matthias Jakob[1], Amira Aissiou[2], William Morrish[2], Frank Marsiglio[2], Muhammad Islam[3], Aras Kartouzian[1] and Alkiviathes Meldrum[2]*

[1] Department of Chemistry, Technical University of Munich, Lichtenbergstrasse 4, 85748 Garching, Germany.

[2] Department of Physics, University of Alberta, Edmonton, AB T6G 2E1, Canada.

[3] Department of Chemistry, University of Alberta, Edmonton, AB T6G 2G2, Canada

* corresponding author, Email: ameldrum@ualberta.ca

Reproduced from *Nanoscale Res. Lett.*, **2018**, *13*, 383.

Jakob *et al. Nanoscale Research Letters* (2018) 13:383
https://doi.org/10.1186/s11671-018-2785-x

Nanoscale Research Letters

NANO EXPRESS Open Access

Reappraising the Luminescence Lifetime Distributions in Silicon Nanocrystals

Matthias Jakob[1], Amira Aissiou[2], William Morrish[2], Frank Marsiglio[2], Muhammad Islam[3], Aras Kartouzian[1] and Alkiviathes Meldrum[2*]

Abstract

The luminescence dynamics in ensembles of nanocrystals are complicated by a variety of processes, including the size-dependence of the radiative and non-radiative rates in inhomogeneous broadened samples and interparticle interactions. This results in a non-exponential decay, which for the specific case of silicon nanocrystals (SiNCs) has been widely modeled with a Kohlrausch or "stretched exponential" (SE) function. We first derive the population decay function for a luminescence decay following $\exp[-(t/\tau)^{\beta}]$. We then compare the distributions and mean times calculated by assuming that either the luminescence decay or the population decay follows this function and show that the results are significantly different for β much below 1. We then apply these two types of SE functions as well as other models to the luminescence decay data from two thermally grown SiNC samples with different mean sizes. The mean lifetimes are strongly dependent on the experimental setup and the chosen fitting model, none of which appears to adequately describe the ensemble decay dynamics. Frequency-resolved spectroscopy (FRS) techniques are then applied to SiNCs in order to extract the lifetime distribution directly. The rate distribution has a half width of ~ 0.5 decades and mainly resembles a somewhat high-frequency-skewed lognormal function. The combination of TRS and FRS methods appear best suited to uncovering the luminescence dynamics of NC materials having a broad emission spectrum.

Keywords: Silicon nanocrystals, Time-resolved spectroscopy, Frequency-resolved spectroscopy, Lifetimes, Stretched exponential, Lognormal

Introduction

Colloidal nanoparticles can be used in a manifold of applications including catalysis, medical treatments, and optoelectronic applications [1–4]. Semiconductor nanoparticles are of particular interest for light emission, photovoltaic, and photocatalytic applications [5, 6]. Silicon nanocrystals (SiNCs) are a focus of current attention owing to the tunable emission properties [7] as well as the abundance and biocompatibility of silicon [8]. In order to develop nanoparticle-based technologies, a deep knowledge of the relevant optoelectronic properties is needed, and time-resolved spectroscopy is often a valuable tool for this purpose.

The luminescence lifetimes of SiNCs are usually modeled with a stretched exponential (SE) function having the basic form $\exp[-(\lambda t)^{\beta}]$, where the dispersion parameter β takes values between 0 and 1, λ is a rate parameter, and t is time. This function is often described as "slower than exponential" and implies an asymmetric distribution of decay rates tailing toward longer lifetimes. Once the β and λ parameters have been found by fitting a luminescence decay curve, the corresponding decay rate distribution can be approximately reconstructed [9].

The origin of the SE luminescence decay in silicon and other semiconductor quantum dots has been heavily debated in the last two decades, and the debate has continued recently [10]. Various explanations have been proposed for the appearance of the SE in the decay dynamics, including carrier tunneling and trapping in closely spaced ensembles of nanocrystals [11], the inhomogeneously broadened size distribution [12], size-dependent electron-phonon coupling [10], and a distribution of barrier heights for non-radiative recombination [13], the latter being similar to a previous suggestion for porous

* Correspondence: ameldrum@ualberta.ca
[2]Department of Physics, University of Alberta, Edmonton, AB T6G 2E1, Canada
Full list of author information is available at the end of the article

silicon [14]. Clearly, knowledge of the rate distribution is required for an understanding of the luminescence mechanism in SiNCs as well as in semiconductor nanocrystals more generally.

In much of the previous literature on SiNCs, the stretched exponential decay was assumed a priori, usually without analysis of other possible distributions. The SE tends to fit well visually (i.e., the best-fit line appears to match the data well "by eye"). Furthermore, in the vast majority of the previous works, e.g., [15], there is a lack of clarity about whether the population decay or the luminescence decay is actually being modeled. These are related by a derivative and one should use the correct expression in order to understand the decay timescales in the sample [16]. Also, the responsivity function of the detector can have a significant effect on the measured luminescence decay curve in SiNCs, due to the broad ensemble emission spectrum. Despite this, the responsivity has rarely if ever been taken into account, making it difficult to compare results from different investigations. Finally, no previous studies have attempted to use frequency-resolved spectroscopy (FRS) in the analysis of silicon nanocrystals. In principle, FRS permits the lifetime distribution to be extracted without assuming a model a priori.

The purpose of this paper is to establish an approach to measure, model, and interpret the luminescence dynamics of silicon nanocrystals. It is hoped that this could help to better understand the vast diversity of often contradictory results in the literature, lead to better agreement, or at least more consistency, between different measurements, and to better understand the luminescence mechanisms.

Basic Theory

We compare three models: the stretched exponential, which is widely used for Si nanocrystals, the lognormal decay distribution, which was first applied to SiNCs recently [17], and the bimolecular decay. For any model, the emission probability density function, represented by the integral of the intensity function $g(t)$, at time t' is related to the fraction of excitations remaining at t' according to [16].

$$\int_0^t g\left(t'\right)dt = 1 - \frac{c_t}{c_0}, \tag{1}$$

where c_t and c_0 are the number of excited NCs at time t and initially. The probability density function describes the fraction of photons emitted between time 0 and t relative to the total number of photons emitted. If the population decay follows a first-order rate equation (i.e., "monomolecular" recombination), we have $dc_t/dt = -\lambda c_t$, where $\lambda = 1/\tau_0$, leading to the usual $c_t/c_0 = \exp[-\lambda t]$ and $g(t) = \lambda \cdot \exp[-\lambda t]$ after taking the time derivative of both sides of Eq. 1. The derivative is necessary because the luminescence intensity measured in the window dt' is proportional to the change in the excited fraction over that interval.

If we consider both radiative and non-radiative rates, then we replace the total decay rate λ with $\lambda_R + \lambda_{NR}$ so that $g(t) = (\lambda_R + \lambda_{NR})\exp[-(\lambda_R + \lambda_{NR}t] = \lambda_R\exp[-(\lambda_{Ri} + \lambda_{NR})t] + \lambda_{NR}\exp[-(\lambda_R + \lambda_{NR})t]$ in which only the first term is measurable, yielding a measured intensity for time-resolved spectroscopy (TRS) given by

$$g(t) = \lambda_R \exp[-(\lambda_R + \lambda_{NR})t]. \tag{2}$$

The decay function used to fit the data, $I_t = A\cdot\exp(-\lambda t) + \mathrm{dc}$, scales with an additional arbitrary prefactor, A, which depends on the detection efficiency and the number of nanoparticles excited and will lead to the appropriate scale. A dc offset is usually added to the decay function as another fitting parameter.

In the case of the stretched exponential decay, the fraction of excited emitters decays according to

$$\frac{c_t}{c_0} = \exp\left[-(\lambda_{SE}t)^{\beta}\right]. \tag{3}$$

where λ_{SE} is the stretched exponential decay rate (equal to $1/\tau_{SE}$). Inserting this into Eq. 1 and taking the derivative of both sides as before yields an emission probability function given by

$$g(t) = \beta\lambda_{SE}^{\beta}t^{\beta-1}\exp\left[-(\lambda_{SE}t)^{\beta}\right]. \tag{4}$$

A way to estimate the distribution of frequencies $H(\lambda)$ that leads to Eq. 3 was shown using an inverse Laplace transform [9], yielding a distribution that widens with decreasing β and is skewed toward high frequencies.

Unfortunately, in Eq. 4, it is not possible to separate the prefactor into radiative and non-radiative parts. This means that Eq. 4 is correctly normalized only for $\lambda_{NR} = 0$ [16], and the lifetime distribution obtained from a PL decay curve is only understood in this way. Moreover, there is a time-dependent term in the prefactor; therefore, the population decay has a different time dependence as compared to the luminescence decay [16, 18]. In order to obtain values of τ_{SE} and β for the population decay from which the appropriate mean lifetimes can be extracted, one has to use Eq. 4 to model the observed decay, where we replace $g(t)$ by the measured decay function I_t:

$$I_t = A\beta\lambda_{SE}^{\beta}t^{\beta-1}\exp\left[-(\lambda_{SE}t)^{\beta}\right] + \mathrm{dc}. \tag{5}$$

In Eq. 5, a scaling parameter (which can also absorb the β and λ terms in the prefactor) and a dc offset

were inserted as fitting parameters. The mean lifetime is given by

$$\langle \tau_{SE} \rangle = \frac{\tau_{SE}}{\beta} \Gamma\left[\frac{1}{\beta}\right], \tag{6}$$

where Γ represents the Gamma function, and the mean decay time is

$$\langle t \rangle = \tau_{SE} \frac{\Gamma(2/\beta)}{\Gamma(1/\beta)}. \tag{7}$$

In much previous work, it has been common to use the "standard" stretched exponential $\exp[-(\lambda_{SE}t)^{\beta}]$ to model the luminescence decay instead of the population decay. Accordingly, we have a normalized intensity function given by

$$g(t) = \frac{\lambda_{SE}\beta}{\Gamma(1/\beta)} \exp\left[-(\lambda_{SE}t)^{\beta}\right]. \tag{8}$$

Equation 8 is normalized so that integration between $t = 0$ and ∞ is equal to 1. The corresponding fitting model is simply

$$I_t = A \exp\left[-(\lambda_{SE}t)^{\beta}\right] + \mathrm{dc}. \tag{9}$$

Equation 9 is widely applied and often fits the SiNC luminescence data quite well, despite the fact that (like Eq. 4) Eq. 8 is strictly normalized for an absolute quantum efficiency (AQY) of 100%. An often-overlooked point is the fact that one cannot extract τ_{SE} (= $1/\lambda_{SE}$) and β from the luminescence decay modeled by Eq. 9 and use them to calculate the mean times with Eqs. 6 and 7. Essentially, Eqs. 4 and 8 are different intensity decay models and one should expect different population decay functions, mean times, and decay rate distributions.

In order to find the population decay that would lead to an intensity function given by Eq. 9, we apply the same process we did to get from Eq. 4 to Eq. 5, but in reverse, that is:

$$\frac{c_t}{c_0} = 1 - \frac{\lambda_{SE}\beta}{\Gamma(1/\beta)} \int_0^t \exp\left[-(\lambda_{SE}t)^{\beta}\right] \cdot \mathrm{dt}. \tag{10}$$

After several steps, the solution to Eq. 10 is

$$\frac{c_t}{c_0} = \frac{1}{\Gamma(1/\beta)} \Gamma\left[1/\beta, (\lambda_{SE}t)^{\beta}\right]. \tag{11}$$

Equation 11 is the population decay obtained from the intensity decay given by Eq. 8. Finding the mean lifetime in the usual way leads to

$$\langle \tau_{SE} \rangle = \tau_{SE} \frac{\Gamma(2/\beta)}{\Gamma(1/\beta)} \tag{12}$$

and a mean decay time of

$$\langle t \rangle = \tau_{SE} \frac{\Gamma(3/B)}{2\Gamma(2/\beta)}. \tag{13}$$

Finally, the frequency distribution is $(1/\lambda)\cdot H(\lambda)$, where, as before, $H(\lambda)$ is the distribution calculated in ref. [9] for a population decay given by Eq. 3. These results are summarized in Table 1.

The differences between the two SE formulas are significant (Fig. 1). In the literature, one frequently finds that the intensity decay is modeled by $A\cdot\exp[-(t/\tau_{SE})^{\beta}]$ + dc (i.e., Eq. 9) and then the mean times are calculated using Eqs. 6 and 7. This appears to be mathematically incorrect, since Eqs. 6 and 7 are derived from an intensity decay given by Eq. 4, not Eq. 8. For example, taking $\tau_{SE} = 100$ μs and $\beta = 0.7$, as shown in Fig. 1, for an intensity decay given by $\exp[-(t/\tau_{SE})^{\beta}]$, we find a mean time constant of 199 μs (Eq. 12), as compared to 127 μs by using Eq. 6. Similar differences are found for the mean decay times (Eqs. 7 and 13). Additionally, there is an approach known as the Higashi-Kastner method for estimating a characteristic lifetime [19], which has been applied to SiNCs as an alternative to applying the SE decay model [20, 21]. In this model, the characteristic delay time, t_d, is simply taken as the peak of the decay data plotted as $I_t\cdot t$ vs. t. This was suggested to be equivalent to $(1/\beta)^{1/\beta}\cdot\tau_{SE}$ obtained from Eq. 9 [20].

Alternatively, the distribution of decay rates may follow a specific $H(\lambda)$, leading to a luminescence decay given by:

$$g(t) = \int_0^{\infty} \mathrm{H}(\lambda) \cdot \exp(-\lambda t)\mathrm{d}\lambda, \tag{14}$$

where $H(\lambda)$ represents the frequency-dependent distribution of decay rates. Equation 14 reduces to Eq. 2 if $H(\lambda)$ is equal to the Dirac delta function $\delta(\lambda - \lambda_0)$, or it can represent a continuous series of exponentials weighted by the selected distribution. A lognormal function seems a reasonable choice in nanocrystal systems since many nanocrystal ensembles naturally follow lognormal size distributions [22]. In order to avoid further confusion, we use the standard normalized definition of lognormal function given by:

$$H(\lambda) = \frac{1}{\lambda} \cdot \frac{1}{\sigma\sqrt{2\pi}} \exp\left[-\frac{(\ln\lambda - \mu)^2}{2\sigma^2}\right]. \tag{15}$$

so that the measured decay function is

Table 1 Formulas for stretched exponential population and luminescence decays. The approximate solution $H(\lambda)$ is shown in ref. [9]

Population decay c_t/c_0	Intensity decay $g(t)$	Mean time constant	Mean decay time	Rate distribution
$\exp[-(\lambda_{SE}t)^{\beta}]$	$\beta\lambda_{SE}^{\beta}t^{\beta-1}\ \exp[-(\lambda_{SE}t)^{\beta}]$	$\frac{\tau_{SE}}{\beta}\Gamma\left[\frac{1}{\beta}\right]$	$\tau_{SE}\frac{\Gamma(2/\beta)}{\Gamma(1/\beta)}$	$H(\lambda)$
$\frac{1}{\Gamma(1/\beta)}\Gamma[1/\beta,(\lambda_{SE}t)^{\beta}]$	$\frac{\lambda_{SE}\beta}{\Gamma(1/\beta)}\ \exp[-(\lambda_{SE}t)^{\beta}]$	$\tau_{SE}\frac{\Gamma(2/\beta)}{\Gamma(1/\beta)}$	$\tau_{SE}\frac{\Gamma(3/\beta)}{2\Gamma(2/\beta)}$	$H(\lambda)/\lambda$

$$I_t = A\cdot\int_0^{\infty}\left(\frac{1}{\lambda}\cdot\frac{1}{\sigma\sqrt{2\pi}}\ \exp\left[-\frac{(\ln\lambda-\mu)^2}{2\sigma^2}\right]\cdot\ \exp(-\lambda t)d\lambda\right)+dc. \tag{16}$$

As with the SE function, there are only two independent variables (as well as an offset and a scaling factor). The moments are defined as usual; i.e., the median rate is given by $exp(\mu)$, the mean by $exp(\mu+\sigma^2/2)$, and the most probable lifetime (the peak of the distribution) is $exp(\mu-\sigma^2)$. Previously, a non-standard distribution was employed [16] (i.e., a distribution that, while valid on its own, is not the commonly accepted lognormal distribution function). Equation 14 also applies to a radiative decay distribution (i.e., AQY = 100%). In fact, it has been suggested that decay rate distributions are weighted by an (unknown) quantum efficiency function [16]. In real situations, one simply has to accept this caveat given that it is difficult or impossible to know the population distribution of non-radiative rates in the sample.

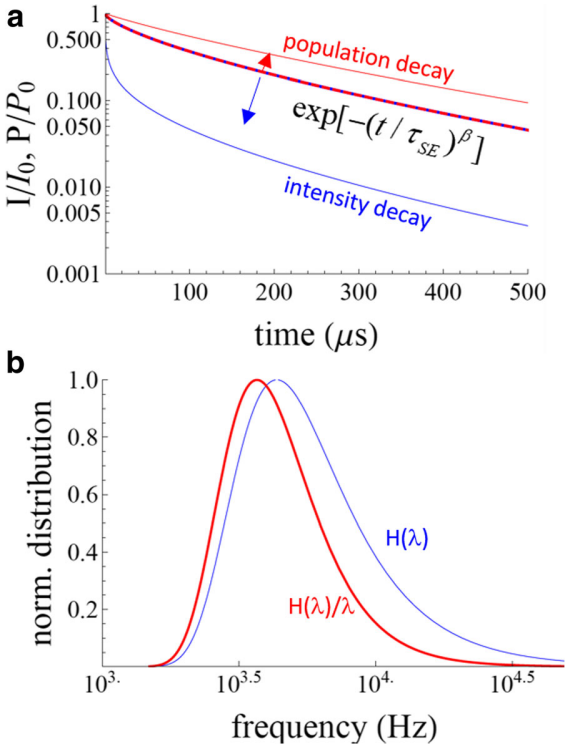

Fig. 1 Stretched exponentials. **a** Population and intensity decays for the stretched exponential function with τ_{SE} = 100 μs and β = 0.7. The blue-red dashed line is $\exp[-(\lambda t)^{\beta}]$. If this represents the population decay, then the intensity decay will be given by the blue line. If $\exp[-(\lambda t)^{\beta}]$ is the intensity decay, then the population decay is shown with the red line. **b** The corresponding rate distributions

Luminescence decays may also correspond to a second-order reaction (i.e., the "bimolecular" decay) [23]. Here, the rate at which the population decays is given by $dc/dt = -\lambda[c_t]^2$, which yields a remaining fraction $c_t/c_0 = (c_0\lambda t+1)^{-1}$. Inserting this expression into Eq. 1 results in a power law decay:

$$I_t/I_0 = A\frac{\lambda c_0}{(\lambda c_0+1)^2}. \tag{17}$$

The bimolecular model has only one rate constant λ (unlike the stretched exponential and lognormal, which have distributions of rates), and there is no mean lifetime. More specifically, the time integral diverges and the mean lifetime of the second-order decay is infinite.

The "standard" SE function (Eq. 9) has been by far the dominant model used for SiNC luminescence decays, with many papers devoted to interpreting the meaning of the decay for the luminescence mechanisms. The lognormal lifetime distribution was first applied to SiNCs quite recently [17, 24, 25]. Obviously, there is little a priori reason to assume any model, and it would instead be preferable to establish the distribution of decay rates directly. This can, in principle at least, be achieved by quadrature frequency-resolved spectroscopy (QFRS), which has been applied on several occasions to amorphous silicon but not to SiNCs.

Quadrature Frequency-Resolved Spectroscopy

The QFRS method is rather sparsely reported in the literature, mainly limited to a few studies of rare-earth-doped glasses [26–28] and amorphous silicon [29–31]. The basis of the technique is to excite the sample with a sine-wave-modulated pump beam of angular frequency ω and to measure the phase and amplitude of the luminescence as it attempts to track the excitation. With this setup, the quadrature component (Q) of a phase-sensitive detector (i.e., a lock-in amplifier) provides a direct measure of the lifetime distribution [30]. Since the amplitude of the AOM-modulated laser oscillation can be frequency-dependent, the quadrature component of the PL, $Q_{PL} = Z_{PL}sin(\Delta\theta_{PL})$ has to be normalized to the amplitude of the laser oscillation, Z_{LA}.

The quadrature FRS signal is complicated by the fact that a single exponential decay does not result in a delta function in the QFRS spectrum. The observed signal is in fact the convolution of the lifetime distribution with a single exponential response function given on a log scale by [31].

$$S_{\log_{10}r} = \frac{\omega\tau_0}{1+\omega^2\tau_0^2}, \tag{18}$$

Where the time constant $\tau_0 = \omega_0^{-1}$. Thus, unless the decay rate distribution is several decades wide, a deconvolution has to be performed in order to extract a meaningful distribution.

Results and Discussion

Basic Characterization

Due to the low contrast associated with the SiNCs and the overlapping mottled contrast from the amorphous carbon support, computer-based particle counting algorithms using bright-field images cannot be applied and the diameters had to be estimated "by eye" using pixel counting software (sample bright-field TEM images are shown in Fig. 2a, d and the manual particle counting results were fit with a lognormal distribution (Fig. 2c, f) in order to obtain a linear mean diameter of 2.9 nm (mean and standard deviation of the natural logarithms $\mu = 1.057$ and $\sigma = 0.1555$) and 5.4 nm ($\mu = 1.663$ and $\sigma = 0.1917$), for 1100 and 1200 °C annealing temperatures, respectively. These samples will henceforth be referred as "small" and "large" SiNCs. The sizes were further checked by high-resolution imaging of selected NCs (Fig. 2b, e), where the lattice fringes could be used as another way to identify the NCs and estimate their diameters. The Fourier transform infrared (FTIR) spectroscopy and XPS data showed that the prepared SiNCs were successfully functionalized with dodecene; however, the small SiNCs are more oxidized than the large ones and thus show a smaller degree of functionalization (Additional file 1: Figures S1 and S2).

Photoluminescence and Time-Resolved Spectroscopy

The photoluminescence (PL) spectra were centered at 660 and 825 nm with a full-width-at-half maximum of 123 and 198 nm for small and large SiNCs, respectively (Fig. 3 insets). The indirect bandgap energies are predicted to be 1.87 and 1.37 eV according to $E_g = \sqrt{E_{g,\mathrm{bulk}}^2 + D/R^2}$ [32] with $D = 4.8$ eV^2/nm^2 and R being the NC radius, which is in close agreement for the small particles but predicts a slightly smaller bandgap than obtained by the PL peak for the large ones. The AQY was 12% for the small SiNC sample and 56% for the large NCs. Independent measurements on a different system yielded 18% and 48% for the two samples, which is typical of the uncertainties in AQY measurements [33] for the different excitation and cutoff wavelengths. We hypothesize that the less curved, lower-energy surfaces of the larger NCs leads to a better surface functionalization and a smaller contribution from non-radiative surface states to the overall PL spectrum.

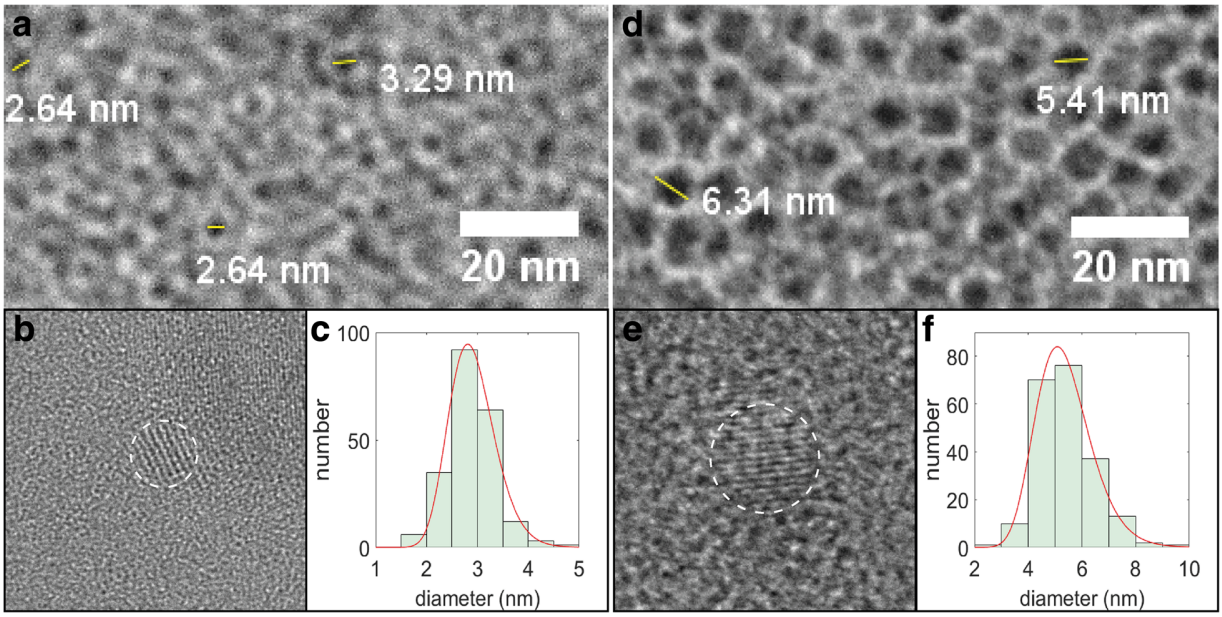

Fig. 2 TEM images of SiNCs. **a** Bright-field, **b** high resolution, and **c** size distribution histogram for the small SiNCs. Panels **d**–**f** represent a similar set of images from the large SiNCs

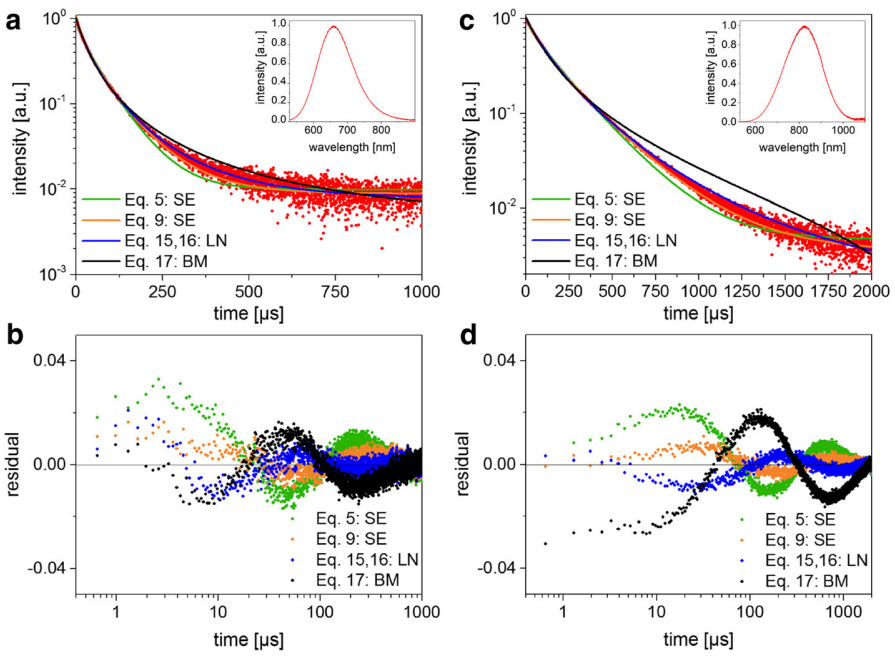

Fig. 3 TRS data and fitting results. **a** Luminescence decays and the corresponding fitting function (*BM* bimolecular, *SE* stretched exponential, *LN* lognormal) for small SiNCs. The PL spectrum is shown in the inset. **b** Residuals plots for the fits in (**a**, **c**, **d**) show the curves and residuals for the large SiNCs.

Both samples yielded a non-exponential decay, as expected on the basis of the extensive previous literature on SiNCs. The measured PL decays were fit with Eqs. 5, 9, 16, and 17 in order to test the different models using standard sum-of-squares minimization (Fig. 3). The fact that the detector responsivity is not constant over the wide NC luminescence spectrum will be discussed later. For all cases, the residuals oscillate, indicating that none of the models appears fully adequate, but the "simple" SE model (Eq. 9) and the lognormal (Eq. 16) tend toward the lowest sum of squares of the residuals. The calculated fitting parameters and mean lifetimes for the two SiNC samples are shown in Table 2, in which the means are clearly dependent on the selection of the decay model. The Higashi-Kastner method was also applied (Fig. 4) and the peak positions determined by fitting the delay time curves with a skewed Gaussian. The Higashi-Kastner method yields a time constant t_d quite similar to $(1/\beta)^{1/\beta}\cdot\tau_{SE}$, with these values take from Eq. 9 as shown before [20]. The bimolecular model fits fairly poorly, consistent with isolated nanocrystals that are not heavily over-excited. It will therefore not be further discussed.

In order to estimate the number of excitons per NC on average for these measurement conditions, the excitation rate has to be calculated from the absorption cross sections, which can evidently be as high as 10^{-14} cm^2 for these experiments [34]. Given an excitation irradiance of 4500 W/m^2 at 352 nm and the measured peak emission rates (see following sections), the number of excitations per NC for the large and small SiNCs was estimated to be less than ~ 1 and 0.2, respectively. This suggests that the large SiNCs may be slightly over-excited. This can cause additional non-radiative

Table 2 Fitting parameters, mean lifetimes, and mean decay times obtained for Eqs. 5, 9, and 16 for the small and large SiNC samples. For the lognormal function (Eq. 16), the last column shows the mode (i.e., the most common lifetime). All lifetimes are in microseconds

Sample	Equation 5				Equation 9				Equation 16				HK method
	τ_{SE}	β	$\langle t\rangle$	$\langle\tau_{SE}\rangle$	τ_{SE}	β	$\langle t\rangle$	$\langle\tau_{SE}\rangle$	μ	σ	$\langle\tau_{LN}\rangle$	$\langle\tau_{mode,\ LN}\rangle$	t_d
Small SiNCs	60.9	0.92	69.4	63.4	38.9	0.72	89.7	73.3	10.1	0.73	31.4	70.4	62.8
Large SiNCs	195	0.94	212	200	146	0.79	253	220	8.8	0.61	124	217	194.8

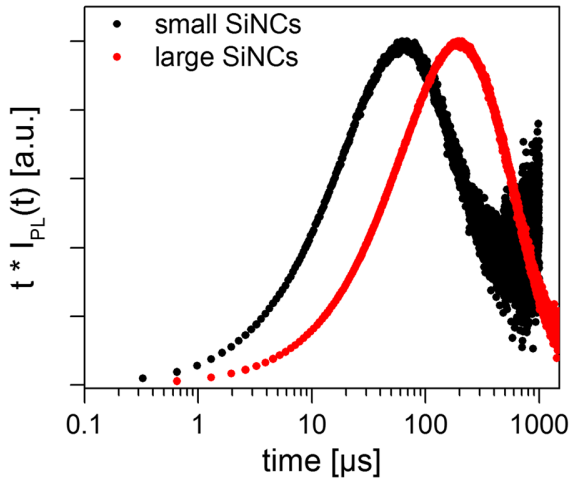

Fig. 4 Normalized PL decay curves multiplied by the decay time (Higashi-Kastner plots) for the small and large SiNC ensembles. The peak positions represent the most dominant decay time, represented by t_d in Table 2

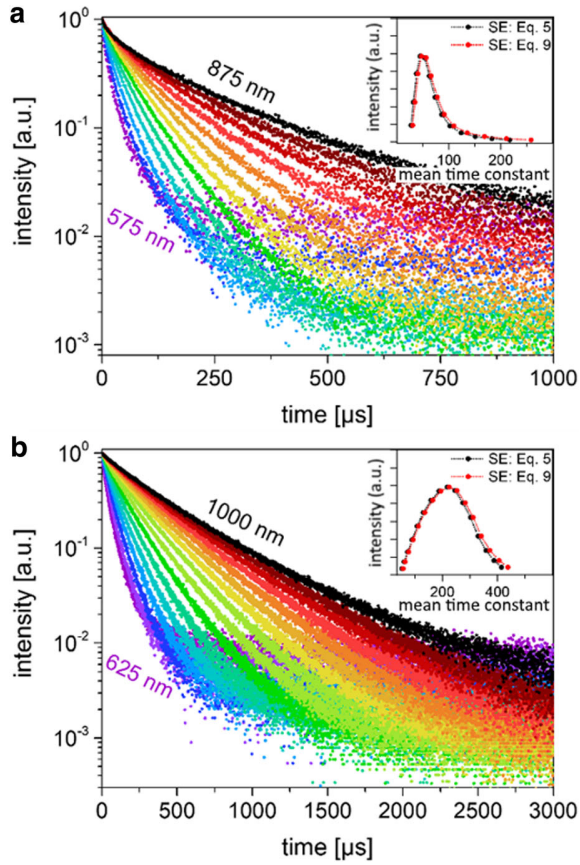

Fig. 5 Narrow-wavelength PL decays. **a** Luminescence decays for the small SiNCs at specific emission wavelengths (3 nm FWHM) ranging from 575 to 875 nm, in 25-nm intervals. The data were fit with Eqs. 5 and 9, which yielded a nearly single exponential fit. **b** Luminescence decays at specific emission wavelengths ranging from 625 to 1000 nm for the large SiNCs measured and fitted under the same conditions. The resulting time constants for the small and the large SiNCs are given in Table 1

effects due to the presence multi-excitons in some NCs. In order to further evaluate this possibility, the lifetime was measured as a function of excitation power; down to 2% of the values reported above. The results showed no trend and were always the same within ~ 2% (Additional file 1 Figure S3), which is close to the fitting and repeatability errors despite the low signal-to-noise ratio in the low-power measurements. Thus, the possible over-excitation of the NCs appears to have little effect on the results.

In order to estimate the lifetime distribution from TRS, the decays were measured over a set of fixed wavelengths using a monochromator with a ~ 3 nm bandpass (Fig. 5). Due to the low intensity, a photon-counting PMT system was used for this purpose. With effectively monochromatic radiation, there should be no difference in the decay constants measured with different detectors since there is negligible distribution of the response function over such a narrow range of wavelengths. The same trend was found for the dodecyl-terminated particles as observed for in other silicon NCs [25, 35, 36]; that is, the dispersion parameter increases closer to unity and the lifetime increases rapidly as a function of the wavelength (Fig. 5, Table 3).

The smaller particles always had a shorter lifetime than the larger ones at the same measurement wavelength. This observation is consistent with the lower AQY of the smaller particles, indicating that the lifetime of the large NCs is less strongly governed by non-radiative processes. The large NCs are also less oxidized in comparison to the small NC sample (Additional file 1 Figure S1). Thus, while the observation of the lower AQY on the small sample is consistent with the measured shorter lifetimes, one cannot make a relative comparison of the two samples via wavelength selection (basically, the emission wavelength depends on size *and* the degree of oxidation [24], which is different in the two samples).

Also plotted as insets in Fig. 5 are the distributions obtained by plotting the mean lifetimes obtained from the monochromated data, using Eqs. 5 or 9 to fit the data, as a function of the PL intensity at that wavelength. Since for these decays the beta parameter is reasonably close to 1, there is fairly little difference between the mean lifetimes calculated with the two versions of the SE model and the distributions obtained in this manner appear similar. While these decays do not represent the "true" distribution of lifetimes due to non-radiative contributions to I_{PL}, they can nevertheless give an indication of the lifetime distribution. For the small particles, we

Table 3 Wavelength dependence of the SiNCs lifetimes and fitting parameters obtained from Eq. 5 and 9. The lifetimes changed by almost an order of magnitude across the emission spectrum. The β values were above 0.8 in most cases

Small SiNCs						Large SiNCs					
λ (nm)	I_{PL}	$\beta_{Eq.\ 5}$	$\langle\tau_{SE}\rangle_{Eq.\ 5}$	$\beta_{Eq.\ 9}$	$\langle\tau_{SE}\rangle_{Eq.\ 9}$	λ (nm)	I_{PL}	$\beta_{Eq.\ 5}$	$\langle\tau_{SE}\rangle_{Eq.\ 5}$	$\beta_{Eq.\ 9}$	$\langle\tau_{SE}\rangle_{Eq.\ 9}$
575	0.19	0.85	27.3	0.65	30.2	–	–	–	–	–	–
600	0.45	0.89	31.7	0.71	34.6	–	–	–	–	–	–
625	0.77	0.92	37.6	0.76	40.4	625	0.08	0.92	53.1	0.76	57.7
650	0.97	0.93	44.5	0.80	47.2	650	0.15	0.94	61.2	0.82	64.7
675	0.95	0.94	53.2	0.82	56.2	675	0.26	0.96	73.9	0.86	77.4
700	0.74	0.95	62.4	0.84	65.6	700	0.39	0.96	89.8	0.87	93.5
725	0.50	0.95	73.5	0.83	77.7	725	0.55	0.97	108.5	0.88	112.8
750	0.31	0.95	86.0	0.83	91.2	750	0.70	0.97	130.9	0.89	136.0
775	0.18	0.94	102.0	0.81	109.5	775	0.84	0.97	158.3	0.89	164.6
800	0.10	0.93	123.6	0.78	135.2	800	0.94	0.98	187.2	0.90	194.2
825	0.06	0.92	150.8	0.74	168.5	825	0.98	0.98	217.1	0.91	224.3
850	0.04	0.92	182.9	0.71	210.8	850	0.94	0.98	245.7	0.92	253.0
875	0.02	0.91	217.0	0.68	258.0	875	0.81	0.98	274.1	0.91	282.6
–	–	–	–	–	–	900	0.65	0.98	301.9	0.92	311.6
–	–	–	–	–	–	925	0.44	0.98	329.6	0.91	341.1
–	–	–	–	–	–	950	0.28	0.98	358.3	0.91	372.6
–	–	–	–	–	–	975	0.16	0.98	387.5	0.89	405.9
–	–	–	–	–	–	1000	0.09	0.97	414.6	0.88	437.9

observe a peak at ~ 47 μs, whereas for the large NCs the peak is more symmetrical and centered around 220 μs.

Frequency-Resolved Spectroscopy

We started by validating the FRS data from two test standards: the first one was an RC circuit and the second was a sample of fluorescent Eu-chelate-doped microspheres (Fisher Scientific). The RC circuit has a mono-exponential decay in which the FRS data matched Eq. 9 quite closely and peaked at 12.7 kHz, in agreement with the measured decay time constant of 78.9 μs. The Eu-chelate PL spectrum peaked at 650 nm with a decay time in the order of hundreds of microseconds, presenting a standard for the Si NCs. The luminescence also decayed nearly mono-exponentially with a lifetime of 670 μs. The FRS data was centered at ~ 1570 Hz with a width virtually equal to the response function (Eq. 18), which is fairly close to the observed TRS result. The difference (636 vs. 670 μs) might be due to the slightly non-exponential behavior of the decay coupled to the excitation method, as discussed further below.

The FRS data for the Si-NCs is problematic because the observed QFRS results turned out to be only slightly broader than the response function (see the inset to Fig. 6a). Therefore, a deconvolution has to be performed on the data, which need to be nearly free of noise in order to avoid significant problems with the deconvolution procedure. We used the Richardson-Lucy deconvolution method [37] in order to enforce a positivity constraint. The deconvolved and normalized QFRS data then yield the measured lifetime distribution directly, as shown in Fig. 6 for the large and small NCs, respectively (red points), without assuming any model a priori. For both samples, we find a broad lifetime distribution that, in the case of the large NCs, is slightly skewed toward higher frequencies, whereas the small NCs distribution is more nearly symmetrical on a semi-log plot. The decay rate distribution peaked at 19,900 Hz (50.3 μs) for the small NCs, whereas for the larger NCs the distribution peaked at 6280 Hz (159.2 μs).

The lifetime distributions obtained from the stretched exponentials (orange and green curves) and lognormal (blue curve) model fits are also plotted in Fig. 6 for the large and small particles. The three decay models yield different distributions, both in terms of the overall shape and the peak frequencies. For both samples, the QFRS peaks at a higher frequency than any of the TRS model fits. While this may seem surprising, the same effects have been observed for CdSe NCs having a distribution of lifetimes [38, 39]. In fact, the TRS decay curve for CdSe NCs was evidently sensitive to the pulse duration, with shorter pulses accentuating the shorter lifetimes and the opposite case for long pulses.

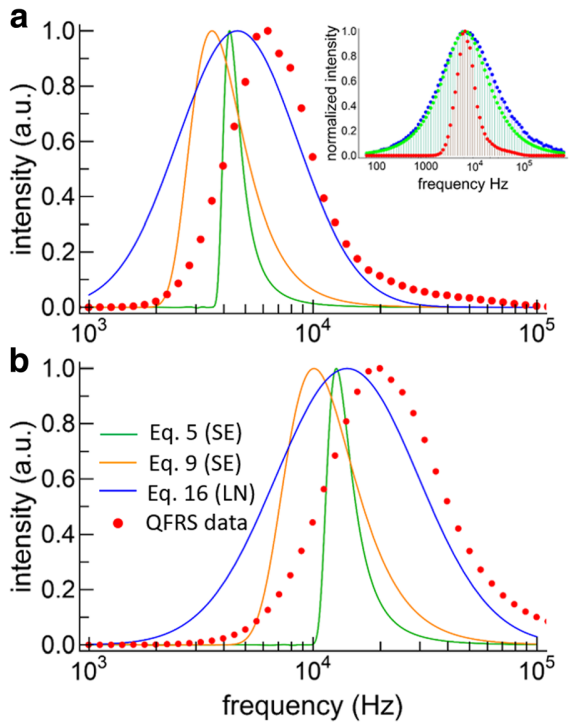

Fig. 6 Lifetime distributions. **a** Lifetime distributions for large SiNCs obtained from fitting the TRS data with the two SE models and the LN model. The deconvolved QFRS data is also shown (red points). The inset shows the raw QFRS data for this sample (blue), the response function (green), and the deconvolution (red). **b** Lifetime distributions obtained by model fitting the TRS data (lines, same color scheme for both graphs) and QFRS (red points) for the small SiNCs

Furthermore, the mean lifetimes obtained by long-pulse duration techniques were a factor of 3–4 times longer than those obtained by phase measurement, which was due to preferential excitation of the long-lived population in steady-state excitation [38]. Indeed, the response function for TRS with a slow repetition rate is narrower than for FRS, cutting off especially sharply on the high frequency side [29]. Essentially, FRS accentuates the short-lived components of the ensemble decay more than steady-state TRS does, and this may account for the difference in the peak frequencies obtained by TRS model fitting and FRS. Despite these inherent differences, FRS appears suited to uncovering the distribution of lifetimes in ensembles of SiNCs, because it is obtained by direct measurement rather than by an assumed model. For SiNCs typical of a thermally grown ensemble, the main drawback of FRS is the necessity of a deconvolution.

While the detector response function certainly affects the QFRS, it plays a role in the TRS data as well. Indeed, measuring the ensemble decay with the APD vs. the PMT setup yielded mean decay times that were different by a factor of ~ 2, regardless of the fitting model applied. The detector responsivity also affects choice of the TRS "best" model fit. As mentioned above, our Thorlabs APD responsivity peaks at 600 nm, whereas for our Hamamatsu PMT the responsivity maximizes at 850 nm, in the long-wavelength, slow-decay part of the SiNC spectrum. Although apparently not reported before in the literature on SiNCs, this issue means that wide-spectrum TRS results from different setups are not comparable. Unfortunately, despite some critical conclusions, ref. [38] also used different detectors to compare the decay dynamics from the same wide-band NC sample and the response functions may not have been the same. Fortunately, however, the phase measurements and the steady-state measurements used the same detector (as was the case here) and the differences in the observed dynamics for these situations remain valid. Finally, the detector response function is in principle correctable in the FRS data if the responsivity curve and monochromated decay rate distribution are known over a wide range of wavelengths (i.e., decay rates). The responsivity correction has no such simple solution with TRS alone.

Conclusions

The most common models used for SiNC luminescence decay were described theoretically. The population decay corresponding to the "simple" stretched exponential luminescence decay, $\exp[-(t/\tau)^{\beta}]$, was derived and expressions for the characteristic mean times were found. This model was compared against the alternative model in which the population decays according to the simple SE. Two dodecene-functionalized SiNCs samples were then prepared from thermal nucleation and growth, followed by etching and alkane surface functionalization. These samples consisted of particles with mean diameters of 2.9 and 5.4 nm, respectively. The basic PL spectrum and TRS was measured using standard methods. The TRS data were fit with several distributions in order to establish whether any of them can be considered "true" and to find which one yields the best fit. While the simple SE luminescence decay fits the TRS data reasonably well, the distribution of residuals shows that it is not strictly accurate. None of the fitting models fully captures the shape of the measured decay rate distribution; they also show large deviations in the peak position and the shape of the distribution, as well as disagreement in the average time constants. Furthermore, the ensemble mean time constants were dependent on the responsivity curve of the detection system. This leads to serious questions about how to interpret the PL decay from ensembles of thermally-grown SiNCs.

Quadrature frequency-resolved spectroscopy was then employed with the intent to find the lifetime distribution directly for SiNC ensembles formed by thermal annealing of a base oxide. The spectrum was found to be not much wider than the intrinsic QFRS response function, requiring a deconvolution in order to extract the SiNC rate distribution. This yielded a distribution whose shape was nearly symmetrical (on a semilog scale) for the small NC sample and about half a decade wide, whereas it was slightly more skewed for the large NCs. We find that FRS techniques are suited to the study of SiNC luminescence dynamics and, after deconvolving the system response from the data, FRS yields the decay rate distribution directly. The most significant problem is the required deconvolution, but the Richardson-Lucy method was found to produce fairly robust results. While the detector response function can in principle be corrected from the FRS data, there is no simple means to do this for wide-PL-band TRS data. Still, as long as the data compared are from the same detector then the results should at least be internally meaningful. Hopefully in the future, these issues will be more fully considered when analyzing inhomogeneously broadened NC luminescence lifetimes, rather than defaulting to the simple stretched exponential model (Eq. 9) to describe and characterize the dynamical processes at work in the PL spectrum.

Methods

The SiNCs were synthesized according to a recently-proposed method [21]. Briefly, 4 g of hydrogen silsesquioxane (HSQ) was annealed at 1100 or 1200 °C for 1 h in a flowing 5% H_2 + 95% Ar atmosphere, resulting in composites of SiNCs embedded in a silica matrix. These composites were mechanically ground into a fine powder using an agate mortar. The powder was shaken for about 8 h with glass beads using a wrist action shaker. The powders were suspended in 95% ethanol and interfaced to a vacuum filtration system equipped with a filter. To liberate the H-SiNCs, the silica matrix was removed via HF etching. An approximately 200 mg aliquot of the composite was transferred to a Teflon beaker to which 2 mL of ethanol, 2 mL of water, and 2 mL of 49% HF aqueous solution were added in order to dissolve the silica matrix. After stirring the suspension for 40 min, the liberated H-SiNCs were extracted as a cloudy yellow suspension using toluene and isolated by centrifugation at 3000 rpm for 5 min. The resulting hydrogen-terminated SiNCs were suspended in 10 mL dry toluene, and then transferred to an oven-dried Schlenk flask equipped with a magnetic stir bar. Subsequently, 1 mL of 1-dodecene (ca. 4.6 mmol), as well as 20 mg of AIBN were added. The suspension was subjected to three freeze-pump-thaw cycles using an Ar charged Schlenk line. After warming the suspension to room temperature, it was stirred for 24 h at 70 °C, and 10 mL of methanol and 20 mL of ethanol were subsequently added to the transparent reaction mixture. The resulting cloudy suspension was transferred to a 50 mL PTFE vial and the SiNCs were isolated by centrifugation at 12,000 rpm for 20 min. The SiNCs were re-dispersed in 10 mL toluene and isolated by addition of 30 mL ethanol antisolvent followed by another centrifugation. The latter procedure was carried out one more time. Finally, the dodecyl-SiNCs were re-dispersed in 5 mL dry toluene and stored in a screw capped vial (concentration ~ 0.5 mg/mL) for optical studies.

TEM samples were prepared by depositing the free-standing nanoparticles directly onto an ultrathin (ca. 3 nm) carbon-coated copper TEM grid. The NCs were imaged by bright-field TEM using a JEOL JEM-2010 and HRTEM was done on a JEOL JEM-ARM200CF. Fourier transform infrared spectroscopy (FTIR) was performed in a Nicolet 8700 from Thermo Scientific. X-ray photo-electron spectroscopy was measured in a SPECS system equipped with a Phoibos 150 2D CCD hemispherical analyzer and a Focus 500 monochromator. The detector angle was set perpendicular to the surface and the X-ray source was the Mg Kα line.

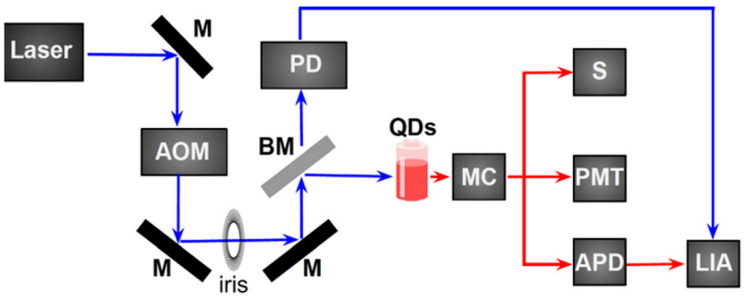

Fig. 7 Diagram of the experimental setup. *M* mirror, *AOM* acousto-optic modulator, *BM* beamsplitter, *PD* photodiode, *MC* monochromator, *S* spectrometer, *PMT* photomultiplier tube, *APD* avalanche photodiode, *LIA* lock-in amplifier

Luminescence spectra were excited with a 352-nm Ar^+ ion laser, which was pulsed (50% duty cycle, 50–250 Hz) using an Isomet IMDD-T110 L-1.5 acousto-optic modulator (AOM) with a fall time of ~ 50 ns. The used setup is schematically depicted in Fig. 7. The laser beam passes the acousto-optic modulator and one of the diffracted beams is selected by an iris. A beamsplitter reflects the main part of the pulsed laser beam into the sample cuvette and the incident power on the sample was ~ 8 mW spread over an area of ~ 4 mm^2. The luminescence was collected with an optical fiber (numerical aperture 0.22), sent through a 450-nm longpass filter and is guided to the appropriate detector. The PL spectrum was measured by an Ocean Optics miniature spectrometer whose response function was corrected using a calibrated radiation source (the HL-3 + -CAL from Ocean Optics). The quantum efficiency was measured using an integrating sphere with 405-nm excitation, using a solution diluted to have an absorbance of ~ 0.15 at that wavelength.

The luminescence dynamics were measured with two different detectors. The first detector was the Thorlabs 120A2 avalanche photodiode (50 MHz roll-off), which was interfaced to a Moku:Lab (200 MHz) in digital oscilloscope mode. The second detector was a Hamamatsu h7422-50 photomultiplier tube interfaced to a Becker-Hickl PMS400 multiscalar. The error in the luminescence decay times was obtained by repeating the measurements three times, yielding a standard error in the mean lifetime calculated using the stretched exponential fit (Eq. 4) of 1 μs. All fits to the decay data were done in Origin using the least linear squares with the Levenberg-Marquardt algorithm, and were repeated in Matlab using the same method. For wavelength -dependent decay measurements, the luminescence was sent through an Acton MS2500i monochromator prior to detection, with the half width of the detected radiation set to ~ 3 nm.

For QFRS measurements, the AOM was set to produce a sinusoidal oscillation. A part of the incident beam was deflected into a Thorlabs PDA10A photodiode (200 MHz) in order to generate the reference signal. The SiNC PL response was simultaneously collected and sent to the APD. The reference signal was obtained using the beamsplitter, and along with the corresponding PL signal, was analyzed using the Moku:Lab in the lock-in amplifier mode to measure the in-phase and quadrature components of the signal.

Finally, we also searched for a short-lifetime component in the luminescence, as has sometimes been reported previously and attributed to oxidation [22]. This system used a 405-nm picosecond diode laser (Alphalas GmbH) to excite the NCs, and a Becker-Hickl HPM-100-50 PMT interfaced to an SPC-130 pulse counter system. This setup has a response time of ~ 100 ps. No evidence of a nanosecond decay was observed in these SiNCs.

Additional File

Additional file 1: Figure S1. Normalized FTIR spectra of the synthesized SiNCs. The IR spectra and thus the surface composition is similar. However, it can be seen that the small SiNCs are more oxidized than the large particles (higher ratio of silicon oxide to CH_3 bands). **Figure S2.** XPS spectra for the Si 2p orbital of the investigated particles. The ratio of oxide species to elemental silicon is considerably smaller for the large SiNCs. The XPS spectra were referenced to the Carbon C1s peak at 284.8 eV. **Figure S3.** PL intensity plotted against the excitation power for the large SiNCs. An 352 nm Ar+ ion laser beam was used to excite the sample. **Table S1.** Excitation power dependence of the SiNCs fitting parameters obtained from Eq. 4. The decay time τ and the stretching factor β remains almost the same within the used excitation powers. (DOCX 81 kb)

Abbreviations

APD: Avalanche photodiode; AQY: Absolute quantum yield; FRS: Frequency-resolved spectroscopy; LN: Lognormal; NCs: Nanocrystals; PL: Photoluminescence; PMT: Photomultiplier tube; QFRS: Quadrature frequency-resolved spectroscopy; SE: Stretched exponential; SiNCs: Silicon nanocrystals; TRS: Time-resolved spectroscopy

Acknowledgements

We thank Prof. Ulrich Heiz for helpful discussions, and Jinkun Cheng and Mauricio Sacchi for discussions on deconvolution procedures.

Funding

DFG (IRTG 2022) and NSERC (CREATE grant 463990-2015) and Alberta/Technische Universität München Graduate School for Functional Hybrid Materials (ATUMs).

Availability of Data and Materials

All collected data is kept by MJ and/or AM.

Authors' Contributions

MJ conducted most of the experiments, performed analyses, and helped write the MS. AA performed some experiments and analyses and contributed to the MS. WM assisted with coding, deconvolution, and MS preparation. FM led the theory and derivations. MA provided test samples needed to start the project. AK assisted with sample preparation and characterization. AM wrote the MS, performed analyses, and conceived the work. All authors read and approved the final manuscript.

Competing Interests

The authors declare that they have no competing interests.

Publisher's Note

Author details

[1]Department of Chemistry, Technical University of Munich, Lichtenbergstrasse 4, 85748 Garching, Germany. [2]Department of Physics, University of Alberta, Edmonton, AB T6G 2E1, Canada. [3]Department of Chemistry, University of Alberta, Edmonton, AB T6G 2G2, Canada.

Received: 18 July 2018 Accepted: 6 November 2018
Published online: 28 November 2018

References

1. Johnson BFG (2003) Nanoparticles in catalysis. Top Catal 24:147–159
2. Tong X, Kong X-T, Zhou Y, Navarro-Pardo F, Selopal GS, Sun S, Govorov AO, Zhao H, Wang ZM, Rosei F (2018) Quantum dots: near-infrared, heavy

metal-free colloidal "Giant" core/shell quantum dots (Adv. Energy mater. 2/2018). Adv Energy Mater 8:1870010
3. Rao J, Dragulescu-Andrasi A, Yao H (2007) Fluorescence imaging in vivo: recent advances. Curr Opin Biotechnol 18:17–25
4. Lohse SE, Murphy CJ (2012) Applications of colloidal inorganic nanoparticles: from medicine to energy. J Am Chem Soc 134:15607–15620
5. Kamat PV (2008) Quantum dot solar cells. Semiconductor nanocrystals as light harvesters. J. Phys. Chem. C 112:18737–18753
6. Tong X, Kong XT, Wang C, Zhou Y, Navarro-Pardo F, Barba D, Ma D, Sun S, Govorov AO, Zhao H, Wang ZM, Rosei F (2018) Optoelectronic properties in near-infrared colloidal heterostructured pyramidal "Giant" core/shell quantum dots. Adv Sci (Weinh) 5:1800656
7. Dasog M, Kehrle J, Rieger B, Veinot JG (2016) Silicon nanocrystals and silicon-polymer hybrids: synthesis, surface engineering, and applications. Angew Chem Int Ed Engl 55:2322–2339
8. Park JH, Gu L, von Maltzahn G, Ruoslahti E, Bhatia SN, Sailor MJ (2009) Biodegradable luminescent porous silicon nanoparticles for in vivo applications. Nat Mater 8:331–336
9. Berberan-Santos MN, Bodunov EN, Valeur B (2005) Mathematical functions for the analysis of luminescence decays with underlying distributions 1. Kohlrausch decay function (stretched exponential). Chem Phys 315:171–182
10. Brown SL, Krishnan R, Elbaradei A, Sivaguru J, Sibi MP, Hobbie EK (2017) Origin of stretched-exponential photoluminescence relaxation in size-separated silicon nanocrystals. AIP Adv 7:055314
11. Pavesi L, Ceschini M (1993) Stretched-exponential decay of the luminescence in porous silicon. Phys Rev B 48:17625–17628
12. Ondic L, Varga M, Pelant I, Valenta J, Kromka A, Elliman RG (2017) Silicon nanocrystal-based photonic crystal slabs with broadband and efficient directional light emission. Sci Rep 7:5763
13. Mihalcescu I, Vial JC, Romestain R (1996) Carrier localization in porous silicon investigated by time-resolved luminescence analysis. J Appl Phys 80:2404–2411
14. Sawada S, Hamada N, Ookubo N (1994) Mechanisms of visible photoluminescence in porous silicon. Phys Rev B 49:5236–5245
15. Glover M, Meldrum A (2005) Effect of "buffer layers" on the optical properties of silicon nanocrystal superlattices. Opt Mater 27:977–982
16. van Driel AF, Nikolaev IS, Vergeer P, Lodahl P, Vanmaekelbergh D, Vos WL (2007) Statistical analysis of time-resolved emission from ensembles of semiconductor quantum dots: Interpretation of exponential decay models. Physical Review B 75:035329
17. Nguyen A, Gonzalez CM, Sinelnikov R, Newman W, Sun S, Lockwood R, Veinot JG, Meldrum A (2016) Detection of nitroaromatics in the solid, solution, and vapor phases using silicon quantum dot sensors. Nanotechnology 27:105501
18. Zatryb G, Podhorodecki A, Misiewicz J, Cardin J, Gourbilleau F (2011) On the nature of the stretched exponential photoluminescence decay for silicon nanocrystals. Nanoscale Res Lett 6:106
19. Higashi GS, Kastner MA (2006) Excitation-energy dependence of the photoluminescence total-light decay in arsenic chalcogenides. Philos Mag B 47:83–98
20. Hartel AM, Gutsch S, Hiller D, Zacharias M (2013) Intrinsic nonradiative recombination in ensembles of silicon nanocrystals. Phys Rev B 87:035428
21. Valenta J, Greben M, Remeš Z, Gutsch S, Hiller D, Zacharias M (2016) Determination of absorption cross-section of Si nanocrystals by two independent methods based on either absorption or luminescence. Appl Phys Lett 108:023102
22. de Lamaestre RE, Bernas H (2006) Significance of lognormal nanocrystal size distributions. Phys Rev B 73:125317
23. Huntley DJ (2006) An explanation of the power-law decay of luminescence. J Phys Condens Matter 18:1359–1365
24. Sinelnikov R, Dasog M, Beamish J, Meldrum A, Veinot JGC (2017) "Revisiting an ongoing debate: what role do surface groups play in silicon nanocrystal photoluminescence?," ACS photonics 4:1920–1929.
25. Greben M, Khoroshyy P, Liu X, Pi X, Valenta J (2017) Fully radiative relaxation of silicon nanocrystals in colloidal ensemble revealed by advanced treatment of decay kinetics. J Appl Phys 122:034304
26. Aoki T, Koughia K, Fujimoto K, Fujihashi C, DeCorby R, Haugen C, Hewak DW, Tonchev D, Kasap S (2009) Observation of 4F3/2→4I15/2 radiative transition in Nd3+ ions in GaLaS glass using frequency-resolved PL spectroscopy. physica status solidi (c) 6:S54–S58
27. Aoki T, Saitou D, Fujimoto K, Fujihashi C, Shimakawa K, Koughia K, Kasap SO (2010) Quadrature frequency resolved spectroscopy (QFRS) of radiative transitions of Er3+and Nd3+ions in chalcogenide glasses (ChGs). J Phys Conf Ser 253:012010
28. Tessler LR, Biggemann D (2003) Temperature independent Er3+ photoluminescence lifetime in a-Si:H<Er> and a-SiOx:H<Er>. Mater Sci Eng B 105:165–168
29. Dunstan DJ (1982) Kinetics of distant-pair recombination .1. amorphous-silicon luminescence at low-temperature. Philosophical Magazine B-Physics of Condensed Matter Statistical Mechanics Electronic Optical and Magnetic Properties 46:579–594
30. Depinna SP, Dunstan DJ (1984) Frequency-resolved spectroscopy and its application to the analysis of recombination in semiconductors. Philosophical Magazine B-Physics of Condensed Matter Statistical Mechanics Electronic Optical and Magnetic Properties 50:579–597
31. Stachowitz R, Schubert M, Fuhs W (1994) Frequency-resolved spectroscopy and its application to low-temperature geminate recombination in a-Si: H. Philosophical Magazine Part B 70:1219–1230
32. Belyakov VA, Burdov VA, Lockwood R, Meldrum A (2008) Silicon nanocrystals: fundamental theory and implications for stimulated emission. Advances in Optical Technologies 2008:1–32
33. Leyre S, Coutino-Gonzalez E, Joos JJ, Ryckaert J, Meuret Y, Poelman D, Smet PF, Durinck G, Hofkens J, Deconinck G, Hanselaer P (2014) Absolute determination of photoluminescence quantum efficiency using an integrating sphere setup. Rev Sci Instrum 85:123115
34. Kovalev D, Diener J, Heckler H, Polisski G, Kunzner N, Koch F (2000) Optical absorption cross sections of Si nanocrystals. Phys Rev B 61:4485–4487
35. Meier C, Gondorf A, Lüttjohann S, Lorke A, Wiggers H (2007) Silicon nanoparticles: absorption, emission, and the nature of the electronic bandgap. J Appl Phys 101:103112
36. Huisken F, Ledoux G, Guillois O, Reynaud C (2002) Light-emitting silicon nanocrystals from laser pyrolysis. Adv Mater 14:1861–1865
37. Richardson WH (1972) Bayesian-based iterative method of image restoration. J. Opt. Soc. Am 62:55–59
38. Martin JE, Shea-Rohwer LE (2006) Lifetime determination of materials that exhibit a stretched exponential luminescent decay. J Lumin 121:573–587
39. Shea-Rohwer LE, Martin JE (2007) Luminescence decay of broadband emission from CdS quantum dots. J Lumin 127:499–507

Reappraising the Luminescence Lifetime Distributions in Silicon Nanocrystals

Supporting Information

Basic characterization – IR and XPS spectroscopy

The IR spectra provide a first check of the functionalization process. Both spectra show the characteristic C-H stretching mode around 2800-3000 cm^{-1} as well as Si-H bonds at 2100 cm^{-1} and Si-O-Si around 1065 cm^{-1}. The higher intensity of Si-O-Si to CH_3 bonds for the smaller particle size indicates higher surface oxidation compared to the larger SiNCs. Generally, it can be seen that the hydrosylilation reaction is not yielding a full surface coverage, as there is some remaining Si-H bonds visible.

Fourier transform infrared spectroscopy (FTIR) was performed in a Nicolet 8700 from Thermo Scientific.

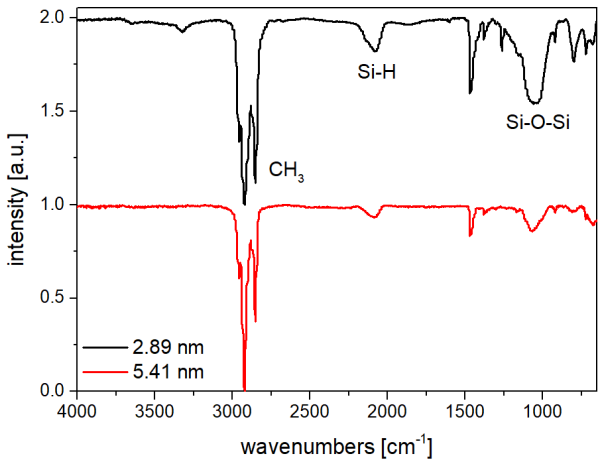

Figure S1 Normalized FTIR spectra of the synthesized SiNCs. The IR spectra and thus the surface composition is similar. However, it can be seen that the small SiNCs are more oxidized than the large particles (higher ratio of silicon oxide to CH_3 bands).

To gain further insight about the degree of oxidation, XPS spectra were taken. In the following, high resolution XPS spectra for the different samples are shown. The small SiNCs show a higher ratio of oxide species compared to the large SiNCs further approving the result from FTIR. The oxide species are very likely produced during the synthesis process, as some

steps cannot be done under inert atmosphere (e.g. HF etching with subsequent particle separation).

X-ray photo-electron spectroscopy was measured in a SPECS system equipped with a Phoibos 150 2D CCD hemispherical analyzer and a Focus 500 monochromator. The detector angle was set perpendicular to the surface and the X-ray source was Mg Kα.

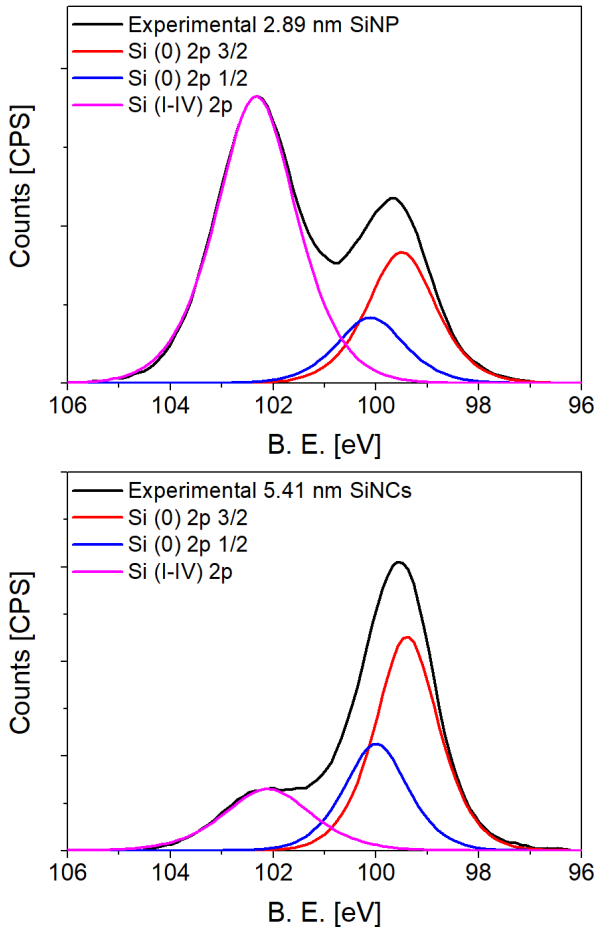

Figure S2 XPS spectra for the Si 2p orbital of the investigated particles. The ratio of oxide species to elemental silicon is considerably smaller for the large SiNCs. The XPS spectra were referenced to the Carbon C1s peak at 284.8 eV.

Excitation power dependency of the PL intensity and measured lifetime

As stated in the main article, the number of excitations per NC ~1 for the larger NCs suggests that one may be in the over-excitation regime in which there are additional non-radiative effects, due to the presence of multi-excitons on some NCs. In order to further evaluate this possibility, the lifetime was measured as a function of excitation power, resulting in Fig. S3 and Table S1. Though showing a saturation behavior in the PL intensities with increasing

excitation power, the obtained values of τ and β remain unaffected within the experimental error of 2.1%.

Due to low intensities for small excitation power the Hamamatsu h7422-50 photomultiplier tube interfaced to a Becker-Hickl PMS400 multiscalar was used, which is the reason for the measured lifetimes appearing longer than in the main article.

The 352 nm Ar^+ ion laser beam was pulsed (50% duty cycle, 100 Hz) using an Isomet IMDD-T110L-1.5 acousto-optic modulator (AOM) with a fall time of ~50 ns.

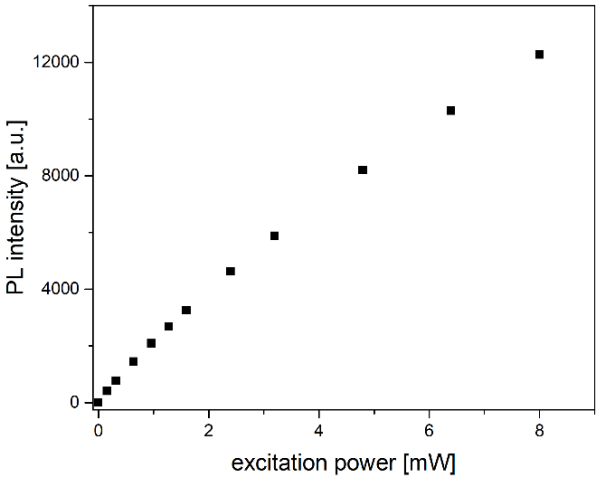

Fig. S3: PL intensity plotted against the excitation power for the large SiNCs. An 352 nm Ar+ ion laser beam was used to excite the sample.

Table S1. Excitation power dependence of the SiNCs fitting parameters obtained from Eq. 4. The decay time τ and the stretching factor β remains almost the same within the used excitation powers.

excitation power [mW]	τ [µs]	β [a.u.]
0.16	290.43	0.959
0.32	291.62	0.959
0.64	291.41	0.959
0.96	292.45	0.960
1.28	296.10	0.958
1.60	295.18	0.957
2.40	294.24	0.958
3.20	296.86	0.957
4.80	293.89	0.959
6.40	293.26	0.958
8.00	291.84	0.958

6.3 Ensemble effects in the temperature-dependent photoluminescence of silicon nanocrystals

Matthias Jakob[a], Morteza Javadi[b], Jonathan G. C. Veinot[b], Al Meldrum[c], Aras Kartouzian*[a] and Ulrich Heiz[a]

[a] Matthias Jakob, Aras Kartouzian, Ulrich Kaspar Heiz
Chair of Physical Chemistry
Technical University of Munich
Lichtenbergstrasse 4. 85748 Garching, Germany

[b] Morteza Javadi, Jonathan. G. C. Veinot
Department of Chemistry
University of Alberta
T6G 2R3 Edmonton, Alberta, Canada

[c] Al Meldrum
Department of Physics
University of Alberta
T6G 2E1 Edmonton, Alberta, Canada

* corresponding author, E-mail: aras.kartouzian@tum.de

Reproduced from *Chem. Eur. J.*, **2019**, *25*, 3061-3067 with permission from John Wiley and Sons.

ChemPubSoc Europe

DOI: 10.1002/chem.201804986

CHEMISTRY A European Journal Full Paper

Silicon Nanocrystals

Ensemble Effects in the Temperature-Dependent Photoluminescence of Silicon Nanocrystals

Matthias Jakob,[a] Morteza Javadi,[b] Jonathan G. C. Veinot,[b] Al Meldrum,[c] Aras Kartouzian,*[a] and Ulrich Heiz[a]

Abstract: In this work the temperature-dependent photoluminescence of alkyl-capped silicon nanocrystals with mean diameters of between 3 and 9 nm has been investigated. The nanocrystals were characterized extensively by FTIR, TEM, powder XRD, and X-ray photoelectron spectroscopy prior to low-temperature and time-resolved photoluminescence spectroscopy experiments. The photoluminescence (PL) properties were evaluated in the temperature range of 41–300 K. We found that the well-known temperature-dependent blueshift of the PL maximum decreases with increasing nanocrystal diameter and eventually becomes a redshift for nanocrystal diameters larger than 6 nm. This implies that the observed shifts cannot be explained solely by band-gap widening, as is commonly assumed. We propose that the luminescence of drop-cast silicon nanocrystals is affected by particle ensemble effects, which can explain the otherwise surprising temperature dependence of the luminescence peak.

Introduction

Semiconductors play an important role in technological products and therefore in our daily life.[1,2] Recent advances in high-tech products have often been due to developments in nanotechnology. Semiconductor nanoparticles in particular present many attractive features for light-emission applications.[3,4] On the one hand, the physical and optical properties of semiconductor nanoparticles make them promising candidates for future applications in electronic devices,[5–7] for example, in quantum dot display technology.[8] On the other hand, there is also an increasing demand to reduce the amount of heavy metals in electronic devices.[9] This limits the use of the well-established high-performance CdSe nanoparticles,[8] and therefore the demand for less toxic materials is rising.

Silicon is a preferred candidate, because it is biocompatible, abundant, and already used in computer technology and solar cells, and is therefore comparatively well understood.[10,11] Accordingly, silicon nanomaterials have received considerable attention, mainly due to the tunability of their light emission properties through the control of their size and functionalization.[12–14] Furthermore, medical applications such as fluorescence and magnetic resonance imaging have recently been demonstrated.[15,16] For the commercial use of silicon nanomaterials to be realized, a complete understanding of their behavior and properties as well as the ability to control them reliably are essential.[17–19] Thus, a manifold of different studies have been performed on silicon nanomaterials, including studies on size-dependent emission,[19–21] low-temperature effects,[22–26] particle interactions,[27–30] and the influence of functionalization or oxidation.[24,31–34] We present herein a low-temperature study of functionalized silicon nanocrystals (SiNCs) that extends the so-far measured size range up to 9 nm SiNCs. The surprising temperature-dependence of these large SiNC solids leads us to ensemble effects in non-monodisperse nanoparticle samples. Ensemble effects have scarcely been considered, but may alter the emission properties of nanomaterials.[28,35,36] We hope these effects are considered more often, as this may help to improve the understanding of silicon nanomaterials and create new materials that exploit or prevent the found effects.

[a] M. Jakob, A. Kartouzian, U. Heiz
Chair of Physical Chemistry, Technical University of Munich
Lichtenbergstrasse 4, 85748 Garching (Germany)
E-mail: aras.kartouzian@tum.de

[b] M. Javadi, J. G. C. Veinot
Department of Chemistry, University of Alberta
T6G 2R3 Edmonton, Alberta (Canada)

[c] A. Meldrum
Department of Physics, University of Alberta
T6G 2E1 Edmonton, Alberta (Canada)

Supporting information and the ORCID identification number(s) for the author(s) of this article can be found under: https://doi.org/10.1002/chem.201804986.

Results and Discussion

Characterization

The synthetic method employed (see the Experimental Section) produced dodecyl-capped SiNCs with well-defined diameters. Table 1 shows the resulting average particle diameters, determined by fitting the size distributions obtained by bright-field transmission electron microscopy (TEM) analysis (see the Supporting Information). A Gaussian distribution function was used to fit the obtained particle distributions.

To investigate the surface compositions of the different nanocrystals, FTIR spectra were recorded (Figure 1). All the

ChemPubSoc Europe

CHEMISTRY A European Journal Full Paper

Table 1. Annealing temperatures and resulting nanoparticle diameters determined by bright-field TEM. Errors are represented by the standard deviation of the Gaussian fit.

Annealing temperature [°C]	Particle diameter [nm]
1100	2.92 ± 0.53
1150	3.89 ± 0.67
1200	5.49 ± 1.15
1250	7.19 ± 1.05
1300	8.67 ± 1.23

Table 2. Ratio of silicon oxides to elemental silicon determined by XPS.[a]

Particle diameter [nm]	Ratio SiO_x/Si
2.92	2.03
3.89	1.04
5.49	0.31
7.19	0.07
8.67	0.08

[a] The spectra were internally referenced to adventitious carbon at 284.8 eV.

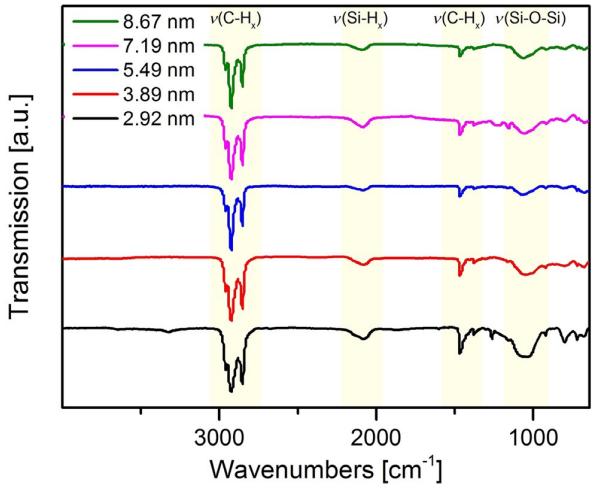

Figure 1. FTIR spectra of the synthesized SiNCs show a similar surface composition.

nanocrystals show characteristic C–H bands at around 2800–3000 and 1500 cm^{-1}, an Si–H band at 2100 cm^{-1}, and Si–O–Si bands at around 1065 cm^{-1}.[37,38] Radical-initiated hydrosilylation is known to provide only partial surface coverage, which is indicated by the presence of Si–H and Si–O–Si bands.[37] The higher intensity ratio of the Si–O–Si to the C–H band for the two smallest nanocrystal diameters indicates a larger amount of surface oxidation. Nevertheless, a similar overall surface composition is present in all samples. To verify that the prepared nanocrystals are composed of elemental silicon and to quantify the degree of oxidation, the samples were analyzed by X-ray photoelectron spectroscopy (XPS; see the Supporting Information). Although all the samples showed the Si 2p peak for elemental silicon (99.4 eV), it is apparent that the smallest SiNC ensembles are more oxidized than the larger samples (Table 2). Note that the amount of oxides in the two largest particle ensembles may be overestimated, as the information depth of XPS in silicon is approximately 2.5 nm, and thus particles with diameters larger then around 5 nm are not fully probed.

Low-temperature PL and time-resolved spectroscopy

The SiNCs were drop cast onto a silicon wafer and low-temperature PL spectroscopy was performed on the solid SiNC films. Figure 2 shows the temperature-dependent spectra for the smallest (2.92 nm) and largest (8.67 nm) nanocrystals. The temperature-dependent PL spectra for all the samples are included in the Supporting Information. Figure 3 shows the fitted temperature-dependent peak positions and relative peak shifts for all the investigated samples. Despite showing a higher PL maximum and integrated intensity upon cooling, the investigated samples behaved quite differently. SiNCs with an average diameter of 2.92, 3.89, and 5.49 nm showed a blueshift of their emission maxima at lower temperatures, whereas a redshift was observed for the SiNCs with diameters of 7.19 and 8.67 nm. This temperature-dependent behavior cannot be explained solely by band-gap widening and a series of experiments was thus performed to obtain more insight.

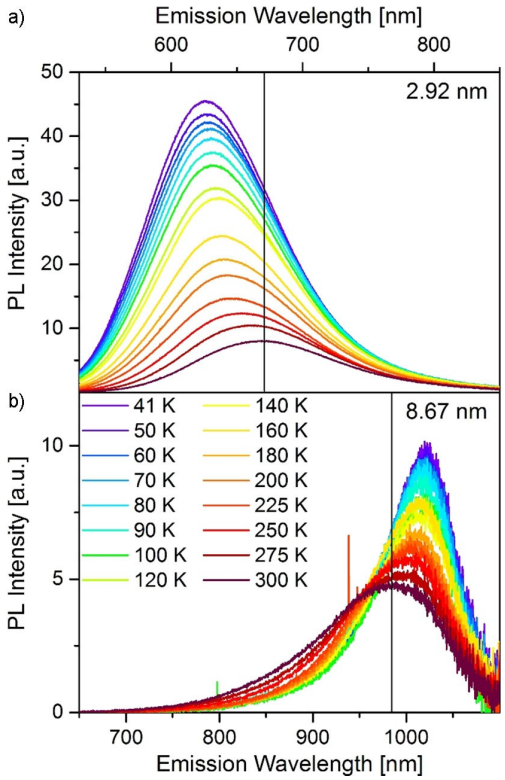

Figure 2. Temperature-dependent PL of the smallest and largest investigated SiNCs. The black line marks the PL peak position at 300 K.

ChemPubSoc Europe

CHEMISTRY A European Journal Full Paper

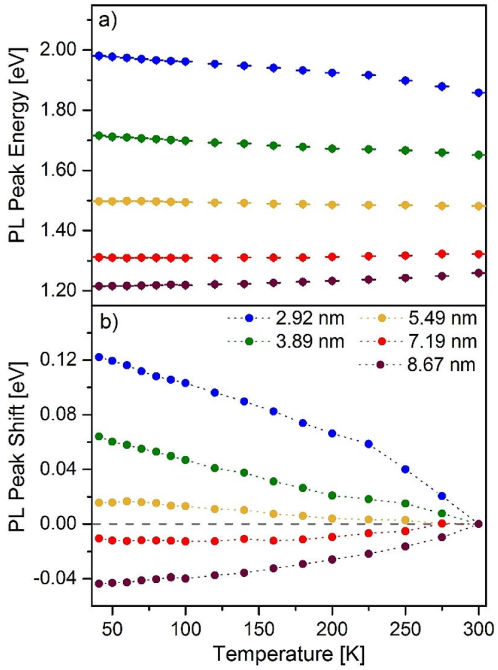

Figure 3. a) Temperature-dependent PL peak positions of the samples. Error bars display the standard deviation of the peak energy, determined from three measurements each. b) Peak positions normalized to the value at 300 K (shown by the dashed line), to more clearly display the change in emission energy upon cooling.

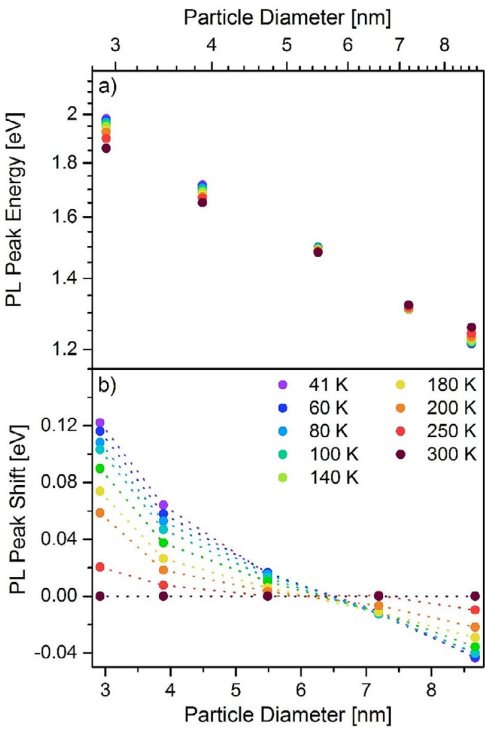

Figure 4. a) Size-dependent PL peak positions at selected temperatures. b) Size-dependent PL peak shifts relative to the peak energy at 300 K at selected temperatures. The value of the peak PL energy at 300 K was subtracted from the other data points for each SiNC ensemble.

The peak PL energy can also be displayed as a function of particle diameter for different temperatures and is displayed as a double logarithmic plot in Figure 4a. It is apparent that a linear dependence on the particle diameter exists for each temperature in the double logarithmic plot, which indicates that the observed temperature- and size-dependent peak PL energy can be fitted by a power function for each applied temperature (see the Supporting Information). To visualize the size-dependent PL peak shift, it has been plotted relative to the corresponding peak position at 300 K in Figure 4b. The data points converge at a diameter of around 6.4 nm, which implies that a SiNC ensemble with an average diameter of around 6.4 nm should not show any temperature dependence of its PL peak position. As temperature independence is physically unlikely, we conclude that beyond band-gap widening at least one additional temperature-dependent effect must be present and that these effects compensate each other at this particular particle diameter.

To obtain further information on the observed phenomena, temperature-dependent time-resolved PL (TRPL) spectroscopy was performed. The resulting mean decay times are shown in Figure 5a as absolute values and in Figure 5b as relative values normalized to the value at 300 K. The raw decays, model fits, and obtained fitting parameters are given in the Supporting Information. In general, the mean decay time was longer for larger particles, which is known from the literature and attributed to the loss of confinement with increasing diameter.[39,40] In addition, the effect of temperature on the

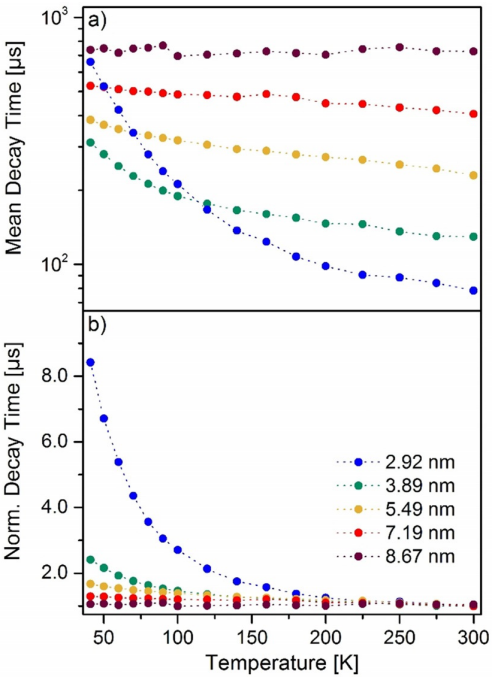

Figure 5. a) Calculated temperature-dependent mean decay times. The relative error in the time-resolved measurements was determined from three measurements at 41, 140, and 300 K each and was below 1% for all measurements. b) Mean decay times normalized to the value at 300 K.

ChemPubSoc Europe

CHEMISTRY A European Journal Full Paper

decay dynamics was more pronounced for ensembles with a smaller average particle diameter, which is also consistent with previous reports.[24,41] This behavior could be caused by the increased oxidation of the smaller particles. Similar temperature-dependent behavior was shown by Sinelnikov et al. They investigated the effect of surface functionalization on PL properties and more oxidized 5 nm SiNCs showed a larger increase in decay time and a larger blueshift of the PL peak at low temperatures than less oxidized samples.[24] This suggests that there are more nonradiative decay pathways (e.g., defects and surface states) within the small nanocrystals and that these nonradiative channels are quenched at lower temperatures.[42] This is also in good agreement with the observation of smaller quantum yields (QYs) for smaller SiNCs (see the Supporting Information).

The decay dynamics were then compared on wavelength-selected data for 2.92 and 5.49 nm SiNCs. These samples were chosen because they behave differently, and because their signal intensity was high enough to conduct monochromatic TRPL spectroscopy (see the Experimental Section). The temperature- and wavelength-dependent mean decay times are shown in Figure 6a,b for the 2.92 and 5.49 nm SiNCs, respectively. The resulting fitting parameters are shown in Tables S3 and S4 in the Supporting Information. It can be seen that smaller emission wavelengths and thus smaller SiNCs within one ensemble are more dependent on temperature than larger ones. This is similar to the overall trend shown in Figure 5. For example, when comparing the 750 nm emission wavelength for both samples (Figure 6) it is apparent that upon cooling the decay time becomes three times larger in the case of the 2.92 nm SiNCs, whereas the increase for the 5.49 nm SiNCs is approximately a factor of 1.3. Thus, the particle fractions within the 5.49 nm ensemble are hardly temperature-dependent and behave very similarly, whereas there are large differences within the 2.92 nm ensemble. This can help to explain the larger than expected blueshift in SiNC ensembles with small average particle size. It was also found by Hartel et al. that larger NCs have a longer PL lifetime and a higher absorption cross-section. Thus, the larger NCs within the population may saturate first, effectively causing a blueshift of the PL spectrum.[23] An illustration of how stronger PL enhancement of the smaller particle fractions can lead to an additional blueshift is depicted in Figure 7.NCs

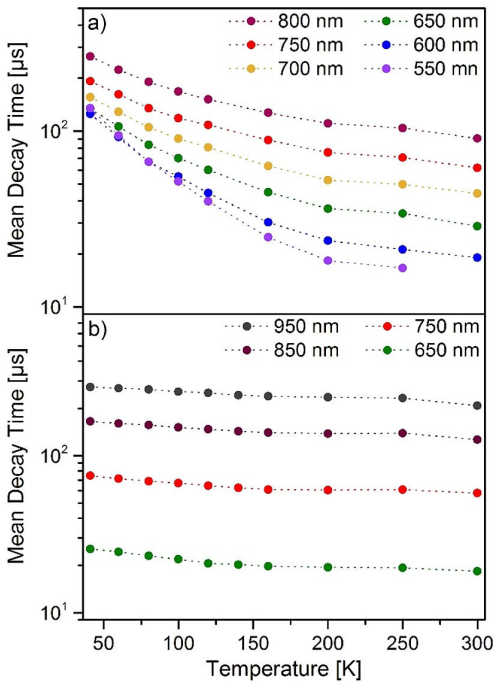

Figure 6. a) Temperature-dependent mean decay times of monochromatic emission wavelengths for the 2.92 nm particles. b) Temperature-dependent mean decay times of monochromatic emission wavelengths for the 5.49 nm particles. The error in the time-resolved monochromatic measurements was determined from sets of three measurements at different temperatures and wavelengths and was always below 4%.

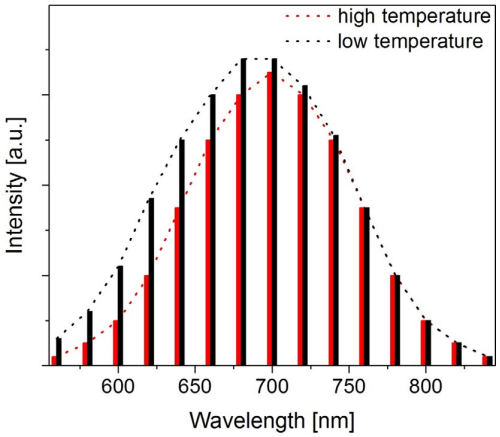

Figure 7. Illustration based on the findings from Figure 6. An ensemble of small SiNCs shows a different temperature dependence for different emission energies, which correspond to different sample fractions. This may lead to a blueshift of the PL peak position.

To summarize, small SiNCs (i.e., diameter <6.4 nm) showed a blueshift of the PL peak position and a distinct increase in mean decay time upon cooling. The effect of temperature on the PL peak position decreased continuously with increasing nanocrystal diameter, finally becoming a redshift for the ensembles of the largest SiNCs (i.e., diameter >6.4 nm). The effect of temperature on the mean decay time also decreased continuously with increasing nanocrystal diameter. We conclude that the first of the two earlier proposed effects is a combination of band-gap widening and a more pronounced PL enhancement of the smaller SiNCs within an ensemble, which causes an effective spectral blueshift as a function of decreasing temperature.

Nevertheless, the temperature-dependent redshift of the PL maxima for ensembles with an average SiNC diameter larger than 6 nm is still unexplained. A closer look at Figure 2 reveals that for the 2.92 nm SiNCs, the increase in PL intensity as a function of decreasing temperature is evident over the entire wavelength range and only the peak position changes (Fig-

ChemPubSoc Europe

CHEMISTRY A European Journal Full Paper

ure 2a). In contrast, the 8.67 nm SiNCs show a decrease in PL intensity in the range 700–950 nm and an increase in intensity between 950 and 1100 nm upon cooling (Figure 2b). We deduce that radiative or Förster resonance energy transfer (FRET) may happen between the small and large particles within the investigated SiNC ensembles. We then compared the samples in dispersed and drop-cast form (Figure 8). It can

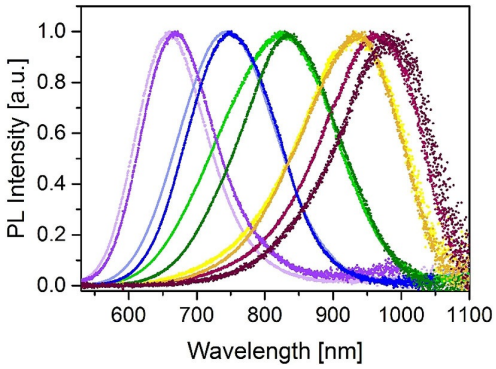

Figure 8. Photoluminescence spectra at 300 K for the SiNC samples in solution (bright) and drop cast onto a silicon wafer piece (dark). The samples are color-coded as follows: Purple: 2.92 nm, blue: 3.89 nm, green: 5.49 nm, gold: 7.29 nm, and dark red: 8.67 nm.

be seen that all the samples undergo a redshift or at least a decrease in intensity on the high-energy side of the PL spectrum upon drop casting. This is an indication that interparticle energy transfer may indeed happen within the samples in drop-cast form. The Förster distance R_0 for semiconductor nanoparticles is estimated to be around 5 nm, although no specific value for R_0 between SiNCs is available.[43,44] Based on the chain length of dodecane (ca. 1.5 nm), we estimate the maximum interparticle distance to be around 3 nm, assuming there is no ligand intercalation but densely packed layers. This is well below the R_0 value of 5 nm and therefore in principle FRET should be possible.

Recently, a redshift in emission upon drop casting was attributed to energy transfer within silicon nanocrystal solids by Furuta et al.[30] They investigated inorganic SiNCs without organic ligands to avoid distance effects and were able to demonstrate FRET within their samples. Therefore, the same experiment was performed on two of the samples investigated herein, which yielded similar results. The wavelength-selected measurements of the 2.92 and 5.49 nm SiNCs in solution and drop-cast form are shown in Figure 9. The difference in decay rate increases as a function of increasing emission energy, which is evidence for quenching processes on the high-energy side. Simple emission and re-absorption of emitted photons does not affect the PL lifetime, whereas FRET is usually accompanied by the shortening of the donor lifetimes.[30]

We conclude, therefore, that energy transfer may happen within our samples also, although the observed increase in decay rate is much smaller than that found by Furuta et al.[30] This can be attributed to a larger interparticle distance, caused

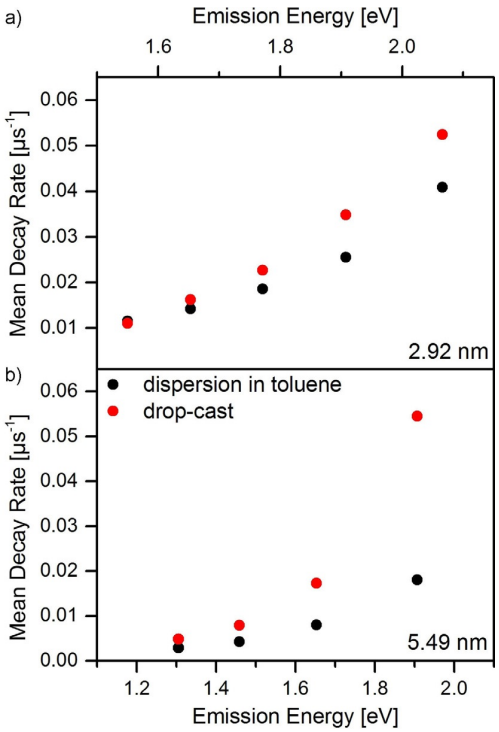

Figure 9. a) Mean decay rates at 300 K for the 2.92 nm SiNCs in dispersion and drop-cast forms. b) Mean decay rates at 300 K for the 5.49 nm SiNCs in dispersion and drop-cast forms. The significantly shortened decay times at low emission wavelengths indicate energy transfer within the drop-cast samples. The error in the time-resolved monochromatic measurements was determined from sets of three measurements and was always below 4%.

by the presence of the organic ligand shell. Furthermore, energy transfer seems to be less pronounced within the 2.92 nm SiNC ensemble, as the differences in decay rate between the dispersed and drop-cast forms are smaller than in the case of the 5.49 nm SiNC ensemble. Energy transfer was also cited as an effect present in luminescent NP ensembles by other groups,[30,45,46] and it was shown by Bose et al. that energy transfer in quantum dot solids can be more efficient when decreasing the temperature.[47] These findings are all consistent with our observations and might explain the surprising temperature dependence of the large SiNC ensembles.

Thus, we have shown that band-gap widening, which is commonly assumed to play the main role in the low-temperature PL of SiNCs, cannot solely explain the observed trends and we propose that a combination of band-gap widening, saturation effects, and energy transfer cause the trends observed in the samples investigated herein.

Conclusions

The PL of alkyl-capped SiNC solids with mean diameters of between 3 and 9 nm has been investigated for temperatures between 41 and 300 K. For SiNCs larger than 6 nm in diameter, which were neglected in most previous studies, an increasing redshift of the PL peak was observed upon cooling. This is con-

ChemPubSoc Europe

CHEMISTRY A European Journal Full Paper

trary to what would be expected from the phenomenon of band-gap widening. Furthermore, temperature-dependent TRPL spectroscopy revealed that the lengthening of the mean decay time upon cooling was more pronounced for smaller-sized SiNC fractions within an ensemble, leading to an additional blueshift of the PL peak. Thus, we conclude that the temperature-dependent shifts observed in the PL peak position of the SiNC ensembles are caused by several effects and not solely by band-gap widening. We propose a combination of band-gap widening (blueshift), size-dependent PL enhancement (blueshift), and size-dependent fluorescence energy transfer (redshift) to be responsible for the observed trends. These effects complicate the low-temperature PL study of SiNC ensembles and should be considered in future studies. Apart from that, knowledge and awareness of these effects could help to improve the manufacture of nanomaterials in this regard and be used in the development of applications, for example, photonic devices with temperature-independent emission.

Experimental Section

Synthesis and characterization

All reagents were used without further purification, unless stated otherwise. Hydrogen silsesquioxane (tradename FOx-17) was obtained from Dow Corning; the solvent was removed in vacuo and the resulting white solid was used without further purification. Electronic-grade hydrofluoric acid (HF, 49% aqueous solution) was purchased from J. T. Baker. 1-Dodecene (95%), methanol (reagent grade), ethanol (reagent grade), and toluene (HPLC grade) were obtained from Sigma–Aldrich. Toluene was dried by using a Grubbs-type solvent purification system (Innovative Technologies, Inc.).

The investigated SiNCs were synthesized according to the method of Dasog et al.[12] The first step in the nanocrystal synthesis involved the high-temperature treatment of hydrogen silsesquioxane (HSQ). HSQ (2 g) was heated in a zirconia furnace tube to the corresponding temperature at a heating rate of 8 °C min^{-1} and annealed for 1 h within a reducing atmosphere (5% H_2 and 95% Ar). The resulting black composite material was pre-ground in an agate mortar in ethanol. The powder suspension was then further ground by using a wrist-action shaker loaded with 5 mm glass beads for around 12 h. The fine powder was collected by vacuum filtration and dried. To release the particles, the brown powder (200 mg) was suspended in water (2 mL), ethanol (2 mL), and 49% aqueous HF (2 mL) and the mixture stirred for 40 min. The free-standing hydrogen-terminated particles were extracted with toluene, centrifuged at 3000 rpm for 10 min, and re-dispersed in dry toluene. The resulting yellow cloudy suspension was transferred to an oven-dried Schlenk flask filled with argon. After the addition of 1-dodecene (1 mL) and azobis(isobutyronitrile) (AIBN, 30 mg), the reaction mixture was subjected to three freeze-pump-thaw cycles to remove residual oxygen. The reaction mixture was then stirred for 24 h at 70 °C. After cooling to room temperature, pure ethanol (20 mL) was added, and the resulting suspension was centrifuged at 12000 rpm for 20 min. The particles were re-dispersed in toluene (10 mL). The precipitation and re-dispersion was repeated twice.

The particles were characterized by various techniques. FTIR spectra were recorded on a Nicolet 8700 spectrometer (Thermo Scientific). Bright-field transmission electron microscopy (TEM) images were recorded on a JEM-2010 instrument (JEOL) and evaluated by using ImageJ. Powder X-ray diffraction (pXRD) patterns were recorded on an Inel diffractometer equipped with a curved position-sensitive detector (CPS 120) using $Cu_{K\alpha}$ radiation. X-ray photoelectron spectroscopy (XPS) data were obtained on a SPECS system equipped with a Phoibos 150 2D CCD hemispherical analyzer and a Focus 500 monochromator. The detector angle was set perpendicular to the surface and the X-ray source was $Mg_{K\alpha}$.

Cryogenic PL setup

A helium cryostat from CTI Cryogenics was used. The samples were drop cast onto a clean silicon wafer with a 100 nm layer of SiO_2 (X18009 from Siegert Wafer), concentrated to a spot (ca. 2 mm^2), and mounted on a cooled copper block in a high-vacuum chamber. The base pressure of the setup was around 1×10^{-6} mbar. The measurements started at 41 K and the temperature was increased by means of a Cryo-con 32 temperature controller. PL spectra were measured with an Ocean Optics USB2000+ spectrometer in the wavelength range of 530–1100 nm. All the spectra were recorded in relative irradiance mode and an HL2000 tungsten halogen light source was used as calibrated radiation source. Time-resolved spectroscopy was performed with a Hamamatsu H7422-50 photomultiplier tube interfaced to a Becker–Hickl PMS400 multiscalar. The number of sweeps was set between 10000 and 300000 depending on the signal intensity. For the simultaneous wavelength- and temperature-dependent time-resolved measurements, the luminescence was directed through an Acton MS2500i monochromator prior to detection, with the half-width of the detected radiation set to around 3 nm. The 352 nm Ar^+ ion laser beam was pulsed (50% duty cycle, 50–1000 Hz) by using an Isomet IMDD-T110L-1.5 acousto-optic modulator (AOM) with a fall time of around 50 ns. The incident laser power was about 4 mW spread over an area of around 2 mm^2. To avoid laser light being detected, a 400 nm long-pass filter was used. The peak positions of the PL spectra were determined by fitting them with a skewed Gaussian function,[48] Equation (1):

$$I = Ae^{\left\{-\ln 2\left[\ln\left(1+\frac{2b(\lambda-\lambda_0)}{\sigma}\right)\frac{1}{b}\right]^2\right\}} \quad (1)$$

in which I, A, λ, λ_0, and b represent the PL intensity, amplitude, wavelength, peak wavelength and skewness, respectively. σ is related to the full width at half maximum by Equation (2):

$$\mathrm{FWHM} = \sigma\frac{\sinh b}{b} \quad (2)$$

To obtain comparable data from time-resolved fluorescence spectroscopy, the obtained luminescence decays have to be modeled and fitted. Recently, it was shown that different fit models lead to large differences in the determined mean decay times but give the same trend internally.[49] In this case the simple stretched exponential model, expressed by Equation (3), was used:

$$I_t = Ae^{-\left(\frac{t}{\tau_{SE}}\right)^{\beta}} + c \quad (3)$$

in which I_t, A, τ_{SE}, β, and c represent the time-dependent luminescence intensity, amplitude, stretched exponential time constant, stretching exponent ($0<\beta<1$), and constant offset, respectively.

The mean decay time $\langle t\rangle$ is then correctly calculated from[49] Equation (4) using the gamma function, Γ:

ChemPubSoc Europe

CHEMISTRY A European Journal Full Paper

$$\langle t \rangle = \tau_{SE} \frac{\Gamma(3/\beta)}{2\Gamma(2/\beta)} \quad (4)$$

Acknowledgements

This work was financially supported by the Deutsche Forschungsgemeinschaft (DFG) through the project Alberta/Technische Universität München Graduate School for Functional Hybrid Materials (ATUMS IRTG2022) and the project HE-3454/21-1. J.G.C.V. and A.M. acknowledge the continued generous funding from the Natural Sciences and Engineering Research Council of Canada (NSERC) Discovery Grant Program (RPGIN-2015-03893) and the NSERC CREATE-supported Alberta/Technical University of Munich International Graduate School for Hybrid Functional Materials (ATUMS, CREATE-463990-2015).

Conflict of interest

The authors declare no conflict of interest.

Keywords: ensemble effects · luminescence · nanocrystals · silicon · time-resolved spectroscopy

[1] S. M. Sze, M.-K. Lee, *Semiconductor Devices: Physics and Technology*, 3rd ed., Wiley, Hoboken, **2012**.
[2] Y. Furukawa, *Bull. Japan Inst. Met.* **1990**, *29*, 18 – 21.
[3] National Research Council, D. on E. and P. Sciences, C. for the R. of the N. N. Initiative, *Small Wonders, Endless Frontiers: A Review of the National Nanotechnology Initiative*, National Academies Press, Washington, **2002**.
[4] A. M. Bagher, *Sensors & Transducers* **2016**, *198*, 37 – 43.
[5] L. Zhuang, L. Guo, S. Y. Chou, *Appl. Phys. Lett.* **1998**, *72*, 1205 – 1207.
[6] M. Feng, K. L. Silverman, R. P. Mirin, S. T. Cundiff, *Opt. Express* **2010**, *18*, 13385 – 13395.
[7] C. Lin, C. Hung, P. Kuo, M. Cheng, *J. Disp. Technol.* **2010**, *8*, 681 – 683.
[8] H. Chen, J. He, S.-T. Wu, *IEEE J. Sel. Top. Quantum Electron.* **2017**, *23*, 1 – 1.
[9] EU Directive 2002/95/EC, Restriction of the Use of Certain Hazardous Substances in Electrical and Electronic Equipment, **2003**.
[10] S. De Wolf, A. Descoeudres, Z. C. Holman, C. Ballif, *Green Sustainable Chem.* **2012**, *2*, 7 – 24.
[11] S. E. Thompson, S. Parthasarathy, *Mater. Today* **2006**, *9*, 20 – 25.
[12] M. Dasog, J. Kehrle, B. Rieger, J. G. C. Veinot, *Angew. Chem. Int. Ed.* **2016**, *55*, 2322 – 2339; *Angew. Chem.* **2016**, *128*, 2366 – 2384.
[13] M. Dasog, G. B. De los Reyes, L. V. Titova, F. A. Hegmann, J. G. C. Veinot, *ACS Nano* **2014**, *8*, 9636 – 9648.
[14] L. Brus, *J. Phys. Chem.* **1994**, *98*, 3575 – 3581.
[15] J. H. Park, L. Gu, G. Von Maltzahn, E. Ruoslahti, S. N. Bhatia, M. J. Sailor, *Nat. Mater.* **2009**, *8*, 331 – 336.
[16] J. Aptekar, M. Cassidy, A. Johnson, R. Barton, M. Lee, A. Ogier, C. Vo, M. Anahtar, Y. Ren, S. Bhatia, C. Ramanathan, D. G. Cory, A. L. Hill, R. W. Mair, M. S. Rosen, R. L. Walsworth, C. M. Marcus, *ACS Nano* **2009**, *3*, 4003 – 4008.
[17] A. Sa'ar, *Phys. Status Solidi C* **2011**, *8*, 1764 – 1768.
[18] I. M. D. Höhlein, J. Kehrle, T. K. Purkait, J. G. C. Veinot, B. Rieger, *Nanoscale* **2014**, *6*, 914 – 918.
[19] G. Ledoux, O. Guillois, D. Porterat, C. Reynaud, F. Huisken, B. Kohn, V. Paillard, *Phys. Rev. B* **2000**, *62*, 15942 – 15951.
[20] C. Meier, A. Gondorf, S. Lüttjohann, A. Lorke, H. Wiggers, S. Lüttjohann, A. Lorke, H. Wiggers, *J. Appl. Phys.* **2007**, *101*, 103112.
[21] B. Delley, E. F. Steigmeier, *Appl. Phys. Lett.* **1995**, *67*, 2370.
[22] S. L. Brown, D. J. Vogel, J. B. Miller, T. M. Inerbaev, R. J. Anthony, U. R. Kortshagen, D. S. Kilin, E. K. Hobbie, *J. Phys. Chem. C* **2016**, *120*, 18909 – 18916.
[23] A. M. Hartel, S. Gutsch, D. Hiller, M. Zacharias, *Phys. Rev. B* **2012**, *85*, 165306.
[24] R. Sinelnikov, M. Dasog, J. Beamish, A. Meldrum, J. G. C. Veinot, *ACS Photonics* **2017**, *4*, 1920 – 1929.
[25] A. R. Van Sickle, J. B. Miller, C. Moore, R. J. Anthony, U. R. Kortshagen, E. K. Hobbie, *ACS Appl. Mater. Interfaces* **2013**, *5*, 4233 – 4238.
[26] G. Mauckner, K. Thonke, T. Baier, T. Walter, R. Sauer, *J. Appl. Phys.* **1994**, *75*, 4167 – 4170.
[27] J. Valenta, M. Greben, S. Gutsch, D. Hiller, M. Zacharias, *Appl. Phys. Lett.* **2014**, *105*, 243107.
[28] J. B. Miller, N. Dandu, K. A. Velizhanin, R. J. Anthony, U. R. Kortshagen, D. M. Kroll, S. Kilina, E. K. Hobbie, *ACS Nano* **2015**, *9*, 9772 – 9782.
[29] R. Limpens, A. Lesage, P. Stallinga, A. N. Poddubny, M. Fujii, T. Gregorkiewicz, *J. Phys. Chem. C* **2015**, *119*, 19565 – 19570.
[30] K. Furuta, M. Fujii, H. Sugimoto, K. Imakita, *J. Phys. Chem. Lett.* **2015**, *6*, 2761 – 2766.
[31] M. Dasog, Z. Yang, S. Regli, T. M. Atkins, A. Faramus, M. P. Singh, E. Muthuswamy, S. M. Kauzlarich, R. D. Tilley, J. G. C. Veinot, *ACS Nano* **2013**, *7*, 2676 – 2685.
[32] Y. Kanemitsu, *Phys. Rev. B Condens. Matter Mater. Phys.* **1996**, *53*, 13515 – 13520.
[33] S. Godefroo, M. Hayne, M. Jivanescu, A. Stesmans, M. Zacharias, O. I. Lebedev, G. Van Tendeloo, V. V. Moshchalkov, *Nat. Nanotechnol.* **2008**, *3*, 174 – 178.
[34] M. V. Wolkin, J. Jorne, P. M. Fauchet, G. Allan, C. Delerue, *Phys. Rev. Lett.* **1999**, *82*, 197 – 200.
[35] D. Nguyen, H. A. Nguyen, J. W. Lyding, M. Gruebele, *ACS Nano* **2017**, *11*, 6328 – 6335.
[36] N. Kholmicheva, P. Moroz, H. Eckard, G. Jensen, M. Zamkov, *ACS Energy Lett.* **2017**, *2*, 154 – 160.
[37] R. J. Clark, M. Aghajamali, C. M. Gonzalez, L. Hadidi, M. A. Islam, M. Javadi, M. H. Mobarok, T. K. Purkait, C. J. T. Robidillo, R. Sinelnikov, A. N. Thiessen, J. Washington, H. Yu, J. G. C. Veinot, *Chem. Mater.* **2017**, *29*, 80 – 89.
[38] I. M. D. Höhlein, A. Angı, R. Sinelnikov, J. G. C. Veinot, B. Rieger, *Chem. Eur. J.* **2015**, *21*, 2755 – 2758.
[39] C. Garcia, B. Garrido, P. Pellegrino, R. Ferre, J. A. Moreno, J. R. Morante, L. Pavesi, M. Cazzanelli, *Appl. Phys. Lett.* **2003**, *82*, 1595 – 1597.
[40] Y. Yu, G. Fan, A. Fermi, R. Mazzaro, V. Morandi, P. Ceroni, D.-M. Smilgies, B. A. Korgel, *J. Phys. Chem. C* **2017**, *121*, 23240 – 23248.
[41] F. Maier-Flaig, E. J. Henderson, S. Valouch, S. Klinkhammer, C. Kübel, G. A. Ozin, U. Lemmer, *Chem. Phys.* **2012**, *405*, 175 – 180.
[42] M. Nirmal, L. Brus, *Acc. Chem. Res.* **1999**, *32*, 407 – 414.
[43] A. L. Rogach, T. A. Klar, J. M. Lupton, A. Meijerink, J. Feldmann, *J. Mater. Chem.* **2009**, *19*, 1208 – 1221.
[44] S. Melle, O. G. Calderón, M. Laurenti, D. Mendez-Gonzalez, A. Egatz-Gomez, E. Lopez-Cabarcos, E. Cabrera-Granado, E. Diaz, J. Rubio-Retama, *J. Phys. Chem. C* **2018**, *122*, 18751.
[45] V. A. Belyakov, V. A. Burdov, R. Lockwood, A. Meldrum, *Adv. Opt. Technol.* **2008**, 279502.
[46] K. Chou, A. Dennis, *Sensors* **2015**, *15*, 13288 – 13325.
[47] R. Bose, J. F. McMillan, J. Gao, K. M. Rickey, C. J. Chen, D. V. Talapin, C. B. Murray, C. W. Wong, *Nano Lett.* **2008**, *8*, 2006 – 2011.
[48] P. F. Rusch, J. P. Lelieur, *Anal. Chem.* **1973**, *45*, 1541 – 1543.
[49] M. Jakob, A. Aissiou, W. Morrish, F. Marsiglio, M. Islam, A. Kartouzian, A. Meldrum, *Nanoscale Res. Lett.* **2018**, *13*, 383.

Manuscript received: October 2, 2018
Revised manuscript received: December 14, 2018
Accepted manuscript online: January 2, 2019
Version of record online: January 31, 2019

Supporting information

Characterization of the prepared Materials

To get information on the particle diameter bright field TEM images were recorded on a JEOL-2010 and evaluated with ImageJ. The size distributions were fit by a Gaussian distribution function to obtain a mean particle diameter. The errors are given as its standard deviation. The resulting size distributions are shown in Figure S1.

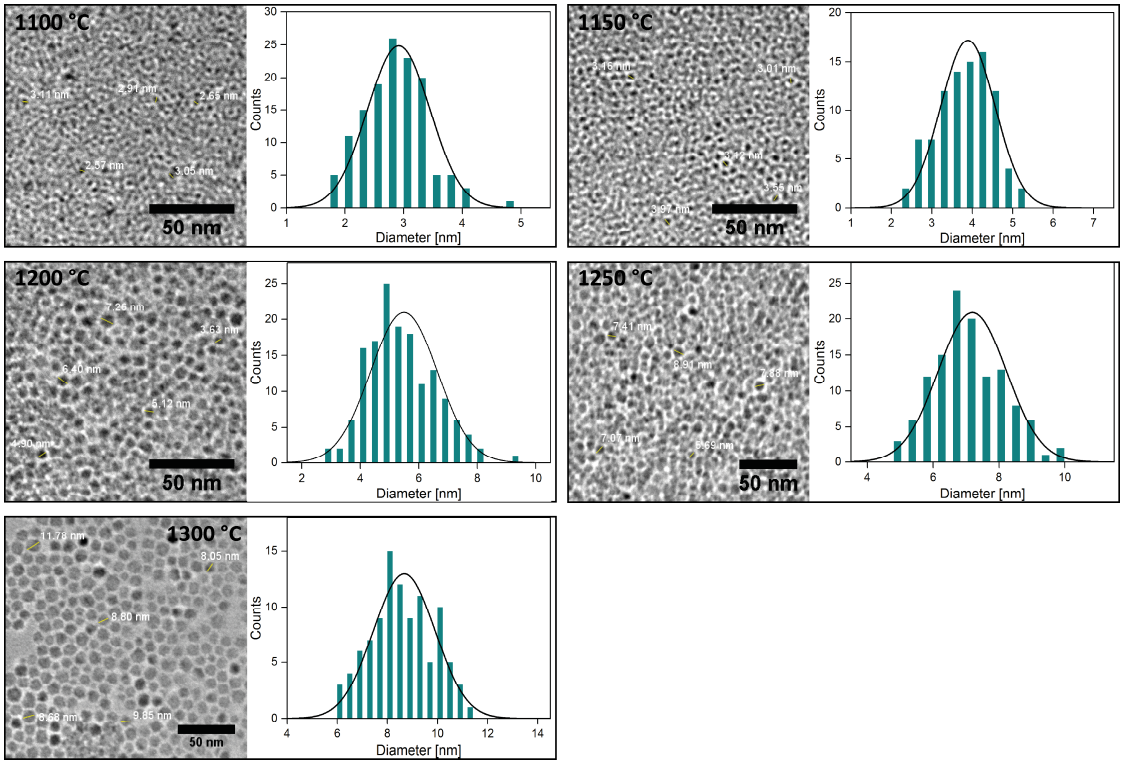

Figure S1: Exemplary bright-field TEM images of silicon nanocrystals and corresponding size distributions for different annealing temperatures. The average diameters are ranging from 3 to 9 nm. The size distributions are fit by a Gaussian distribution function (black line).

Table S1: Average diameters and dispersions obtained from brightfield TEM images by using a Gaussian fit and the simple arithmetic average.

Annealing Temperature [°C]	Gaussian Fit		Arithmetic Average	
	Diameter [nm]	Dispersion [nm]	Diameter [nm]	Dispersion [nm]
1100	2.915	± 0.534	2.886	± 0.474
1150	3.892	± 0.672	3.880	± 0.551
1200	5.492	± 1.151	5.408	± 1.046
1250	7.188	± 1.050	7.257	± 0.972
1300	8.670	± 1.232	8.638	± 1.038

In Figure S2 powder X-Ray diffraction (pXRD) spectra for the samples are depicted. It can be seen, that the crystallinity increases with increasing size, as the FWHM decreases. The estimated mean diameters using the Debye-Scherrer equation are 2.25, 2.72, 3.36, 4.53 and 5.1 nm respectively. A diffractometer from Inel equipped with a curved position sensitive detector was used. The applied radiation was Cu Kα.

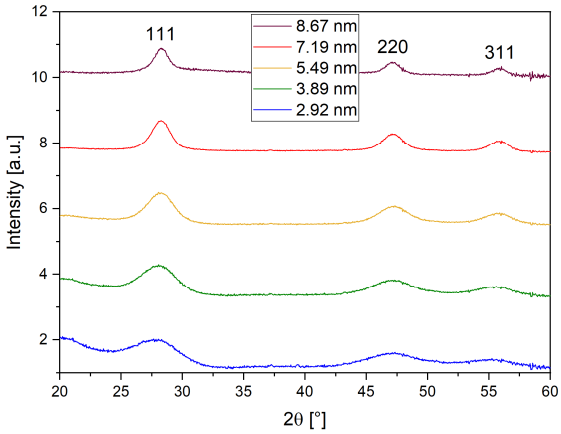

Figure S2: Powder XRD spectra for the investigated samples. The functionalized particles were drop casted directly onto the sample holder.

To gain further insight on the particle composition, XPS spectra were recorded. In Figure S3 high resolution XPS spectra for the prepared samples are shown. The two spin orbit couples of elemental silicon and of the different oxide species were fit separately. Si (IV) is not shown, as the fit was leading to a peak area of 0 for all samples. The small silicon nanocrystals show a higher ratio of oxide species compared to the large silicon nanocrystals further approving the qualitative result from FTIR. The oxide species are most probably introduced during the synthesis process, as some steps include ambient conditions (e.g. HF etching with subsequent particle separation). X-ray photoelectron spectroscopy was measured on a SPECS system equipped with a Phoibos 150 2D CCD hemispherical analyzer and a Focus 500 monochromator. The detector angle was set perpendicular to the surface and the X-ray source was Mg Kα.

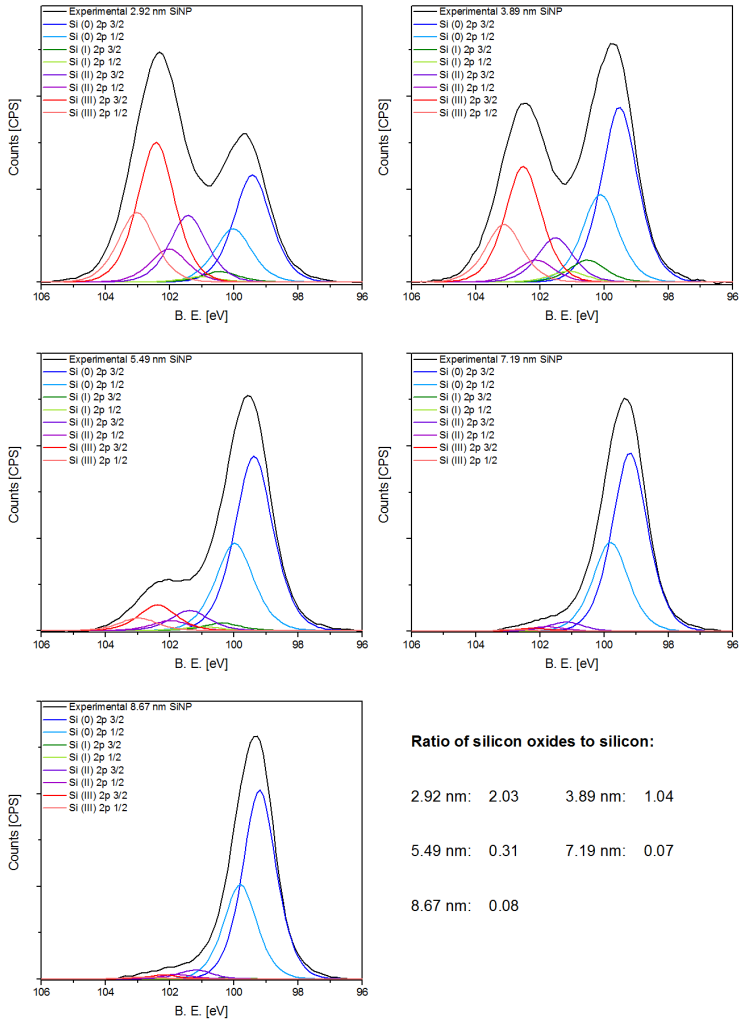

Figure S3: XPS analysis of the investigated particles. The ratio of silicon-oxides to elemental silicon is considerably smaller for the large SiNCs. All spectra were internally referenced to the carbon C 1s peak at 284.8 eV.

Low temperature fluorescence spectroscopy

Fluorescence and time-resolved fluorescence spectroscopy was performed for all samples at different temperatures ranging from 41 to 300 K. Figure S4 shows the raw photoluminescence spectra for the different samples. It its visible that the two smallest sized samples show a blue shift compared to room temperature (indicated by black line), the medium sized particles show no shift and the largest particles are shifting to the red. The biggest particles also show a narrower bandwidth at low temperatures. This may indicate that energy transfer is happening between the nanocrystals in this sample.

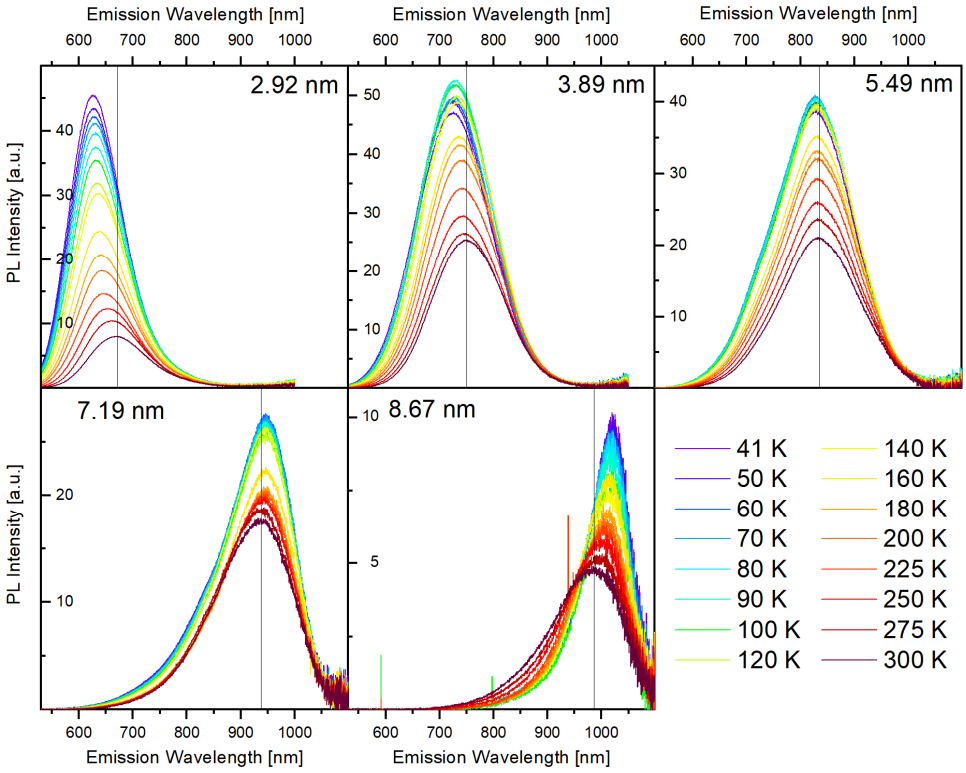

Figure S4: Temperature-dependent photoluminescence spectra for the different samples. A temperature dependence of intensity and spectral position is clearly visible. The black line marks the luminescence peak position at 300 K.

The peak PL energy can also be displayed as a function of the particle diameter for different temperatures and is displayed as a double logarithmic plot in Figure 4a. It is apparent that a linear dependence on the particle diameter exists for each temperature, which converts to a power function in a linear plot as follows:

$$\log(E_{PL}) = \log(a) + n \cdot \log(d) \;\rightarrow\; E_{PL} = a \cdot (d)^n \qquad (S1)$$

Where E_{PL}, a, n and d correspond to PL peak energy, a prefactor, the potency of the power function, and the particle diameter. This means that the peak PL energy can be fit by a certain power function for each temperature. The prefactor a and potency n appear to be linearly dependent on the ambient temperature, which in principal allows to extrapolate our data to lower and higher temperatures.

Table S2: Fit parameters obtained for fitting the size-dependent peak PL positions with a power function (Eq. S1).

Temperature (K)	a	n
41	3.18	-0.45
60	3.15	-0.44
80	3.12	-0.44
100	3.10	-0.43
140	3.05	-0.42
180	2.98	-0.41
200	2.95	-0.41
250	2.86	-0.39
300	2.72	-0.36

The fluorescence decay times are getting larger with increasing particle diameter, although the temperature dependency is getting smaller. Whereas the small particles show a much longer decay time at low temperatures, the large particles are almost unaffected. Normalized fluorescence decays are depicted in Figure S5. Exemplary stretched exponential fits are depicted in Figure S6. The stretched exponential function fits the decays well, although the fits for the 2.92 nm sample are less accurate than for the other samples. The obtained fit parameters are given in Table S3. It is remarkable that the stretching parameter β is decreasing (more stretched behavior) upon cooling for the 2.92 nm ensembles, whereas it is increasing for all other samples.

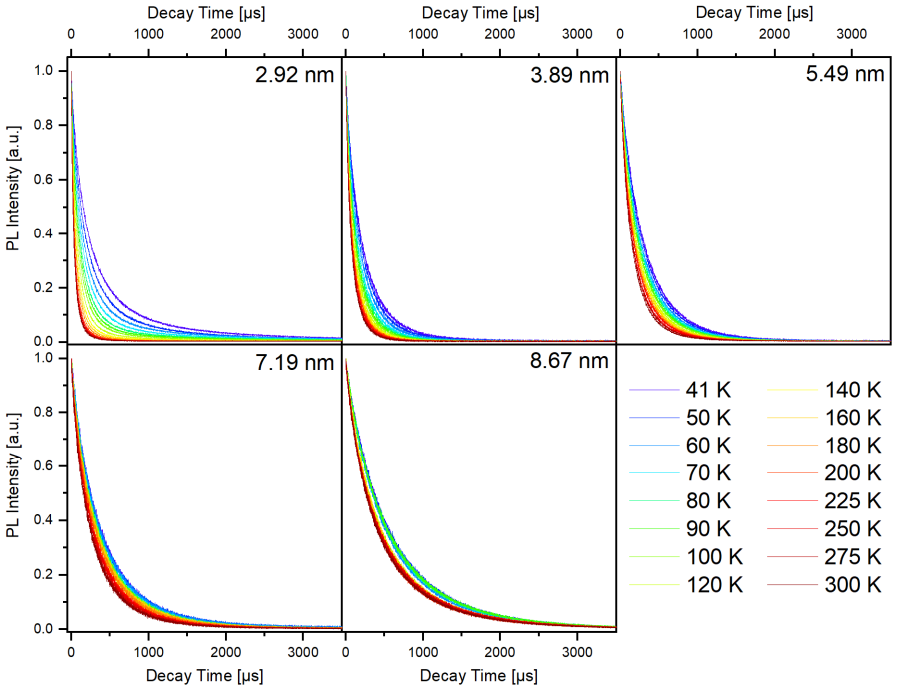

Figure S5: Temperature-dependent time-resolved photoluminescence decays for the different samples. The larger the particles get, the smaller is the temperature dependence on the lifetime. Larger particles are showing longer lifetimes in general.

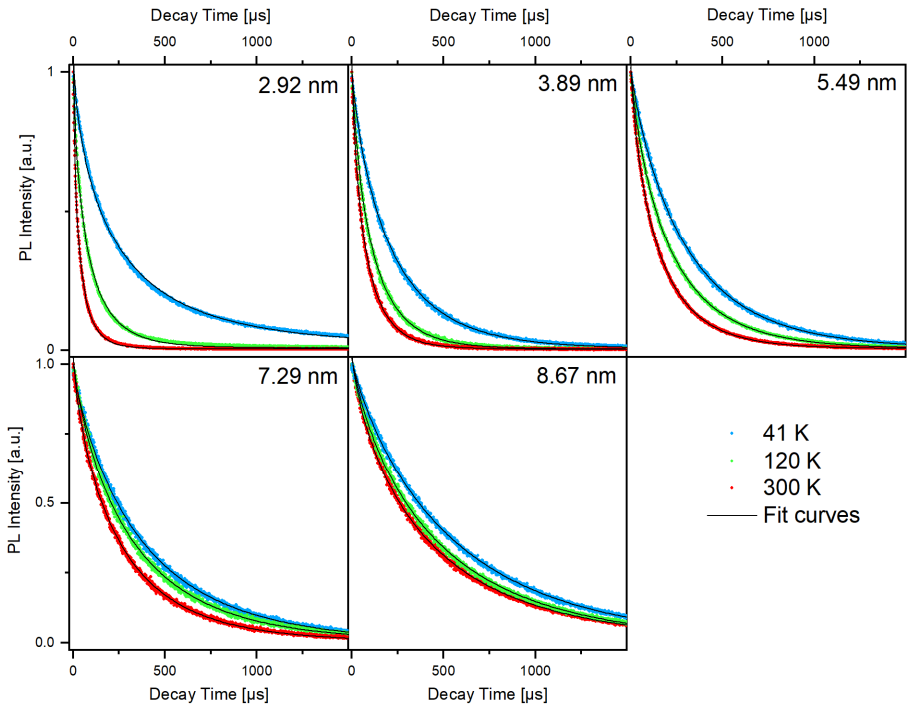

Figure S6: Selected temperature-dependent time-resolved photoluminescence decays for the different samples. The data points are fitted with a stretched exponential fit and the fit curves are depicted as black lines.

Table S3: The obtained stretched exponential fit parameters and mean decay times for all samples for the applied temperatures. β, τ and ⟨*t*⟩ represent the stretching exponent ($0 < \beta < 1$), the stretched exponential time constant and the calculated mean decay time (Eq. 4) respectively.

	2.92 nm			3.89 nm			5.49 nm			7.26 nm			8.67 nm		
Temperature [K]	β	τ	⟨*t*⟩	β	τ	⟨*t*⟩	β	τ	⟨*t*⟩	β	τ	⟨*t*⟩	β	τ	⟨*t*⟩
41	0.66	217	660	0.83	207	312	0.89	298	384	0.85	371	527	0.86	537	738
50	0.66	175	525	0.84	188	280	0.88	280	368	0.84	360	522	0.86	545	748
60	0.66	143	422	0.83	167	250	0.87	263	353	0.84	352	511	0.85	503	717
70	0.67	125	341	0.82	148	228	0.86	250	341	0.84	339	503	0.85	524	747
80	0.68	104	279	0.82	137	212	0.86	239	333	0.83	329	500	0.85	526	753
90	0.69	93	239	0.82	127	199	0.85	230	325	0.83	326	492	0.84	526	768
100	0.69	83	212	0.81	119	189	0.85	221	318	0.83	321	487	0.82	449	697
120	0.71	71	167	0.80	106	176	0.84	208	305	0.82	311	484	0.81	438	706
140	0.72	60	137	0.80	99	166	0.83	197	293	0.81	298	476	0.80	430	713
160	0.71	53	123	0.79	94	160	0.83	190	289	0.82	313	489	0.80	434	727
180	0.72	47	108	0.79	89	154	0.82	181	279	0.81	298	474	0.79	416	716
200	0.71	42	98	0.79	84	146	0.82	175	272	0.81	278	448	0.78	395	705
225	0.71	38	91	0.77	79	146	0.82	170	265	0.81	275	445	0.78	420	744
250	0.70	36	88	0.78	76	136	0.81	159	254	0.80	262	431	0.78	424	756
275	0.70	35	84	0.78	72	130	0.81	152	244	0.79	248	421	0.77	398	729
300	0.70	32	78	0.77	71	130	0.81	142	229	0.79	237	405	0.77	390	727

In Figure S7 exemplary monochromated and temperature-dependent TRPL is shown for the two investigated samples. The obtained fit parameters are given in Table S4 and S5.

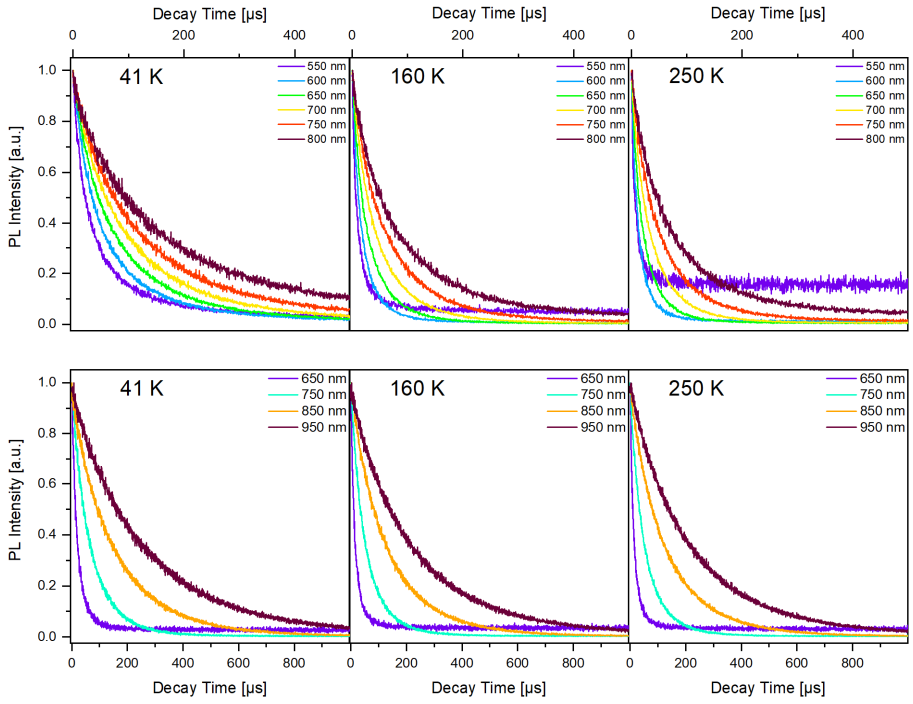

Figure S7: Selected monochromated and temperature-dependent TRPL decays for the 2.92 nm (top) and 5.49 nm (bottom) SiNCs.

Table S4: The obtained wavelength dependent stretched exponential fit parameters and mean decay times for the 2.92 nm SiNC at different temperatures. β, τ and ⟨*t*⟩ represent the stretching exponent (0 < β < 1), the stretched exponential time constant and the calculated mean decay time (Eq. 5) respectively.

2.92 nm SiNC																		
Temperature [K]	550 nm			600 nm			650 nm			700 nm			750 nm			800 nm		
	β	τ	⟨*t*⟩	β	τ	⟨*t*⟩	β	τ	⟨*t*⟩	β	τ	⟨*t*⟩	β	τ	⟨*t*⟩	β	τ	⟨*t*⟩
41	0.60	30	135	0.69	48	125	0.75	67	134	0.78	87	156	0.79	110	192	0.77	142	266
60	0.61	24	94	0.70	37	92	0.75	54	106	0.79	73	129	0.80	96	162	0.78	127	223
80	0.63	19	67	0.73	31	67	0.78	46	84	0.81	65	105	0.82	88	135	0.80	113	191
100	0.64	15	52	0.72	25	55	0.78	39	70	0.81	56	91	0.83	79	118	0.81	105	168
120	0.65	12	40	0.74	21	44	0.78	34	60	0.81	49	81	0.82	70	108	0.81	94	151
160	0.68	9	25	0.76	16	30	0.79	26	45	0.81	40	63	0.82	57	89	0.81	79	127
200	0.70	7	18	0.77	13	24	0.79	21	36	0.82	34	53	0.82	49	76	0.81	68	111
250	0.70	7	17	0.79	12	21	0.79	20	34	0.82	32	50	0.83	47	71	0.81	65	104
300	-	-	-	0.76	10	19	0.78	16	29	0.79	26	44	0.82	40	62	0.80	54	91

Table S5: The obtained wavelength dependent stretched exponential fit parameters and mean decay times for the 5.49 nm SiNC for the applied temperatures. β, τ and ⟨*t*⟩ represent the stretching exponent (0 < β < 1), the stretched exponential time constant and the calculated mean decay time (Eq. 5) respectively.

5.41 nm SiNC												
Temperature [K]	650 nm			750 nm			850 nm			950 nm		
	β	τ	⟨*t*⟩	β	τ	⟨*t*⟩	β	τ	⟨*t*⟩	β	τ	⟨*t*⟩
41	0.93	25	25	0.97	74	75	0.98	164	165	0.98	271	274
60	0.94	24	24	0.97	70	71	0.97	158	160	0.98	266	269
80	0.93	22	23	0.97	68	69	0.98	155	157	0.98	261	264
100	0.94	21	22	0.96	66	67	0.97	150	151	0.98	253	256
120	0.93	20	21	0.96	63	64	0.97	146	147	0.98	248	251
160	0.92	19	20	0.96	61	62	0.97	141	143	0.98	240	243
200	0.92	19	20	0.96	60	61	0.97	139	140	0.98	236	239
250	0.91	19	19	0.96	59	60	0.97	137	138	0.97	232	235
300	0.91	18	19	0.96	60	61	0.97	137	139	0.98	230	232
	0.90	17	18	0.95	56	58	0.97	125	127	0.97	205	208

The rise in PL intensity follows the trend of time-resolved spectroscopy in general and is depicted in Figure S8. The intensities were calculated by integrating the obtained spectra. The small particles show a greater dependence on temperature than the larger ones in general. The 3.89 and 5.49 nm sized ensembles show a saturation behavior around 90 K and the intensity is slightly dropping towards lower temperatures. The luminescence intensity drop for low temperatures might be an artifact of slight over-excitation, as has been previously reported in the literature.[1]

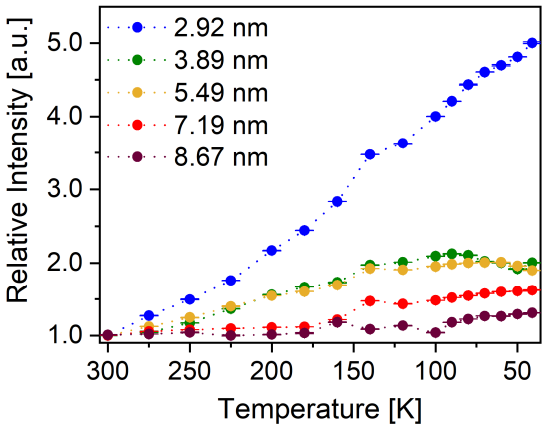

Figure S8: Temperature-dependent relative PL intensity of the investigated particle ensembles. Smaller particles show a larger dependency. Error-bars display the standard deviation of three measurements.

The quantum yield (QY) at room temperature was measured on drop casted samples. One can observe, that with increasing particle diameter also the quantum yield increases (Figure S9). It is hardly excitation wavelength dependent moreover. The largest particles could not be measured within this device as their emission is beyond the detection limit of the used detector.

External quantum yields were collected on a Quantaurus-QY quantum yield spectrometer from Hamamatsu equipped with an integrating sphere detector and a Xenon light excitation source.

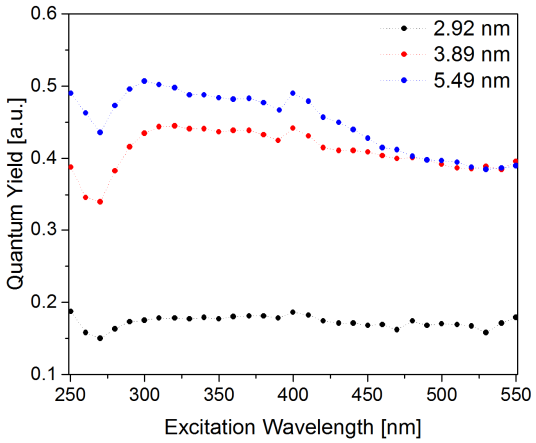

Figure S9: Excitation wavelength dependent quantum yield for the different samples. Larger SiNCs show a higher quantum yield.

In Figure S10 the raw fluorescence spectra for quantum yield calculation is shown. The visible spikes are internally corrected by a reference measurement. One can see that the emission of the large SiNCs is cut off by the detection limit of the device. Subsequently the QY is determined as too small.

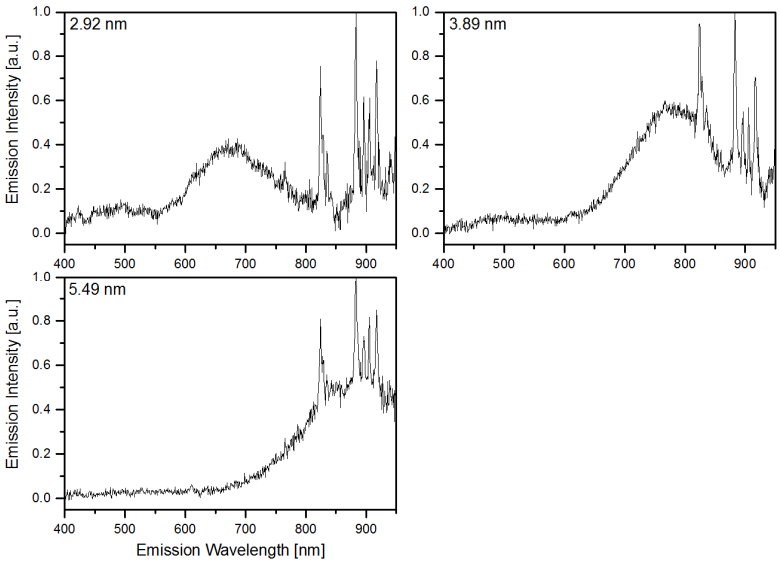

Figure S10: Photoluminescence spectra measured by Quantaurus QY. The quantum yield is determined from these spectra and the measured absorption.

In Figure S11 the photoluminescence decay curves of the 2.92 nm and 5.49 nm SiNCs in dispersed and drop-cast form at 300 K are displayed. It is apparent that the decay is quenched more strongly for short emission wavelengths as for long emission wavelengths. This indicates that energy transfer takes place between small and large SiNCs within the ensembles.

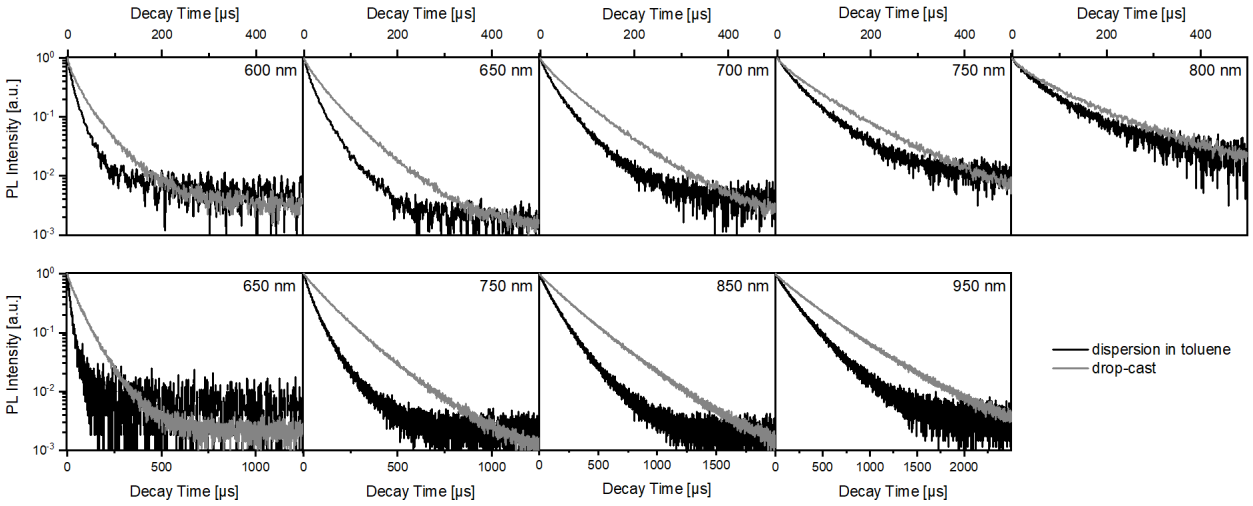

Figure S11: Top) Comparison between the monochromated TRS of the dissolved and drop-cast 2.92 nm SiNCs. Bottom) Comparison between the monochromated TRS of the dissolved and drop-cast 5.49 nm SiNCs.

In Table S6 the obtained fit parameters of the data sets in Fig S11 are shown. It appears that the relative difference between the decay times in solution and drop-cast is larger for larger SiNCs. We conclude, that energy transfer is more present within the large SiNCs, although it is taking place in both samples.

Table S6: The obtained wavelength dependent stretched exponential fit parameters and mean decay times for the 2.92 and 5.49 nm SiNCs as dispersion and drop-cast. β, τ and $\langle t \rangle$ represent the stretching exponent ($0 < \beta < 1$), the stretched exponential time constant and the calculated mean decay time (Eq. 5) respectively.

	2.92 nm						5.49 nm					
	dispersion in toluene			drop-cast			dispersion in toluene			drop-cast		
Wavelength [nm]	β	τ	$\langle t \rangle$	β	τ	$\langle t \rangle$	β	τ	$\langle t \rangle$	β	τ	$\langle t \rangle$
600	0.74	20.2	25	0.76	10	19	-	-	-	-	-	-
650	0.82	35.1	39	0.78	16	29	0.84	50	55	0.90	17	18
700	0.82	48.6	54	0.79	26	44	-	-	-	-	-	-
750	0.81	62.6	70	0.82	40	62	0.90	119	125	0.95	56	58
800	0.75	72.6	87	0.80	54	91	-	-	-	-	-	-
850	-	-	-	-	-	-	0.92	227	236	0.97	125	127
900	-	-	-	-	-	-	-	-	-	-	-	-
950	-	-	-	-	-	-	0.91	325	341	0.97	205	208

References

[1] A. M. Hartel, S. Gutsch, D. Hiller, M. Zacharias, *Phys. Rev. B - Condens. Matter Mater. Phys.*, **2012**, *85*, 1–5.

List of Publications

1. T. Lünskens, A. von Weber, **M. Jakob**, T. Lelaidier, A. Kartouzian and U. Heiz, Effect of Thiol-Ligands on the Optical Response of Supported Silver Clusters, *The Journal of Physical Chemistry C* **2017**, *121*, 9331-9336.
2. F. M. Hörmann, T. S. Chung, E. Rodriguez, **M. Jakob** and T. Bach, Evidence for Triplet Sensitization in the Visible-Light-Induced [2+2] Photocycloaddition of Eniminium Ions, *Angewandte Chemie International Edition* **2018**, *57*, 827-831.
3. A. Ozcelik, R. Pereira-Cameselle, A. von Weber, M. Paszkiewicz, M. Carlotti, T. Paintner, L. Zhang, T. Lin, Y.-Q. Zhang, J. V. Barth, T. van den Nobelen, R. C. Chiechi, **M. Jakob**, U. Heiz, S. Chiussi, A. Kartouzian and J. L. Alonso-Gómez, Device-Compatible Chiroptical Surfaces through Self-Assembly of Enantiopure Allenes, *Langmuir* **2018**, *34*, 4548-4553.
4. **M. Jakob**, A. von Weber, A. Kartouzian and U. Heiz, Chirality transfer from organic ligands to silver nanostructures via chiral polarisation of the electric field, *Physical Chemistry Chemical Physics* **2018**, *20*, 20347-20351.
5. **M. Jakob**, A. Aissiou, W. Morrish, F. Marsiglio, M. Islam, A. Kartouzian and A. Meldrum, Reappraising the Luminescence Lifetime Distributions in Silicon Nanocrystals, *Nanoscale Research Letters* **2018**, *13*, 383.
6. A. von Weber, **M. Jakob**, E. Kratzer, A. Kartouzian and U. Heiz, *In situ* second-harmonic generation circular dichroism with submonolayer sensitivity, *ChemPhysChem* **2019**, *20*, 134-141.
7. A. von Weber, D. C. Hooper, **M. Jakob**, V. K. Valev, A. Kartouzian and Prof. U. Heiz, Circular dichroism & isotropy - polarity Reversal of Ellipticity in molecular films of 1,1′-Bi-2-Naphtol, *ChemPhysChem* **2019**, *20*, 62-69.
8. **M. Jakob**, M. Javadi, J. G. C. Veinot, A. Meldrum, A. Kartouzian and U. Heiz, Ensemble effects in the temperature-dependent photoluminescence of silicon nanocrystals, *Chemistry – A European Journal* **2019**, *25*, 3061-3067.
9. A. von Weber, P. Stanley, **M. Jakob**, A. Kartouzian, U. Heiz, Tunable Induced Circular Dichroism in Thin Organic Films, *The Journal of Physical Chemistry C* **2019**, *Advance Article*.

List of Abbreviations

CD	circular dichroism
EDX	energy-dispersive X-ray
FRS	frequency-resolved spectroscopy
FTIR	Fourier-transform infrared
HSQ	hydrogen silsesquioxane
IR	infrared
LSPR	localized surface plasmon resonance
PMT	photomultiplier tube
PL	photoluminescence
QFRS	quadrature frequency-resolved spectroscopy
s-CRD	surface cavity ring-down
SEM	scanning electron microscopy
SHG	second harmonic generation
s-SHG	surface second harmonic generation
SiNCs	silicon nanocrystals
SPR	surface plasmon resonance
TEM	transmission electron microscopy
TRS	time-resolved spectroscopy
UHV	ultrahigh vacuum
UPW	ultrapure water
UV/VIS	ultraviolet/visible
XPS	X-ray photoelectron spectroscopy
p-XRD	X-ray powder diffraction

Acknowledgements

Foremost, I would like to thank Prof. Dr. Ulrich K. Heiz for the opportunity to spend my time in his research group during the last years. It was my pleasure to work in a group with such a scientific and at the same time enjoyable working atmosphere. I also appreciate the support of Dr. Aras Kartouzian, as he was always readily available to discuss ideas and help us in the lab with his profound knowledge. I liked the freedom to pursue own ideas and projects and I want thank Ueli and Aras for their trust in my work. I also would like to thank PD. Dr. Friedrich Esch, who attracted me to Physical Chemistry by his inspiring lectures and practical courses during the Chemistry Master's program.
I am also thankful, that I was chosen to be part of the ATUMS program, so that I was able to spend some of my time in Canadian research labs and also got the opportunity to explore this wonderful country. In this regards special thanks go to Prof. Jonathan G.C. Veinot and Prof. Al Meldrum, who warmly welcomed me to their labs and shared their knowledge about semiconductor nanomaterials.
I also wish to express my gratitude to my labmates and friends Alexander, Farinaz and Jörn, who provided the best working environment one could think of. I also thank all the other former and present group members for their readiness to help and the good atmosphere within the group. The mechanical and electronic workshops helped to keep our experimental setup in a good state and I want to thank them for their support. I also want to thank all my bachelor and internship students for their support and valuable work.
I sincerely thank my parents and family for their ongoing support, who were always encouraging me to give my best. I acknowledge my best friends who accompanied my life as long as I can think and I want to thank them all for creating so many opportunities to slow down and relax. Last but not least I thank my girlfriend for all the fantastic moments during the last years.

Bibliography

[1] D. G. Rickerby in *Sustainable Nanotechnology and the Environment: Advances and Achievements*, American Chemical Society, **2013**, pp. 91–105.

[2] M. Van de Voorde, B. Sels, *Nanotechnology in Catalysis*, (Eds.: M. Van de Voorde, B. Sels), Wiley-VCH Verlag GmbH & Co. KGaA, Weinheim, Germany, **2017**.

[3] I. Chorkendorff, J. W. Niemantsverdriet, *Concepts of Modern Catalysis and Kinetics - 2nd Edition*, Wiley-VCH Verlag GmbH & Co. KGaA, Weinheim, Germany, **2007**.

[4] E. Alonso, F. R. Field, R. E. Kirchain, *Environmental Science & Technology* **2012**, *46*, 12986–12993.

[5] P. J. Loferski, Z. T. Ghalayini, S. A. Singerling, *Minerals Yearbook vol. I - Platinum-Group Metals*, U.S. Geological Survey, **2018**.

[6] X. Qi, M. A. Biberger, U.S. Patent 9,156,025 B2: Three-Way Catalytic Converter Using Nanoparticles, **2015**.

[7] Statista. Estimated worldwide automobile production from 2000 to 2018 (in million vehicles). https://www.statista.com/statistics/262747/worldwide-automobile-production-since-2000/. Accessed March 12, 2019.

[8] J. A. Hubbell, A. Chilkoti, *Science* **2012**, *337*, 303–305.

[9] A. M. Bagher, *Sensors & Transducers* **2016**, *198*, 37–43.

[10] National Research Council, *Small Wonders, Endless Frontiers: A Review of the National Nanotechnology Initiative*, National Academies Press, Washington, **2002**.

[11] Y. Furukawa, *Bulletin of the Japan Institute of Metals* **1990**, *29*, 18–21.

[12] S. J. Russel, P. Norvig, *Artificial Intelligence : A Modern Approach*, Third Edit, Pearson Education Limited, Harlow, **2016**.

[13] M. Bohr, *IEEE Transactions On Nanotechnology* **2002**, *1*, 56–62.

[14] G. Tegart, *Foresight* **2004**, *6*, 364–370.

[15] H. Chen, J. He, S.-T. Wu, *IEEE Journal of Selected Topics in Quantum Electronics* **2017**, *23*, 1–11.

[16] C. N. R. Rao, A. K. Cheetham, *Journal of Materials Chemistry* **2001**, *11*, 2887–2894.

[17] R. J. Aitken, M. Q. Chaudhry, A. B. A. Boxall, M. Hull, *Occupational Medicine* **2006**, *56*, 300–306.

[18] J. T. Collins, C. Kuppe, D. C. Hooper, C. Sibilia, M. Centini, V. K. Valev, *Advanced Optical Materials* **2017**, *5*, 1700182.

[19] J. Kumar, K. G. Thomas, L. M. Liz-Marzán, *Chemical Communications* **2016**, *52*, 12555–12569.

[20] X. Lan, X. Lu, C. Shen, Y. Ke, W. Ni, Q. Wang, *Journal of the American Chemical Society* **2015**, *137*, 457–462.

[21] T. Bürgi, *Nanoscale* **2015**, *7*, 15553–15567.

[22] G. Shemer, O. Krichevski, G. Markovich, T. Molotsky, I. Lubitz, A. B. Kotlyar, *Journal of the American Chemical Society* **2006**, *128*, 11006–11007.

[23] H. Yao, K. Miki, N. Nishida, A. Sasaki, K. Kimura, *Journal of the American Chemical Society* **2005**, *127*, 15536–15543.

[24] M. Jakob, A. von Weber, A. Kartouzian, U. Heiz, *Physical Chemistry Chemical Physics* **2018**, *20*, 20347–20351.

[25] C. Gautier, T. Bürgi, *Journal of the American Chemical Society* **2006**, *128*, 11079–11087.

[26] H.-E. Lee, H.-Y. Ahn, J. Mun, Y. Y. Lee, M. Kim, N. H. Cho, K. Chang, W. S. Kim, J. Rho, K. T. Nam, *Nature* **2018**, *556*, 360–365.

[27] C. Chang, X. Wang, Y. Bai, H. Liu, *TrAC - Trends in Analytical Chemistry* **2012**, *39*, 195–206.

[28] F. P. Milton, J. Govan, M. V. Mukhina, Y. K. Gun'Ko, *Nanoscale Horizons* **2016**, *1*, 14–26.

[29] M. Heitbaum, F. Glorius, I. Escher, *Angewandte Chemie International Edition* **2006**, *45*, 4732–4762.

[30] A. Edelstein, R. Cammaratra, *Nanomaterials Synthesis, Properties and Applications - 2nd Edition*, CRC Press, Boca Raton, **1996**.

[31] G. Cao, *Nanostructures & Nanomaterials: Synthesis, Properties & Applications*, Imperial College Press, London, **2004**.

[32] C. N. R. Rao, A. Müller, A. K. Cheetham, *Nanomaterials Chemistry: Recent Developments and New Directions*, John Wiley & Sons, Darmstadt, **2007**.

[33] S. M. Bhagyaraj, O. S. Oluwafemi, N. Kalarikkal, S. Thomas, *Synthesis of Inorganic Nanomaterials*, Woodhead Publishing, **2018**, p. 312.

[34] J. Turkevich, P. C. Stevenson, J. Hillier, *Discussions of the Faraday Society* **1951**, *11*, 55.

[35] G. Frens, *Nature Physical Science* **1973**, *241*, 20–22.

[36] B.-K. Pong, H. I. Elim, J.-X. Chong, W. Ji, B. L. Trout, J.-Y. Lee, *The Journal of Physical Chemistry C* **2007**, *111*, 6281–6287.

[37] M. Brust, M. Walker, D. Bethell, D. J. Schiffrin, R. Whyman, *J. Chem. Soc. Chem. Commun.* **1994**, 801–802.

[38] M. N. Martin, J. I. Basham, P. Chando, S.-K. Eah, *Langmuir* **2010**, *26*, 7410–7417.

[39] J. Xie, J. Y. Lee, D. I. C. Wang, *Chemistry of Materials* **2007**, *19*, 2823–2830.

[40] A. Habib, M. Tabata, Y. G. Wu, *Bulletin of the Chemical Society of Japan* **2005**, *78*, 262–269.

[41] D. Yu, V. W.-W. Yam, *Journal of the American Chemical Society* **2004**, *126*, 13200–13201.

[42] I. Freestone, N. Meeks, M. Sax, C. Higgitt, *Gold Bulletin* **2007**, *40*, 270–277.

[43] J. P. Shastri, M. G. Rupani, R. L. Jain, *The Journal of The Textile Institute* **2012**, *103*, 1234–1243.

[44] J. Perelaer, B.-J. de Gans, U. S. Schubert, *Advanced Materials* **2006**, *18*, 2101–2104.

[45] G. J. Hutchings, J. K. Edwards in *Metal Nanoparticles and Nanoalloys*, *Vol. 44*, 2, Elsevier Ltd, **2012**, pp. 249–293.

[46] C. T. Campbell, *Science* **2004**, *306*, 234–235.

[47] D. T. Thompson, *Nano Today* **2007**, *2*, 40–43.

[48] N. T. Kim Thanh, Z. Rosenzweig, *Analytical Chemistry* **2002**, *74*, 1624–1628.

[49] I. H. El-Sayed, X. Huang, M. A. El-Sayed, *Nano Letters* **2005**, *5*, 829–834.

[50] K. Grieve, P. Mulvaney, F. Grieser, *Current Opinion in Colloid and Interface Science* **2000**, *5*, 168–172.

[51] S. M. Liu, S. Sato, K. Kimura, *Langmuir* **2005**, *21*, 6324–6329.

[52] S. M. Liu, Y. Yang, S. Sato, K. Kimura, *Chemistry of Materials* **2006**, *18*, 637–642.

[53] J. G. Veinot, *Chemical Communications* **2006**, 4160–4168.

[54] C. M. Hessel, D. Reid, M. G. Panthani, M. R. Rasch, B. W. Goodfellow, J. Wei, H. Fujii, V. Akhavan, B. A. Korgel, *Chemistry of Materials* **2012**, *24*, 393–401.

[55] M. Dasog, G. B. De los Reyes, L. V. Titova, F. A. Hegmann, J. G. C. Veinot, *ACS Nano* **2014**, *8*, 9636–9648.

[56] A. Angi, R. Sinelnikov, A. Meldrum, J. G. Veinot, I. Balberg, D. Azulay, O. Millo, B. Rieger, *Nanoscale* **2016**, *8*, 7849–7853.

[57] M. Dasog, J. Kehrle, B. Rieger, J. G. C. Veinot, *Angewandte Chemie International Edition* **2016**, *55*, 2322–2339.

[58] S. Sadeghi, B. Ganesh Kumar, R. Melikov, M. Mohammadi Aria, H. Bahmani Jalali, S. Nizamoglu, *Optica* **2018**, *5*, 793.

[59] M. C. Schlamp, X. Peng, A. P. Alivisatos, *Journal of Applied Physics* **1997**, *82*, 5837–5842.

[60] A. Nozik, *Physica E: Low-dimensional Systems and Nanostructures* **2002**, *14*, 115–120.

[61] S. E. Habas, H. A. S. Platt, M. F. A. M. van Hest, D. S. Ginley, *Chemical Reviews* **2010**, *110*, 6571–6594.

[62] C. M. Gonzalez, M. Iqbal, M. Dasog, D. G. Piercey, R. Lockwood, T. M. Klapötke, J. G. Veinot, *Nanoscale* **2014**, *6*, 2608–2612.

[63] L. Cui, X. P. He, G. R. Chen, *RSC Advances* **2015**, *5*, 26644–26653.

[64] Y.-H. Ko, M. Jalalah, S.-J. Lee, J.-G. Park, *Scientific Reports* **2018**, *8*, 12881.

[65] EU Directive 2002/95/EC, *Restriction of the Use of Certain Hazardous Substances in Electrical and Electronic Equipment*, **2003**.

[66] S. De Wolf, A. Descoeudres, Z. C. Holman, C. Ballif, *Green* **2012**, *2*, 7–24.

[67] S. E. Thompson, S. Parthasarathy, *Materials Today* **2006**, *9*, 20–25.

[68] L. Brus, *Journal of physical chemistry* **1994**, *98*, 3575–3581.

[69] J. Aptekar, M. Cassidy, A. Johnson, R. Barton, M. Lee, A. Ogier, C. Vo, M. Anahtar, Y. Ren, S. Bhatia, C. Ramanathan, D. Cory, A. Hill, R. Mair, M. Rosen, R. Walsworth, C. Marcus, *ACS Nano* **2009**, *3*, 4003–4008.

[70] J.-H. Park, L. Gu, G. von Maltzahn, E. Ruoslahti, S. N. Bhatia, M. J. Sailor, *Nature Materials* **2009**, *8*, 331–336.

[71] R. B. M. Schasfoort, *Handbook of Surface Plasmon Resonance - 2nd Edition*, Royal Society of Chemistry, Croydon, **2017**.

[72] M. A. Garcia, *Journal of Physics D: Applied Physics* **2011**, *44*, 283001.

[73] R. v. Baltz in *Spectroscopy and Dynamics of Collective Excitations in Solids*, **1997**, pp. 303–338.

[74] B. Wu, N. Mathews, T.-C. Sum in *Plasmonic Organic Solar Cells, Nanoscience and Nanotechnology*, **2017**, pp. 25–31.

[75] H. N. Daghestani, B. W. Day, *Sensors* **2010**, *10*, 9630–9646.

[76] G. Mie, *Annale der Physik* **1908**, *25*, 377–452.

[77] C. L. Nehl, J. H. Hafner, *Journal of Materials Chemistry* **2008**, *18*, 2415–2419.

[78] S. Link, M. A. El-Sayed, *The Journal of Physical Chemistry B* **2002**, *103*, 4212–4217.

[79] H. Hovel, S. Fritz, A. Hilger, V. Kreibig, *Physical Review B* **1993**, *48*.

[80] T. Lünskens, P. Heister, M. Thämer, C. a. Walenta, A. Kartouzian, U. Heiz, *Phys. Chem. Chem. Phys.* **2015**, *17*, 17541–17544.

[81] M. Thämer, A. Kartouzian, P. Heister, T. Lünskens, S. Gerlach, U. Heiz, *Small* **2014**, *10*, 2340–2344.

[82] J. I. Pankove, *Optical Processes in Semiconductors*, Dover Publications, Inc., New York, **1971**.

[83] Y. Varshni, *Physica* **1967**, *34*, 149–154.

[84] K. P. O'Donnell, X. Chen, *Applied Physics Letters* **1991**, *58*, 2924–2926.

[85] N. N. Kiselyova, V. A. Dudarev, M. A. Korzhuyev, *Inorganic Materials: Applied Research* **2016**, *7*, 34–39.

[86] L. Bergman, J. McHale, *Handbook of Luminescent Semiconductor Materials*, CRC Press, New York, **2016**.

[87] J. Singh, K. Shimakawa, *Advances in Amorphous Semiconductors*, CRC Press, New York, **2003**.

[88] A. G. Cullis, L. T. Canham, P. D. J. Calcott, *Journal of Applied Physics* **1997**, *82*, 909–965.

[89] C. Meier, A. Gondorf, S. Lüttjohann, A. Lorke, H. Wiggers, *Journal of Applied Physics* **2007**, *101*, 103112.

[90] D. Kovalev, H. Heckler, M. Ben-Chorin, G. Polisski, M. Schwartzkopff, F. Koch, *Physical Review Letters* **1998**, *81*, 2803–2806.

[91] L. Pavesi, R. Turan, *Silicon Nanocrystals: Fundamentals, Synthesis and Applications*, Wiley-VCH Verlag GmbH & Co. KGaA, Weinheim, Germany, **2010**.

[92] M. S. Hybersten, *Physical Review Letters* **1994**, *72*, 8.

[93] D. S. English, L. E. Pell, Z. Yu, P. F. Barbara, B. A. Korgel, D. S. English, B. A. Korgel, Z. Yu, *Nano Letters* **2002**, *2*, 681–685.

[94] J. Heitmann, F. Müller, M. Zacharias, U. Gösele, *Advanced Materials* **2005**, *17*, 795–803.

[95] M. Jakob, A. Aissiou, W. Morrish, F. Marsiglio, M. Islam, A. Kartouzian, A. Meldrum, *Nanoscale Research Letters* **2018**, *13*, 383.

[96] M. Dasog, Z. Yang, S. Regli, T. M. Atkins, A. Faramus, M. P. Singh, E. Muthuswamy, S. M. Kauzlarich, R. D. Tilley, J. G. C. Veinot, *ACS Nano* **2013**, *7*, 2676–2685.

[97] R. Sinelnikov, M. Dasog, J. Beamish, A. Meldrum, J. G. Veinot, *ACS Photonics* **2017**, *4*, 1920–1929.

[98] T. Mitsuoka, T. Morikawa, Y. Sugiyama, K. Nakanishi, T. Ohta, H. Nakano, H. Okamoto, *Journal of the American Chemical Society* **2010**, *132*, 5946–5947.

[99] T. Helbich, A. Lyuleeva, T. Ludwig, L. M. Scherf, T. F. Fässler, P. Lugli, B. Rieger, *Advanced Functional Materials* **2016**, *26*, 6711–6718.

[100] M. L. Mastronardi, E. J. Henderson, D. P. Puzzo, G. A. Ozin, *Advanced Materials* **2012**, *24*, 5890–5898.

[101] L. F. Fraceto, R. de Lima, H. C. Oliveira, D. S. Ávila, B. Chen, *Energy Ecology and Environment* **2018**, *3*, 69–71.

[102] L. D. Barron, *Space Science Reviews* **2008**, *135*, 187–201.

[103] F. Rolf, *Journal of Chemical Information and Modeling* **2013**, *53*, 1689–1699.

[104] M. Quack in, *Vol. 26*, **2012**, pp. 47–76.

[105] M. Nic, L. Hovorka, J. Jirat, B. Kosata, J. Znamenacek, *Compendium of Chemical Terminology 2nd ed. (the Gold Book)*, IUPAC, **2014**, p. 1670.

[106] S. S. Oh, O. Hess, *Nano Convergence* **2015**, *2*, 24.

[107] V. K. Valev, J. J. Baumberg, C. Sibilia, T. Verbiest, *Advanced Materials* **2013**, *25*, 2517–2534.

[108] S. Knoppe, T. Bürgi, *CHIMIA International Journal for Chemistry* **2013**, *67*, 236–239.

[109] Z. Fan, A. O. Govorov, *Nano Letters* **2010**, *10*, 2580–2587.

[110] C. Gautier, T. Bürgi, *ChemPhysChem* **2009**, *10*, 483–492.

[111] T. G. Schaaff, R. L. Whetten, *The Journal of Physical Chemistry B* **2000**, *104*, 2630–2641.

[112] I. Schrader, S. Neumann, A. Šulce, F. Schmidt, V. Azov, S. Kunz, *ACS Catalysis* **2017**, *7*, 3979–3987.

[113] J. M. Hawkins, T. J. N. Watson, *Angewandte Chemie International Edition* **2004**, *43*, 3224–3228.

[114] W. Ma, L. Xu, A. F. de Moura, X. Wu, H. Kuang, C. Xu, N. A. Kotov, *Chemical Reviews* **2017**, *117*, 8041–8093.

[115] J. Labuta, J. P. Hill, S. Ishihara, L. Hanyková, K. Ariga, *Accounts of Chemical Research* **2015**, *48*, 521–529.

[116] W. L. Barnes, A. Dereux, T. W. Ebbesen, *Nature* **2003**, *424*, 824–830.

[117] J. Flammer, M. Mozaffarieh, H. Bebie, *Basic Sciences in Ophthalmology*, Springer Berlin Heidelberg, **2013**, pp. 21–39.

[118] T. Renner, E. R. Cohen, T. Cvitas, J. G. Frey, B. Holström, K. Kuchitsu, R. Marquardt, I. Mills, F. Pavese, M. Quack, J. Stohner, H. L. Strauss, M. Takami, A. J. Thor, *Quantities, Units and Symbols in Physical Chemistry*, The Royal Society of Chemistry, **2007**, P001–232.

[119] S. Zhang, L. Li, A. Kumar, *Materials Characterization Techniques - 1st Edition*, CRC Press, London, **2009**.

[120] G. Hohberg, A. Matthes, H. Schlemmer, U.S. Patent 5,164,586: Arrangement for measuring the absorption of transparent specimens mounted within an integrating sphere, **1992**.

[121] P. Elterman, *Applied Optics* **1970**, *9*, 2140.

[122] D. G. Goebel, *Applied Optics* **1967**, *6*, 125.

[123] L. Porrès, A. Holland, L.-O. Pålsson, A. P. Monkman, C. Kemp, A. Beeby, *Journal of Fluorescence* **2006**, *16*, 267–273.

[124] M. L. Rastello, E. Miraldi, P. Pisoni, *Applied Optics* **2008**, *35*, 4385.

[125] N. Berova, K. Nakanishi, R. W. Woody, *Circular Dichroism - 2nd Edition*, Wiley-VCH Verlag GmbH & Co. KGaA, New York, **2000**.

[126] S. Mitchell, *Nature* **1950**, *166*, 434–435.

[127] J. R. Lakowicz, *Principles of Fluorescence Spectroscopy - 3rd Edition*, Springer US, Boston, **2006**, p. 362.

[128] A. Edgar in *Springer Handbook of Electronic and Photonic Materials*, Springer International Publishing, Cham, **2017**, pp. 1–1.

[129] E. F. Gudgin-Templeton, W. R. Ware, *The Journal of Physical Chemistry* **1984**, *88*, 4626–4631.

[130] M. Jakob, M. Javadi, J. G. C. Veinot, A. Meldrum, A. Kartouzian, U. Heiz, *Chemistry - A European Journal* **2019**, *25*, 3061–3067.

[131] N. Chestnoy, T. D. Harris, R. Hull, L. E. Brus, *The Journal of Physical Chemistry* **1986**, *90*, 3393–3399.

[132] T. Orii, M. Hirasawa, T. Seto, N. Aya, S. Onari, *European Physical Journal D* **2003**, *24*, 119–122.

[133] P. A. Franken, A. E. Hill, C. W. Peters, G. Weinreich, *Physical Review Letters* **1961**, *7*, 118–119.

[134] R. W. Boyd, *Nonlinear Optics - 3rd Edition*, Elsevier, **2003**.

[135] M. Thämer, A. Kartouzian, P. Heister, S. Gerlach, M. Tschurl, U. Boesl, U. Heiz, *The Journal of Physical Chemistry C* **2012**, *116*, 8642–8648.

[136] T. Lünskens, P. Heister, M. Thämer, C. A. Walenta, A. Kartouzian, U. Heiz, *Physical Chemistry Chemical Physics* **2015**, *17*, 17541–17544.

[137] M. N. Teerenstra, J. G. Hagting, A. J. Schouten, R. J. M. Nolte, M. Kauranen, T. Verbiest, A. Persoons, *Macromolecules* **1996**, *29*, 4876–4879.

[138] A. von Weber, M. Jakob, E. Kratzer, A. Kartouzian, U. Heiz, *ChemPhysChem* **2019**, *20*, 134–141.

[139] A. Kartouzian, P. Heister, M. Thämer, S. Gerlach, U. Heiz, *Journal of the Optical Society of America B* **2013**, *30*, 541.

[140] T. F. Heinz, C. K. Chen, *Physical Review Letters* **1982**, *48*, 478–481.

[141] T. Petralli-Mallow, T. M. Wong, J. D. Byers, H. I. Yee, J. M. Hicks, *Journal of Physical Chemistry* **1993**, *97*, 1383–1388.

[142] J. J.M.Hicks, *Physical Review B* **1994**, *49*, 643–648.

[143] S. Sioncke, T. Verbiest, A. Persoons, *Materials Science and Engineering R* **2003**, *42*, 115–155.

[144] J. M. Hicks, T. Petralli-Mallow, H. I. Yee, J. D. Byers, T. M. Wong, *The Journal of Physical Chemistry* **2005**, *97*, 1383–1388.

[145] S. Knoppe, H. Häkkinen, T. Verbiest, *Journal of Physical Chemistry C* **2015**, *119*, 27676–27682.

[146] J. C. Rivière, S. Myhra, *Handbook of Surface and Interface Analysis: Methods for Problem-Solving - 2nd Edition*, CRC Press, Boca Raton, **1998**.

[147] V. Pecharsky, P. Zavalij, *Fundamentals of Powder Diffraction and Structural Characterization of Materials*, Springer US, Boston, MA, **2009**.

[148] B. Warren, *X-Ray Diffraction*, Dover Publications, New York, **1990**.

[149] P. Scherrer in *Kolloidchemie Ein Lehrbuch*, Springer Berlin Heidelberg, **1920**, pp. 387–409.

[150] I. Watt, *The Principles and Practice of Electron Microscopy - 2nd Edition*, Cambridge University Press, Cambridge, **1997**.

[151] L. Reimer, H. Kohl in *Springer Series in Optical Sciences*, Springer US, New York, **2008**.

[152] S. Ristig, PhD thesis, Universität Duisburg-Essen, **2014**.

[153] R. A. Groneberg, J. R. Regan, K. W. Neuenschwander, A. C. Scotese, U.S. Patent 5,455,260: Aliphatic amino bis-aryl squalene synthase inhibitors, **1995**.

[154] S. Link, M. A. El-Sayed, *The Journal of Physical Chemistry B* **1999**, *103*, 4212–4217.

[155] M.-R. Goldsmith, C. B. George, G. Zuber, R. Naaman, D. H. Waldeck, P. Wipf, D. N. Beratan, *Phys. Chem. Chem. Phys.* **2006**, *8*, 63–67.

[156] Z. Wang, B. H. Teh, Y. Wang, G. Adamo, J. Teng, H. Sun, *Applied Physics Letters* **2017**, *110*, 221108.

[157] M. D'Acunto, F. Fuso, R. Micheletto, M. Naruse, F. Tantussi, M. Allegrini, *Beilstein Journal of Nanotechnology* **2017**, *8*, 956–967.

[158] O. Loebich, *Gold Bulletin* **1972**, *5*, 2–10.

[159] A. H. Pakiari, Z. Jamshidi, *The Journal of Physical Chemistry A* **2010**, *114*, 9212–9221.

[160] F. Kim, J. H. Song, P. Yang, *Journal of the American Chemical Society* **2002**, *124*, 14316–14317.

[161] S. Knoppe, T. Burgi, *Accounts of Chemical Research* **2014**, *47*, 1318–1326.

[162] S. A. Scherbak, A. A. Lipovskii, *Journal of Physics: Conference Series* **2016**, *741*, 012120.

[163] L. E. Shea-Rohwer, J. E. Martin, *Journal of Luminescence* **2007**, *127*, 499–507.

[164] J. E. Martin, L. E. Shea-Rohwer, *Journal of Luminescence* **2006**, *121*, 573–587.

[165] K. Furuta, M. Fujii, H. Sugimoto, K. Imakita, *The Journal of Physical Chemistry Letters* **2015**, *6*, 2761–2766.

[166] R. Bose, J. F. McMillan, J. Gao, K. M. Rickey, C. J. Chen, D. V. Talapin, C. B. Murray, C. W. Wong, *Nano letters* **2008**, *8*, 2006–2011.

[167] D. Pfister, K. Schäfer, C. Ott, B. Gerke, R. Pöttgen, O. Janka, M. Baumgartner, A. Efimova, A. Hohmann, P. Schmidt, S. Venkatachalam, L. van Wüllen, U. Schürmann, L. Kienle, V. Duppel, E. Parzinger, B. Miller, J. Becker, A. Holleitner, R. Weihrich, T. Nilges, *Advanced Materials* **2016**, *28*, 9783–9791.

[168] P. Manoj, P. Koshy, V. Vaidyan, *Progress in Natural Science: Materials International* **2012**, *22*, 79–85.

[169] E. Castiglioni, P. Albertini, *Chirality* **2000**, *12*, 291–294.

[170] T. Harada, Y. Miyoshi, R. Kuroda, *Review of Scientific Instruments* **2009**, *80*, 046101.

[171] G. Ledoux, O. Guillois, D. Porterat, C. Reynaud, F. Huisken, B. Kohn, V. Paillard, *Physical Review B* **2000**, *62*, 15942–15951.

[172] B. Delley, E. F. Steigmeier, *Applied Physics Letters* **1995**, *67*, 2370.

[173] A. M. Hartel, S. Gutsch, D. Hiller, M. Zacharias, *Physical Review B* **2012**, *85*, 165306.

[174] A. R. Van Sickle, J. B. Miller, C. Moore, R. J. Anthony, U. R. Kortshagen, E. K. Hobbie, *ACS Applied Materials & Interfaces* **2013**, *5*, 4233–4238.

[175] N. L. Rosi, C. A. Mirkin, *Chemical Reviews* **2005**, *105*, 1547–1562.

[176] M. Schäferling, M. Hentschel, D. Dregely, X. Yin, H. Giessen, *AIP Conference Proceedings* **2012**, *1475*, 77–79.

[177] M. Roy, P. Mukherjee, B. P. Mandal, R. K. Sharma, A. K. Tyagi, S. P. Kale, *RSC Advances* **2012**, *2*, 6496.

[178] Q. Wu, H. Cao, Q. Luan, J. Zhang, Z. Wang, J. H. Warner, A. A. Watt, *Inorg Chem* **2008**, *47*, 5882–5888.

[179] N. V. Tepliakov, A. S. Baimuratov, I. A. Vovk, M. Y. Leonov, A. V. Baranov, A. V. Fedorov, I. D. Rukhlenko, *ACS Nano* **2017**, *11*, 7508–7515.

[180] J. Ahn, E. Lee, J. Tan, W. Yang, B. Kim, J. Moon, *Materials Horizons* **2017**, *4*, 851–856.

[181] A. S. Baimuratov, T. P. Pereziabova, M. Y. Leonov, W. Zhu, A. V. Baranov, A. V. Fedorov, Y. K. Gun'ko, I. D. Rukhlenko, *ACS Nano* **2018**, *12*, 6203–6209.

[182] M. P. Moloney, Y. K. Gun'ko, J. M. Kelly, *Chemical Communications* **2007**, *7345*, 3900.

[183] V. Dobrokhotov, L. Oakes, D. Sowell, A. Larin, J. Hall, A. Barzilov, A. Kengne, P. Bakharev, G. Corti, T. Cantrell, T. Prakash, J. Williams, L. Bergman, J. Huso, D. McIlroy, *Sensors* **2012**, *12*, 5608–5622.

[184] G. Corti, Y. Zhan, L. Wang, B. Hare, T. Cantrell, M. B. II, T. Prakash, F. M. Ytreberg, M. A. Miller, D. N. McIlroy, *Journal of Physics D: Applied Physics* **2013**, *46*, 505307.

[185] T. Khudiyev, M. Bayindir, *Applied Optics* **2015**, *54*, 8018.

Appendix - Reprint Permissions

Chirality transfer from organic ligands to silver nanostructures via chiral polarisation of the electric field

Chirality transfer from organic ligands to silver nanostructures *via* chiral polarisation of the electric field

M. Jakob, A. von Weber, A. Kartouzian and U. Heiz, *Phys. Chem. Chem. Phys.*, 2018, **20**, 20347
DOI: 10.1039/C8CP02970A

- For reproduction of material from all other RSC journals:
  [Original citation] - Reproduced by permission of The Royal Society of Chemistry

If you are the author of this article you still need to obtain permission to reproduce the whole article in a third party publication with the exception of reproduction of the whole article in a thesis or dissertation.

Information about reproducing material from RSC articles with different licences is available on our Permission Requests page.

Reappraising the Luminescence Lifetime Distributions in Silicon Nanocrystals

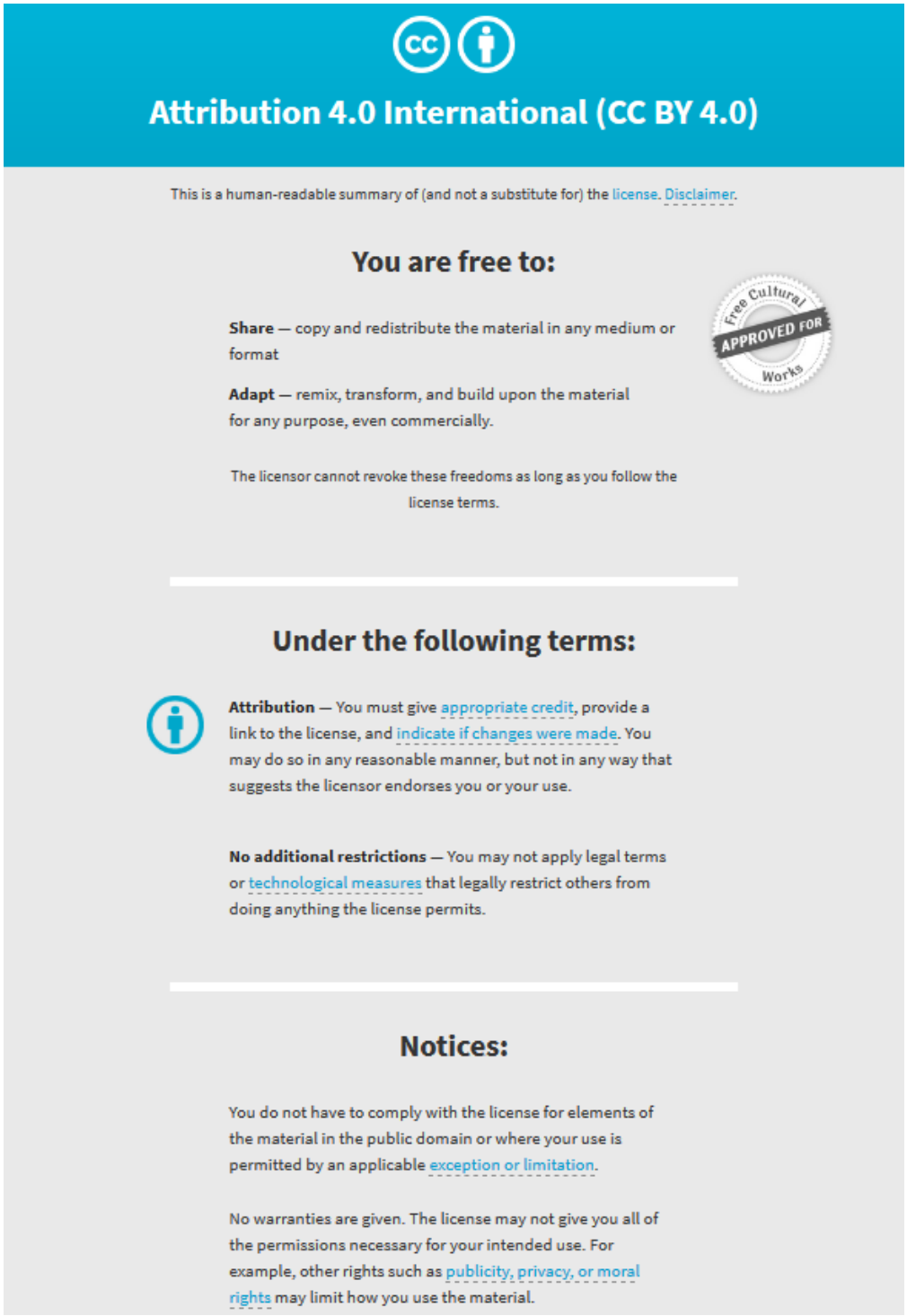

Attribution 4.0 International (CC BY 4.0)

This is a human-readable summary of (and not a substitute for) the license. Disclaimer.

You are free to:

Share — copy and redistribute the material in any medium or format

Adapt — remix, transform, and build upon the material for any purpose, even commercially.

The licensor cannot revoke these freedoms as long as you follow the license terms.

Under the following terms:

Attribution — You must give appropriate credit, provide a link to the license, and indicate if changes were made. You may do so in any reasonable manner, but not in any way that suggests the licensor endorses you or your use.

No additional restrictions — You may not apply legal terms or technological measures that legally restrict others from doing anything the license permits.

Notices:

You do not have to comply with the license for elements of the material in the public domain or where your use is permitted by an applicable exception or limitation.

No warranties are given. The license may not give you all of the permissions necessary for your intended use. For example, other rights such as publicity, privacy, or moral rights may limit how you use the material.

Ensemble effects in the temperature-dependent photoluminescence of silicon nanocrystals

JOHN WILEY AND SONS LICENSE TERMS AND CONDITIONS

Feb 05, 2019

This Agreement between Mr. Matthias Jakob ("You") and John Wiley and Sons ("John Wiley and Sons") consists of your license details and the terms and conditions provided by John Wiley and Sons and Copyright Clearance Center.

License Number	4522500344255
License date	Feb 05, 2019
Licensed Content Publisher	John Wiley and Sons
Licensed Content Publication	Chemistry - A European Journal
Licensed Content Title	Ensemble Effects in the Temperature-Dependent Photoluminescence of Silicon Nanocrystals
Licensed Content Author	Matthias Jakob, Morteza Javadi, Jonathan G. C. Veinot, et al
Licensed Content Date	Jan 31, 2019
Licensed Content Volume	0
Licensed Content Issue	0
Licensed Content Pages	8
Type of use	Dissertation/Thesis
Requestor type	Author of this Wiley article
Format	Print and electronic
Portion	Full article
Will you be translating?	No
Title of your thesis / dissertation	Optical and Chiroptical Properties of Semiconductor and Noble Metal Nanomaterials
Expected completion date	Jun 2019
Expected size (number of pages)	150
Requestor Location	Mr. Matthias Jakob Destouchesstrasse 71 Munich, 80796 Germany Attn: Mr. Matthias Jakob
Publisher Tax ID	EU826007151
Total	0.00 EUR
Terms and Conditions	

TERMS AND CONDITIONS

This copyrighted material is owned by or exclusively licensed to John Wiley & Sons, Inc. or one of its group companies (each a"Wiley Company") or handled on behalf of a society with which a Wiley Company has exclusive publishing rights in relation to a particular work (collectively "WILEY"). By clicking "accept" in connection with completing this licensing transaction, you agree that the following terms and conditions apply to this transaction (along with the billing and payment terms and conditions established by the Copyright Clearance Center Inc., ("CCC's Billing and Payment terms and conditions"), at the time that you opened your RightsLink account (these are available at any time at

In situ second-harmonic generation circular dichroism with submonolayer sensitivity

JOHN WILEY AND SONS LICENSE TERMS AND CONDITIONS

Dec 10, 2018

This Agreement between Mr. Matthias Jakob ("You") and John Wiley and Sons ("John Wiley and Sons") consists of your license details and the terms and conditions provided by John Wiley and Sons and Copyright Clearance Center.

License Number	4485340684434
License date	Dec 10, 2018
Licensed Content Publisher	John Wiley and Sons
Licensed Content Publication	ChemPhysChem
Licensed Content Title	In situ Second-Harmonic Generation Circular Dichroism with Submonolayer Sensitivity
Licensed Content Author	Alexander von Weber, Matthias Jakob, Eva Kratzer, et al
Licensed Content Date	Nov 30, 2018
Licensed Content Volume	0
Licensed Content Issue	0
Licensed Content Pages	9
Type of use	Dissertation/Thesis
Requestor type	Author of this Wiley article
Format	Print and electronic
Portion	Full article
Will you be translating?	No
Title of your thesis / dissertation	Optical and Chiroptical Properties of Semiconductor and Noble Metal Nanomaterials
Expected completion date	Jun 2019
Expected size (number of pages)	150
Requestor Location	Mr. Matthias Jakob Destouchesstrasse 71 Munich, 80796 Germany Attn: Mr. Matthias Jakob
Publisher Tax ID	EU826007151
Total	0.00 EUR
Terms and Conditions	

TERMS AND CONDITIONS

This copyrighted material is owned by or exclusively licensed to John Wiley & Sons, Inc. or one of its group companies (each a"Wiley Company") or handled on behalf of a society with which a Wiley Company has exclusive publishing rights in relation to a particular work (collectively "WILEY"). By clicking "accept" in connection with completing this licensing transaction, you agree that the following terms and conditions apply to this transaction (along with the billing and payment terms and conditions established by the Copyright Clearance Center Inc., ("CCC's Billing and Payment terms and conditions"), at the time that you opened your RightsLink account (these are available at any time at

Inorganic Double Helices in Semiconducting SnIP

Order Completed

Thank you for your order.

This Agreement between Mr. Matthias Jakob ("You") and John Wiley and Sons ("John Wiley and Sons") consists of your license details and the terms and conditions provided by John Wiley and Sons and Copyright Clearance Center.

Your confirmation email will contain your order number for future reference.

printable details

License Number	4534170052655
License date	Feb 22, 2019
Licensed Content Publisher	John Wiley and Sons
Licensed Content Publication	Advanced Materials
Licensed Content Title	Inorganic Double Helices in Semiconducting SnIP
Licensed Content Author	Daniela Pfister, Konrad Schäfer, Claudia Ott, et al
Licensed Content Date	Sep 14, 2016
Licensed Content Volume	28
Licensed Content Issue	44
Licensed Content Pages	9
Type of use	Dissertation/Thesis
Requestor type	University/Academic
Format	Print and electronic
Portion	Figure/table
Number of figures/tables	1
Original Wiley figure/table number(s)	Figure 1
Will you be translating?	No
Title of your thesis / dissertation	Optical and Chiroptical Properties of Semiconductor and Noble Metal Nanomaterials
Expected completion date	Jun 2019
Expected size (number of pages)	150
Requestor Location	Mr. Matthias Jakob Destouchesstrasse 71 Munich, 80796 Germany Attn: Mr. Matthias Jakob
Publisher Tax ID	EU826007151
Total	0.00 EUR